

POLITECNICO DI TORINO

**Corso di Laurea Magistrale
in INGEGNERIA MECCATRONICA**

Tesi di Laurea Magistrale

**Calibration of the SAIFE technological demonstrator's 3-axis
gyroscope and 3-axis accelerometer**



Supervised by

Prof. Angelo Lerro

Dr. Macro Pisani

Prof. Piero Gili

Prof. Marcello Chiaberge

Author by

Xiaochen Meng

Anno Accademico 2020-2021

Abstract

SAIFE (Synthetic Air Data and Inertial Reference System) is a miniaturized solution, suitable for modern aircraft, and can also be applied to UAVs and urban mobile aircraft. The content of this article is part of the SAIFE project. The project aims to demonstrate model-free technology up to TRL 6, using the most advanced sensors to directly measure inertial and air data. The work of the thesis was carried out in the laboratory of the Italian National Metrology Institute, and the fiber optic gyroscope and accelerometer were first calibrated. In the calibration of the gyroscope, the roundness detector, high-precision stepper motor, an Arduino development board are used to complete the construction of the test platform, and the Arduino development board and IDE tools are used to write the test program. This program will control the rotation speed of the stepper motor and direction. The rotating platform of the roundness detector is driven by a stepping motor, and the fiber optic gyroscope is fixed on the platform for testing. Test the three axes of the fiber optic gyroscope at a rate from 0°/s to 100°/s. The fiber optic gyroscope is connected to the PC, and the test data is collected using the developer software provided by KVH. In terms of accelerometer testing, the dynamic acceleration and vibration laboratory of INRiM provides support. The accelerometer's working state will be 0Hz to 100Hz, and the acceleration value will be between 0g-10g. Use Laser Vibrometer to test the performance of the accelerometer in low-frequency motion, and use Vibration Shaker to test the performance of the accelerometer in high-frequency motion. Use Sensor's developer software to collect accelerometer data. The second step is to integrate the two sensors into the demonstrator of the SAIFE project, and perform speed rate test and acceleration test on the demonstrator. The demonstrator will automatically record the sensor data. All the above test data are processed using Excel tools, and the linear regression method is used for analysis in Excel. By comparing and analyzing the datasheets of the sensors, summarize and calibrate their actual performance.

Keywords: fiber optic gyroscope, accelerometer, calibration, demonstrator

Acknowledgments

First of all, the big Thank you to my supervisor prof. Angelo Lerro. Throughout the whole process of working on this thesis, he was informative and helpful. He gave me an internship opportunity for working in INRiM. I am deeply grateful for his help in the platoon of this thesis.

A warm Thank you to my co-supervisor, mentor and navigator, Dr. Marco Pisani from INRiM (Istituto Nazionale di Ricerca Metrologica). His door was always open to me and he had a positive and friendly attitude. He let me be independent, yet gently guided me at the same time. Thank you for all your time and support.

Special gratitude to the organization of The SERVIZIO PREVENZIONE E PROTEZIONE from Politecnico di Torino for providing me with the Safety training. I would especially like to thank Dr. Milena Astrua for her immense hospitality and constant availability while I was a guest in her office. And last, I would like to thank my family, my mother, father for their everlasting encouragement and cheer in all goings-on in my life.

Content

| | | |
|-------|--|----|
| 1 | General introduction | 1 |
| 1.1 | Avionics..... | 1 |
| 1.2 | MEMS tech..... | 1 |
| 1.3 | Backgrounds and goals..... | 2 |
| 1.4 | Literature review | 3 |
| 2 | Test facility | 4 |
| 2.1 | Test platform: FEDERAL MODEL FORMSCAN 3000 Roundness checker | 4 |
| 2.2 | Micro Stepper Motor | 6 |
| 2.3 | MCU (Arduino)..... | 7 |
| 2.3.1 | Arduino Uno R3 development board..... | 8 |
| 2.3.2 | Arduino language..... | 10 |
| 2.3.3 | Arduino development environment setup..... | 11 |
| 2.4 | Accelerometer calibration facility | 12 |
| 2.4.1 | Laser Vibrometer | 12 |
| 2.4.2 | Vibration Shaker | 16 |
| 3 | Devices under test..... | 18 |
| 3.1 | KVH Gyroscope 1760-3axis | 18 |
| 3.1.1 | Working principle | 19 |
| 3.1.2 | features..... | 21 |
| 3.1.3 | Development software | 22 |
| 3.2 | STIM318 IMU..... | 23 |
| 3.2.1 | Work principle | 23 |
| 3.2.2 | Features of STIM318 | 27 |
| 3.2.3 | Development software | 30 |
| 3.3 | Prototype: The SAIFE Demonstrator | 32 |
| 4 | Measurement campaign | 33 |
| 4.1 | Validation workflow..... | 33 |
| 4.1.1 | Signal generation..... | 34 |
| 4.1.2 | Input signal frequency calibration..... | 39 |
| 4.1.3 | Connect the stepper motor | 39 |

| | | |
|-------|--|----|
| 4.1.4 | Platform horizon adjustment | 44 |
| 4.2 | Methodology in the data processing | 45 |
| 4.3 | Data analysis with Excel | 48 |
| 5 | Results | 48 |
| 5.1 | Analysis data | 48 |
| 5.1.1 | Fiber optic gyroscope | 48 |
| 5.1.2 | IMU | 60 |
| 5.1.3 | SAIFE Demonstrator | 80 |
| 6 | Conclusions | 92 |
| | Reference | 94 |

Figures

| | |
|---|----|
| Figure 2.3.1-1 the whole equipment of the roundness checker | 5 |
| Figure 2.3.1-2 rotation platform..... | 5 |
| Figure 2.3.1-1 Arduino UNO R3 | 8 |
| Figure 2.3.1-1 Arduino UNO PIN labels | 9 |
| Figure 2.3.3-1 Arduino UNO connecting cables | 11 |
| Figure 2.4.1-1 Description drawing | 13 |
| Figure 2.4.1-2 laser vibrometer controller | 13 |
| Figure 2.4.1-3 laser probe | 15 |
| Figure 2.4.1-4 controllers on platform | 15 |
| Figure 2.4.2-1 Speaker and shaker..... | 16 |
| Figure 2.4.2-2 Left-hand rules | 16 |
| Figure 2.4.2-3 Engineering drawing of shaker | 17 |
| Figure 3.1.1-1 Schematic diagram of FOG..... | 19 |
| Figure 3.1.2-1 FOG engineering drawing..... | 21 |
| Figure 3.1.3-1 Development software layout..... | 22 |
| Figure 3.2.1-1 Dynamic coordinate system of particle motion in Coriolis effect | 24 |
| Figure 3.2.1-2 Simplified diagram of internal structure model of MEMS inertial gyroscope | 24 |
| Figure 3.2.1-3 Schematic diagram of MEMS accelerometer principle | 26 |
| Figure 3.2.2-1 Frequency characteristics of gyros with low-pass filter -3dB frequency set to 262Hz..... | 28 |
| Figure 3.2.2-2 Frequency characteristics of gyros with low-pass filter -3dB frequency set to 262Hz..... | 28 |
| Figure 3.2.2-3 Frequency characteristics of accelerometers with low-pass filter -3dB frequency set to 262Hz | 29 |
| Figure 3.2.2-4 Frequency characteristics of accelerometers with low-pass filter -3dB frequency set to 262Hz | 29 |
| Figure 3.2.3-1 connection of the testing system | 31 |
| Figure 3.2.3-2 Development software dashboard | 32 |
| Figure 3.2.3-3 saving data format | 32 |
| Figure 3.2.3-1 The SAIFE Demonstrator..... | 33 |
| Figure 4.1.1-1 Signal workflow diagram..... | 34 |

| | |
|---|----|
| Figure 4.1.1-2 Ideal signal behavior | 34 |
| Figure 4.1.1-3 Signal with 100Hz constant | 35 |
| Figure 4.1.1-4 Ideal trapezoidal signal. | 36 |
| Figure 4.1.1-5 stepper increase signal | 37 |
| Figure 4.1.3-1 Driver board..... | 40 |
| Figure 4.1.3-2 layouts of stepper motor | 41 |
| Figure 4.1.3-3 motor connection pin | 41 |
| Figure 4.1.3-4 motor unlock | 42 |
| Figure 4.1.3-5 step angle switch..... | 43 |
| Figure 4.1.3-6 cables connection and operation current graph..... | 44 |
| Figure 4.1.3-7 Physical display | 44 |
| Figure 4.1.4-1 roundness platform horizon calibration | 45 |
| Figure 5.1.1-1 FOG test on Z-axis | 49 |
| Figure 5.1.1-2 Z-axis test run | 49 |
| Figure 5.1.1-3 Half period of rotation | 50 |
| Figure 5.1.1-4 GYRO Z-axis period collection..... | 51 |
| Figure 5.1.1-5 GYRO Z-axis with 0Hz | 51 |
| Figure 5.1.1-6 GYRO Z-axis with 10Hz | 52 |
| Figure 5.1.1-7 GYRO Z-axis with 100Hz | 52 |
| Figure 5.1.1-8 GYRO Z-axis with 200Hz | 52 |
| Figure 5.1.1-9 GYRO Z-axis with 300Hz | 53 |
| Figure 5.1.1-10 FOG gyro data on Z-axis | 54 |
| Figure 5.1.1-11 FOG test on X-axis & Y-axis | 54 |
| Figure 5.1.1-12 GYRO Xaxis output | 55 |
| Figure 5.1.1-13 GYRO Yaxis output | 56 |
| Figure 5.1.1-14 Earth rotation on Y-axis..... | 57 |
| Figure 5.1.1-15 Moving average calculated on Y-axis | 58 |
| Figure 5.1.1-16 earth rotation on Y-axis | 58 |
| Figure 5.1.1-17 earth rotation on z-axis | 59 |
| Figure 5.1.1-18 earth rotation on X-axis | 60 |
| Figure 5.1.2-1 STIM318 on platform | 61 |

| | |
|--|----|
| Figure 5.1.2-2 IMU gyro X-axis with 0Hz | 61 |
| Figure 5.1.2-3 IMU GYRO X-axis with 10Hz | 61 |
| Figure 5.1.2-4 GYRO X-axis with 100Hz | 62 |
| Figure 5.1.2-5 GYRO X-axis with 200Hz | 62 |
| Figure 5.1.2-6 GYRO X-axis with 300Hz | 63 |
| Figure 5.1.2-7 IMU_GYRO X-axis output..... | 64 |
| Figure 5.1.2-8 Residual of IMU GYRO X-axis..... | 65 |
| Figure 5.1.2-9 IMU_GYRO_Yaxis | 66 |
| Figure 5.1.2-10 IMU GYRO z-axis | 67 |
| Figure 5.1.2-11 sensor on the Horizon platform..... | 68 |
| Figure 5.1.2-12 sensor on the vertical testing platform | 68 |
| Figure 5.1.2-13 Acc output with 1Hz | 69 |
| Figure 5.1.2-14 fitting line of acc X-axis 1Hz | 70 |
| Figure 5.1.2-15 IMU Acc Y-axis 1Hz fitting line..... | 70 |
| Figure 5.1.2-16 IMU Acc Z-axis 1Hz fitting line..... | 71 |
| Figure 5.1.2-17 IMU ACC X-axis 80Hz_9.42g..... | 71 |
| Figure 5.1.2-18 IMU_80Hz_X-axis behavior..... | 72 |
| Figure 5.1.2-19 IMU_80Hz_Yaxis behavior | 74 |
| Figure 5.1.2-20 IMU_80Hz_Z-axis behavior | 75 |
| Figure 5.1.2-21 X-axis different frequency | 76 |
| Figure 5.1.2-22 Acc Y-axis different frequency | 77 |
| Figure 5.1.2-23 ACC z-axis different frequency | 78 |
| Figure 5.1.2-24 IMU_Acc_Zaxis frequency range behavior | 79 |
| Figure 5.1.2-25 low pass filter at 262Hz frequency behavior..... | 80 |
| Figure 5.1.3-1 View of FOG..... | 81 |
| Figure 5.1.3-2 Axis component in demonstrator | 81 |
| Figure 5.1.3-3 GYRO X-axis ideal angle | 82 |
| Figure 5.1.3-4 gyro Y-axis ideal angle 45° | 83 |
| Figure 5.1.3-5 GYRO X-axis real angle | 84 |
| Figure 5.1.3-6 GYRO Y-axis at a real angle..... | 84 |
| Figure 5.1.3-7 demonstrator Z-axis output | 85 |

| | |
|---|----|
| Figure 5.1.3-8 Inclinometer on platform | 86 |
| Figure 5.1.3-9 inclinometer X-axis recorded data | 86 |
| Figure 5.1.3-10 Inclinometer X-axis after clean data | 87 |
| Figure 5.1.3-11 Inclinometer on X-axis | 88 |
| Figure 5.1.3-12 angle data on Y-axis | 89 |
| Figure 5.1.3-13 Acc data on Y-axis | 90 |
| Figure 5.1.3-14 Acc data on Z-axis | 90 |
| Figure 5.1.3-15 gravity Acc showed on the Tilt Z-axis | 91 |
| Figure 5.1.3-16 Integrate gravity acc data | 92 |

Tables

| | |
|---|----|
| Table 2.3.1-1 General features of motor | 6 |
| Table 2.3.1-1 main tech indicators of Arduino UNO R3..... | 10 |
| Table 2.4.1-1 Features of laser vibrometer | 14 |
| Table 2.4.2-1 Features of Shaker | 18 |
| Table 3.1.2-1 Features of FOG | 21 |
| Table 3.2.2-1 Features of STIM318..... | 27 |
| Table 3.2.2-2 Features details | 30 |
| Table 3.2.3-1 cables and connector features | 31 |
| Table 4.1.2-1 Arduino UNO frequency calibration | 39 |
| Table 4.1.3-1 Screws used in the driver board..... | 39 |
| Table 4.1.3-2 Motor performance | 42 |
| Table 4.1.3-3 step angle resolution table | 43 |
| Table 4.1.3-4 workflows of motor | 43 |
| Table 4.1.4-1 Steps of data analysis..... | 48 |
| Table 5.1.1-1 GYRO Zaxis data | 53 |
| Table 5.1.1-2 Regression on GYRO Zaxis | 53 |
| Table 5.1.1-3 GYRO X-axis data..... | 55 |
| Table 5.1.1-4 GYRO data on Y-axis..... | 56 |
| Table 5.1.1-5 earth rotation data on Y-axis | 58 |
| Table 5.1.1-6 earth rotation data on Z-axis..... | 59 |
| Table 5.1.1-7earth rotation data on X-axis | 60 |
| Table 5.1.2-1 GYRO X-axis data..... | 63 |
| Table 5.1.2-2 GYRO X-axis regression..... | 64 |
| Table 5.1.2-3 IMU_GYRO_Yaxis data | 65 |
| Table 5.1.2-4 Regression of IMU GYRO Y-axis | 66 |
| Table 5.1.2-5 IMU GYRO z-axis data..... | 66 |
| Table 5.1.2-6 Regression on IMU GYRO z-axis..... | 67 |
| Table 5.1.2-7 IMU ACC gain of each axis | 70 |
| Table 5.1.2-8 IMU Acc X-axis 80Hz calculated data..... | 72 |
| Table 5.1.2-9 IMU Acc X-axis with 80Hz..... | 72 |

| | |
|--|----|
| Table 5.1.2-10 Regression of X-axis with 80Hz | 73 |
| Table 5.1.2-11 IMU Acc Y-axis 80Hz | 73 |
| Table 5.1.2-12 X-axis different frequency | 75 |
| Table 5.1.2-13 ACC Y-axis different frequency | 76 |
| Table 5.1.2-14 Acc z-axis different frequency | 77 |
| Table 5.1.2-15 Acc z-axis large frequency | 78 |
| Table 5.1.3-1 demonstrator gyro data on X-axis | 81 |
| Table 5.1.3-2 Demonstrator gyro data on Y-axis | 82 |
| Table 5.1.3-3 Demonstrator gyro z-axis | 85 |
| Table 5.1.3-4 Inclinometer data on X-axis | 88 |
| Table 5.1.3-5 Integrated gravity acceleration | 91 |

1 General introduction

1.1 Avionics

Avionics is a blend word. It is formed by taking half of the words aviation and electronic and splicing them together. The earliest available sources in avionics show that it came from a magazine called Aviation Week and Space Technology. The term avionics was coined by Philip J.Klass, the magazine's senior editor. Today, the sum of all the electronic systems on an airplane is called avionics. For example, the communication system, the navigation system, the display system, and so on are combined into one avionics system. [1]

In the decades of development so far, avionics systems have experienced four development stages: discrete, combined, integrated, and advanced integrated. The electronic systems installed on aircraft and the increasingly complex and diversified tasks carried by them are increasing in proportion and becoming more complex. Airborne avionics systems are playing an increasingly important role in improving aircraft performance. Whether it is general aircraft, transport aircraft, or military aircraft, the avionics system has gone through the development process from independent to combined and then to integrated.

A modern avionics system is a complex system composed of multiple subsystems, multiple environments, multiple tasks, and multiple resources, which are interrelated, mutually supportive, mutually integrated, and mutually restricted. It has the characteristics of multi-objective, multi-information, multi-specialty, multi-task, multi-function, multi-resource, and multi-process. How to achieve multi-objective composition, multi-information construction, multi-task composition, multi-function organization, multi-specialty configuration, multi-resource combination, multi-process support, and meet the needs of multiple functions, high quality, strong ability, and low cost are the challenges facing the new generation of avionics system. Given the increasingly complex avionics system, integrated technology has become one of the most concerning development aspects in this field.

Considering the next scenario, where the rapid evolution of urban mobility with the use of innovative small (up to 6 seats) aircraft and increasing use of unmanned aircraft, the SAIFE (Synthetic Air Data and Inertial Reference System) project, funded within the PoC instrument frame, proposes an "all-in-one" air data and inertial system (commonly known as ADAHRS) capable of providing multiple information to pilots, or automatic control systems, partially based on synthetic sensors. The solution proposed with the SAIFE project uses fewer physical sensors but at the same time guarantees the same reliability as modern aircraft in order to optimize the efficiency of onboard avionics for both future and modern aircraft. Under the SAIFE project, a flyable technological demonstrator will be developed to validate the flow angle synthetic sensors based on ASSE up to TRL (Technology Readiness Level)6 and verify performances offered by an ADAHRS based on synthetic flow angle sensors. In this thesis, we mainly discuss the performance and verification of the 3-axis gyroscope and 3-axis accelerometer in ADAHRS.

1.2 MEMS tech

MEMS (Micro-Electromechanical Systems), referred to as "micro-electromechanical Systems", is generally considered as a Micro system composed of Micro mechanical sensors, actuators, and micro-electronic circuits. Since microelectronics technology is a developed technology,

MEMS research and development is mainly focused on the research and development of micro mechanical sensors and actuators. MEMS devices and microfabrication technologies have three characteristics, Miniaturization, Microelectronics Integration, and Mass Fabrication with Precision, known as 3M for short. With the consumption upgrading of human society, MEMS technology has ushered in explosive growth. Various types of MEMS sensors have also been widely used in aerospace, petrochemical, shipbuilding, automobile, home, and medical and health fields.

Inertial sensors are devices that respond to physical motion, such as linear displacement or angular rotation, and convert this reaction into electrical signals that are amplified and processed by electronic circuits. Accelerometers and gyroscopes are the most common MEMS inertial sensors. An accelerometer is a sensor that senses axial acceleration and converts it into a usable output signal. A gyroscope is a sensor that can be sensitive to the angular velocity of a moving body relative to the inertial space. Three MEMS accelerometers and three MEMS gyroscope combinations form the Micro Inertial Measurement Unit (MIMU), which can be sensitive to linear acceleration in three directions and acceleration in three directions. The Inertial microsystem utilizes three-dimensional heterogeneous integration technology. The MEMS accelerometer, gyroscope, pressure sensor, magnetic sensor, signal processing circuit, and other functional parts are integrated into the silicon chip, and the built-in algorithm, to achieve chip-level guidance, navigation, positioning, and other functions.

MEMS accelerometer is one of the earliest sensors in the MEMS field. After years of development, MEMS accelerometer design and processing technology have become increasingly mature. According to the different sensitive mechanisms, MEMS accelerometer can be divided into piezoresistive type, thermal-flow type, resonant type, and a capacitance type. Piezoresistive MEMS accelerometer is easy to be affected by piezoresistive materials, which has serious temperature effect, low sensitivity, large transverse sensitivity, and low precision. The Thermal-flow accelerometer is limited by the characteristics of the heat transfer medium itself, the device frequency response is slow, the linearity is poor, easy to be affected by the external temperature. Therefore, thermal flow and piezoresistive accelerometers are mainly used for high G value measurement in civil or military fields where the accuracy is not high. The resonant micro accelerometer can achieve the accuracy of navigation in theory, but it cannot be applied in practice at present. The capacitive silicon micro accelerometer is the most mature and widely used MEMS accelerometer due to its high precision, mature technology, and strong environmental adaptability. With the improvement of MEMS processing capacity and ASIC circuit detection capacity, the accuracy of capacitive MEMS accelerometers is also constantly improving.

1.3 Backgrounds and goals

SAIFE (Synthetic Air Data and Inertial Reference System) is a miniaturized solution, suitable for modern aircraft, and can also be applied to UAVs and urban mobile aircraft. using the most advanced sensors to directly measure inertial and air data. Our goal was to test the performance of the fiber optic gyroscope and accelerometer on the SAIFE demonstrator, generating reliable conclusions. Firstly, the rotating platform was used to test the speed rate of the fiber optic gyroscope, and the Laser Vibrometer and Vibration Shaker were used to test the accelerometer. the three-axis gyroscope and three-axis accelerometer will be tested separately to verify their performance independently of the manufacturer's datasheets. Secondly, the fiber optic gyroscope and accelerometer are integrated into the SAIFE demonstration instrument. SAIFE

demonstrator will be tested in the laboratory using a rotating platform to verify angular rate and attitude, while a tilted platform is used to verify linear acceleration performance.

1.4 Literature review

A lot of research has been done in the field of fiber optic gyroscopes and accelerometers. Most of them focus on the performance testing and enhancement of both sensors. The use scenario is relatively single, and there are few applications and tests about the aviation field.

In the area of fiber optic gyroscope research,

[2]describes the performance capabilities of Honeywell Depolarized Gyros slated for large-scale production as an example of a high precision fiber optic gyroscope. this technology The technology has been shown to have excellent performance in military and space applications. It has been demonstrated that today's fiber-optic gyroscope technology can achieve a Scale Factor Stability of 30ppm and bias stability of 0.006 deg/s.

[3]proposed the use of neural networks to assist in the calibration of fiber optic gyroscopes. By establishing the error model and calibration model of the gyroscope, the working time and data processing time of the 3-axis rotating workbench used in the test of the fiber optic gyroscope is replaced in the traditional test to reduce the cost and improve the efficiency. However, the method should be tested using data measured on real FOG exposed to the desired operating conditions and environmental profile. The results should be compared with calibration results obtained using traditional calibration methods. Environmental stimulus profiles are also required, such as requirements for speed, temperature, and temperature gradient changes.

In the paper [4], the development and test results of a fiber optic gyro with a 0.01 degree/hour accuracy class are presented. The paper discusses gyroscope accuracy, stability of output characteristics, and other issues. The paper considers the development and test results of a navigation-level accuracy FOG with an erbium-doped fiber optic light source capable of providing three fiber optic loops for simultaneous operation. Each loop consists of a coil-hold single-mode fiber with polarization, a multifunctional integrated optical chip for beam phase modulation, and an electronic unit for controlling gyro signal processing in the closed-loop. Testing has confirmed that the FOG is accurate enough to serve as the basis for SINS to replace the moderately accurate shipboard gimbal INS.

In terms of accelerometer,

[5]have proposed a new calibration method for triaxial accelerometers. The method uses a mathematical model with six calibration parameters: three gain factors and three offsets. The basic principle of the proposed calibration method is that when the accelerometer is at rest, the sum of the output of the three-axis accelerometer is equal to the gravity vector. The proposed method requires placing the triaxial accelerometer at six different tilt angles to estimate six calibration parameters. Since the mathematical model of calibration parameters is nonlinear, an iterative method is used. The estimated gain factors and deviations are compared with the real gain factors and deviations, and the results are verified by simulation. The proposed calibration method was also experimentally tested using two different triaxial accelerometers, and the results were verified by a mechanical inclinometer. Experimental results show that the proposed method can estimate the gain factor and deviation accurately even if the initial guess is not close

to the true value. In addition, the method is simple in calculation and low in calculation cost, and the iterative method usually converges in three iterative steps.

[6]proposes a calibration technique for a triaxial accelerometer and a novel dynamic deviation filtering solution. Triaxial accelerometers are key components in a variety of applications, especially navigation systems. Non-ideal conditions such as scaling factors, cross-coupling, and deviations can affect the output of these sensors and often lead to errors, especially for sensitive and high-performance navigation systems. This proves that off-line calibration is a way to overcome these non-idealities. Simulation results show that the proposed algorithm has predictable performance and can calibrate the low-cost accelerometer unit. The method also evaluates the bias and gravity filters experimentally.

It can be seen from the above paper that the calibration of advanced sensors in the field of aviation has not been fully developed. Whereas previous papers focused on testing a single sensor, today's integrated aviation systems are complex. Therefore, it is very important to verify the 3-axis fiber optic gyroscope and 3-axis accelerometer in the SAIFE project.

2 Test facility

2.1 Test platform: FEDERAL MODEL FORMSCAN 3000 Roundness checker

The roundness meter is a precision instrument that measures the out-of-roundness of the rotating surface (shaft, hole, or sphere) of a part. There are usually two types: small table type, where the workpiece is mounted on a rotating worktable, and the measuring head is mounted on a fixed column; large floor type, where the work piece is mounted on a fixed worktable, and the measuring head is mounted on the rotating spindle. When measuring, the measuring head is in contact with the surface of the workpiece, and the rotating part (table or spindle) of the instrument rotates once. Due to the extremely high precision of the supporting bearing of the rotating part, the measuring head will produce a high-precision circular track on the surface to be measured when rotating. The out-of-roundness of the measured surface causes the measuring head to shift, which is converted into an electrical (or pneumatic) signal, and then amplified, can be automatically recorded on the circular recording paper, and the out-of-roundness of each part can be directly read for the accuracy of evaluation Used for process analysis. Widely used in precision bearings, machine tools, and instrument manufacturing industries

The machine we have contains Air Bearing Operated Rotary Table, Level, and Centering Knobs, Auto-Centering Computer, Roundness Plotter; 3 jaw chuck with adapter plate; Extra knobs, computing center, and auto-centering unit; 5 Extra Probes; 2 Extra Gage heads; Air regulator unit. We only use a part of it, the high-precision spindle rotating platform.



Figure 2.3.1-1 the whole equipment of the roundness checker



Figure 2.3.1-2 rotation platform

The rotating platform of the roundness checker has 4 adjusting screws, 2 adjusting the coaxiality, and 2 adjusting the horizontal of the platform. Normal gradienter are far from reaching the accuracy requirements, we use the dial indicator to make precise adjustments. [7]

2.2 Micro Stepper Motor

CRK series is a product of Oriental Motor Co., Ltd. Open-box micro-step driver is an important part of the product. This is a five-phase stepper motor, the driving function of the stepper motor is very stable. Compared with other stepper motors of the same type, it can produce larger torque, but at the same time, the vibration generated by the stepper motor in the process of operation is very small, which is a good reducer motor. Thanks to its stable and smooth operation function, the motor can perform micro-step drive within the driver without changing the pulse settings. From the overall effect, the stepper motor realizes low vibration and low noise operation.

In this experiment, the type of stepping motor we choose is. The information table of the motor is as follows:

Table 2.3.1-1 General features of motor

| | |
|---|---|
| <p>Model: PK564PMB</p> |  |
| <p>Basic step Angle: 0.36°/step</p> | |
| <p>5 Phase Double precision 24V DC power supply</p> | |

Because the stepper motor is a high-precision type, it should be noted that it should not be used in an environment that may have an explosion or corrosive liquid. Otherwise, it may lead to fire. The stepper motor will lose its torque when the power is turned off, which may cause some parts that depend on the motor to fall off, posing a risk of personal injury.

The following are some of the limitations and requirements of the stepper motor.

In the process of using the stepping motor, there are certain requirements for the load it can bear. When the load of the output bearing of the motor is too large, it means that the load has

exceeded the limit. If the modified load continues to act repeatedly on the output bearing of the stepping motor, it may cause motion fatigue of the stepping motor, and then lead to failure.

| | |
|--------------------|---|
| Radial Play | 0.025 mm max. of 5 N |
| Axial Play | 0.075 mm max. of 10 N |
| Radial Load | 0 mm from Shaft End = 90 N 5 mm from Shaft End = 100 N 10 mm from Shaft End = 130 N 15 mm from Shaft End = 180 N 20 mm from Shaft End = 270 N |
| Axial Load | 20 N |

2.3 MCU (Arduino)

In 2005 Massimo Banzi, a teacher at a high-tech design school in Ivrea, Italy, and David Cuartielles, a Spanish chip engineer, teamed up to create a circuit board that met the students' needs. The board was called Arduino. Arduino is a simple I/O platform based on open-source code, with a Processing/Wiring development environment similar to Java and C languages, and Arduino language can be used to cooperate with software such as Flash or Processing. To quickly develop interactive work.

As an electronic prototype platform, Arduino is composed of an open-source hardware platform based on a single-chip microcomputer and open source software that provides a programming interface and programming language. The development environment and programming language are clear and easy to master. Because of the open-source nature of Arduino, there are abundant hardware data such as Arduino circuit schematic diagram, PCB diagram, and all kinds of library files and other software data available on the network, which can be downloaded for free. Therefore, Arduino is highly scalable. Users can not only buy complete sets of Arduino products but also assemble Arduino development boards by themselves. They can also extend the Arduino programming language through C++ libraries. Arduino supports ICSP online burning, which can read a variety of switches and sensor signals and can well control a variety of physical devices such as indicator lights and motors. In addition, Arduino also carries out secondary compilation and packaging of the AVR library and packs each port, so that users can easily realize secondary development and developers can quickly make various products that meet the market demand (such as intelligent robot, intelligent wheelchair, heart rate monitor and other interesting and practical interactive products), which is very convenient and practical.

At present, there are many types of Arduino development boards on the market, each of which has obvious differences in appearance and is easy to identify. There are five common types:

1. Duemilanove series: a processor for ATMEL ATMEGA 168/328, can provide 14 digital interfaces, 6 straight insert board and 8 patch board analog interface, the use of FT232RL USB chip, is currently on the market the number of users, high-cost performance control board.

2. Nano series: The processor is also Atmel Atmega 168/328, can provide 14 digital interfaces, 14 analog interfaces, the same FT232RL USB chip, and Duemilanove series performance is completely the same, but the volume is more compact, in the circuit board size requirements of the occasion is very popular.

3. Leonardo series: Based on the ATmega32U4 microcontroller, it provides 20 digital interfaces, which is very different from the previous Arduino controllers. It directly uses the integrated USB AVR controller ATmega32U4, eliminating the need for USB to UART chip. Therefore, Leonardo can not only act as a virtual serial COM port on its own but also act like a mouse or keyboard to connect to a computer for use.

4. MINI series: The processor is still Atmel Atmega168/328, providing 14 digital interfaces and 8 analog interfaces, the smallest Arduino controller so far. Since the USB chip is not used, you must use an external downloader to download the program.

The latest Arduino panel model is the Arduino Uno R3. This version has been improved in all aspects as a result of efforts to improve the previous version: Firstly, the bug of the previous version was eliminated, the I2C bus interface was added, and the reset circuit design was improved. Then, the USB interface chip used Atmega16U2 to replace the previous version of Atmega8U2. It can work normally in Mac and Linux systems without installing the driver, and the function is more perfect and powerful. Therefore, this paper uses the Arduino Uno R3 development board to design the hardware circuit. The physical Arduino Uno R3 development board is shown in Figure 2.3-1:

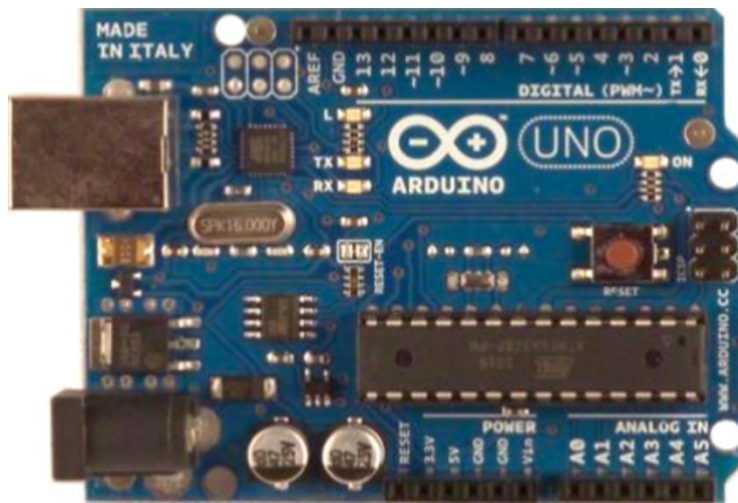


Figure 2.3.1-1 Arduino UNO R3

2.3.1 Arduino Uno R3 development board

The Arduino Uno R3 development board is not only easy to plug into common peripherals such as keyboard, mouse, joysticks, etc., but also perfectly compatible with any existing extension board. It can also adapt to new extension boards with its additional ports. Arduino Uno R3 has 14 digital I/O ports (6 channels for PWM output), 6 analog inputs, a 16MHz crystal oscillator, a USB interface, an ICSP header, a power socket, and a reset button. Pin labels are shown in

5V - The 5V chip on the Uno is powered by the 5V voltage flowing through the USB or regulator.

3.3V -- The voltage generated by the regulator is 3.3V, and the maximum driving current is 50mA.

GND -- Ground pin.

Reset -- Resets the SCM for low level.

AREF -- analog input signal reference voltage.

IOREF -- Expansion board can be compatible with 5V core board.

Table 2.3.1-1 main tech indicators of Arduino UNO R3

| THE MAIN TECHNICAL INDICATORS OF ARDUINO UNO R3 |
|--|
| Operating voltage: 5V |
| Input voltage: no need for the external power supply or external 7V~12V DC input when connected to USB |
| Output voltage: 5V DC output and 3.3V DC output and external power input |
| Microprocessor: ATmega328 |
| Bootloader: Arduino Uno |
| Clock frequency: 16 MHz |
| Input voltage (recommended): 7-12V |
| Input voltage (limit): 6-20V |
| Support USB interface protocol and power supply (no need for external power supply) |
| Support ISP download function |
| Flash memory: 32 KB (ATmega328) (0.5 KB for bootloader) |
| DC current I/O port 40mA |
| DC current 3.3V port 50mA |
| SRAM: 2 KB (ATmega328) |
| EEPROM: 1 KB (ATmega328) |

Arduino UNO R3 is a highly integrated and open-source control board. It provides users with circuit modules with common basic functions to the greatest extent. When it is necessary to implement user-defined features, there are also various types of extended versions to choose from.

2.3.2 Arduino language

Simply put, the Arduino language is the basic C language in which many parameters are processed functionally. The structure of the program written in Arduino language is simple, and it mainly includes the setup() function for initializing variables, setting the pin mode, and the loop execution function loop() similar to the main() function in C language. The Arduino language provides a variety of functions for users to use. Commonly used functions include definition functions for digital I/O port input and output modes, analog I/O port input and output functions, time and date functions, and mathematical functions. The Arduino language also provides a large number of official and unofficial library files, which users can download for free from the Internet. Commonly used official library files are:

(1) LiquidCrystal: LCD control program library file;

- (2) Servo: Servo control program library file;
- (3) SoftwareSerial: Digital I/O port analog serial port program library file;
- (4) Stepper: stepper motor control program library file;
- (5) Wire: TWI/I2C bus library file.

2.3.3 Arduino development environment setup

The construction of the Arduino development environment includes: Arduino main control board installation, USB driver installation of Arduino circuit, Arduino C language integrated development environment installation.

The control program development software Arduino IDE provided by Arduino can be downloaded directly from <https://www.arduino.cc/en/software>. Users can download different versions of Arduino IDE according to different operating platforms.

Before connecting the Arduino UNO development board to the PC, you must first ensure that the Arduino IDE is installed on the PC. The Arduino UNO R3 development board communicates and supplies power to the PC via USB cable type A/B. Connect your Uno board with an A B USB cable; sometimes this cable is called a USB printer cable.

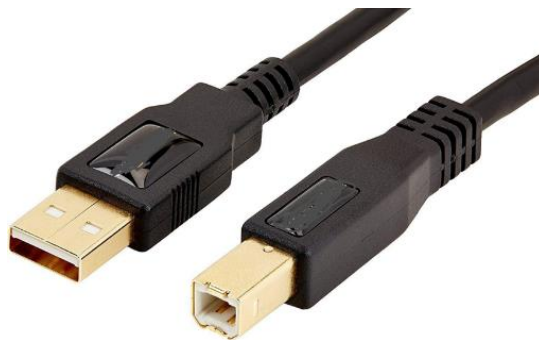


Figure 2.3.3-1 Arduino UNO connecting cables

The USB connection with the PC is necessary to program the board and not just to power it up. The Uno automatically draws power from either the USB or an external power supply. Connect the board to your computer using the USB cable. The green power LED (labeled PWR) should go on.

Generally, PC will install drivers automatically as soon as you connect the Arduino UNO board. [8]

If you downloaded and expanded the Zip package or, for some reason, the board wasn't properly recognized, please follow the procedure below.

1. Click on the Start Menu, and open up the Control Panel.
2. While in the Control Panel, navigate to System and Security. Next, click on System. Once the System window is up, open the Device Manager.
3. Look under Ports (COM & LPT). You should see an open port named "Arduino UNO (COMxx)". If there is no COM & LPT section, look under "Other Devices" for "Unknown Device".

4. Right-click on the "Arduino UNO (COMxx)" port and choose the "Update Driver Software" option.
5. Next, choose the "Browse my computer for Driver software" option.
6. Finally, navigate to and select the driver file named "Arduino.inf", located in the "Drivers" folder of the Arduino Software download (not the "FTDI USB Drivers" sub-directory). If you are using an old version of the IDE (1.0.3 or older), choose the Uno driver file named "Arduino UNO.inf"
7. Windows will finish up the driver installation from there.

2.4 Accelerometer calibration facility

2.4.1 Laser Vibrometer

Polytec CLV-2534 is a vibration analyzer, it can detect the distance range of 0.2m-2m. It using the non-contact measurement method, you only need to hit the laser spot on the point of interest to obtain the physical quantities such as the transfer function, amplitude, and resonance frequency of the point. This vibrometer mainly serves some non-contact high-precision measurements. The device has a micron-level probe, which has a longer measuring distance and higher accuracy. The laser probe of the device can produce a spot with a diameter of 1.5 microns, and the user can adjust the test device by visual observation. With extremely high optical sensitivity and convenient operability, this vibrometer can handle many harsh environments, bringing reliable quality assurance for research or industrial development.

The laser Doppler vibration measurement technology was first developed from the laser velocity measurement technology. Its physical principle is that the reflected light reflected from a moving object will have the vibration characteristics of the moving object itself, that is, Doppler frequency shift.

$$\Delta f_D = \frac{2Vf}{c} = \frac{2V}{\lambda}$$

In the formula, Δf_D represents the Doppler frequency shift that occurs after the laser is reflected by a vibrating object, V is the moving speed of the object, and λ is the wavelength of the laser. It can be seen that the principle of laser Doppler vibration measurement is based on measuring the Doppler frequency Δf_D of the coherent laser light reflected from a small area on the surface of the object, and then determining the vibration velocity V of the measurement point.

Based on the above basic optical theory, the principle of vibration measurement is shown in Figure 3.2.1.1-1, The laser beam with frequency f emitted by the laser is incident on the surface to be measured through the beam splitter. Due to the vibration of the measurement surface, the reflected light will produce a Doppler frequency shift Δf_D , The reference beam with the frequency $f + f_r$ and the reflected light with the frequency $f + \Delta f_D$ are reflected by the mirror and projected on the photodetector to generate the beat signal. After the electronic signal processing system, the beat frequency of $\Delta f_D - f_r$ is finally obtained. For the electrical signal, since the increased f_r of the reference beam is known, the desired object vibration signal can be obtained by analyzing and processing the output signal of the laser Doppler vibrometer

$\Delta f_D - f_r$. Because the output signal of the photodetector is mixed with the reference beam with known direction and frequency, it can distinguish the information reflecting the vibration characteristics of the object itself, such as the direction of motion of the measured surface, the amplitude of motion (that is, the magnitude of displacement), and the frequency of motion.

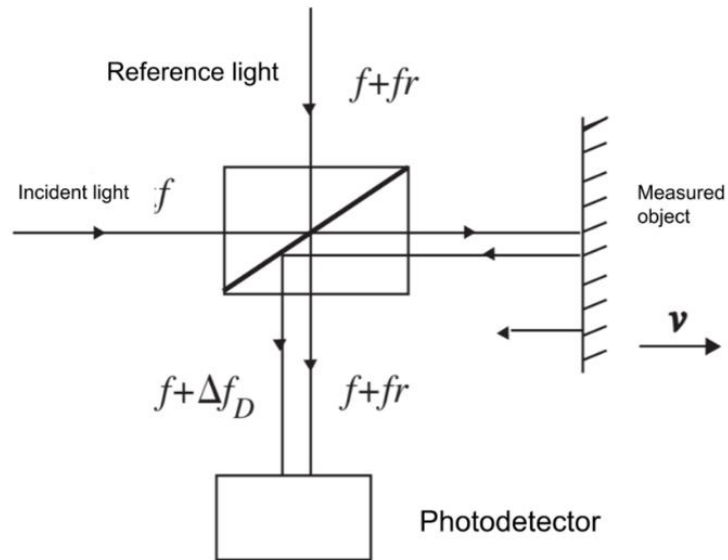


Figure 2.4.1-1 Description drawing

The vibrometer uses laser detection, which is conducted by optical fibers to provide laser power. The device can make positioning and installation convenient without affecting measurement accuracy. On the other hand, the vibrometer integrates a signal processor, laser interferometer, and power supply into a controller. The standard Laser safety used by this vibrometer is IEC/EN 60825-1 (CFR 1040.10, CFR 1040.11), during the test, I don't need to wear goggles. [9]



Figure 2.4.1-2 laser vibrometer controller

Table 2.4.1-1 Features of laser vibrometer

| Compact Sensor Head Specifications | |
|---|--|
| Laser type | Helium neon (HeNe) |
| distance | -----, -----, -----, |
| Minimum spot diameter | 1.5 µm (with VIB-A-20xLENS 20X objective) |
| Maxima of visibility | 295 mm + n · 204 mm; n = 0; 1; 2; ... |
| General Specifications | |
| Dimensions (L x W x H) | Vibrometer Controller: 450 mm x 355 mm x 150 mm (17.7 in x 14.0 in x 5.9 in) Compact Sensor Head: 201 mm x 38 mm x 71 mm (7.9 in x 1.5 in x 2.8 in) |
| Weight | Vibrometer Controller: 11 kg (24.3 lbs) Compact Sensor Head: 0.8 kg (1.8 lbs) |
| Housing protection | Vibrometer Controller: I (protective grounding) Compact Sensor Head: IP64 standard |
| Power | 100 VAC ... 240 VAC ±10 %, 50/60 Hz, max. 75 W |
| Ambient temperature | +5 °C ... +40 °C (41 °F ... 104 °F) |
| Storage temperature | -10 °C ... +65 °C (14 °F ... 149 °F) |
| Relative humidity | max. 80 %, non-condensing |
| Optical cable length | 3 m (Controller to Compact Sensor Head) |
| Output voltage | ±10 V |
| Interfaces | RS-232, max. 115 kBd, serial interface for vibrometer controller |
| Filter | High pass filter: 100 Hz/off Low pass filter: 5 kHz/20 kHz/100 kHz/off Tracking filter: slow/fast/off (CLV-2534-2) |

Here is the test platform build:

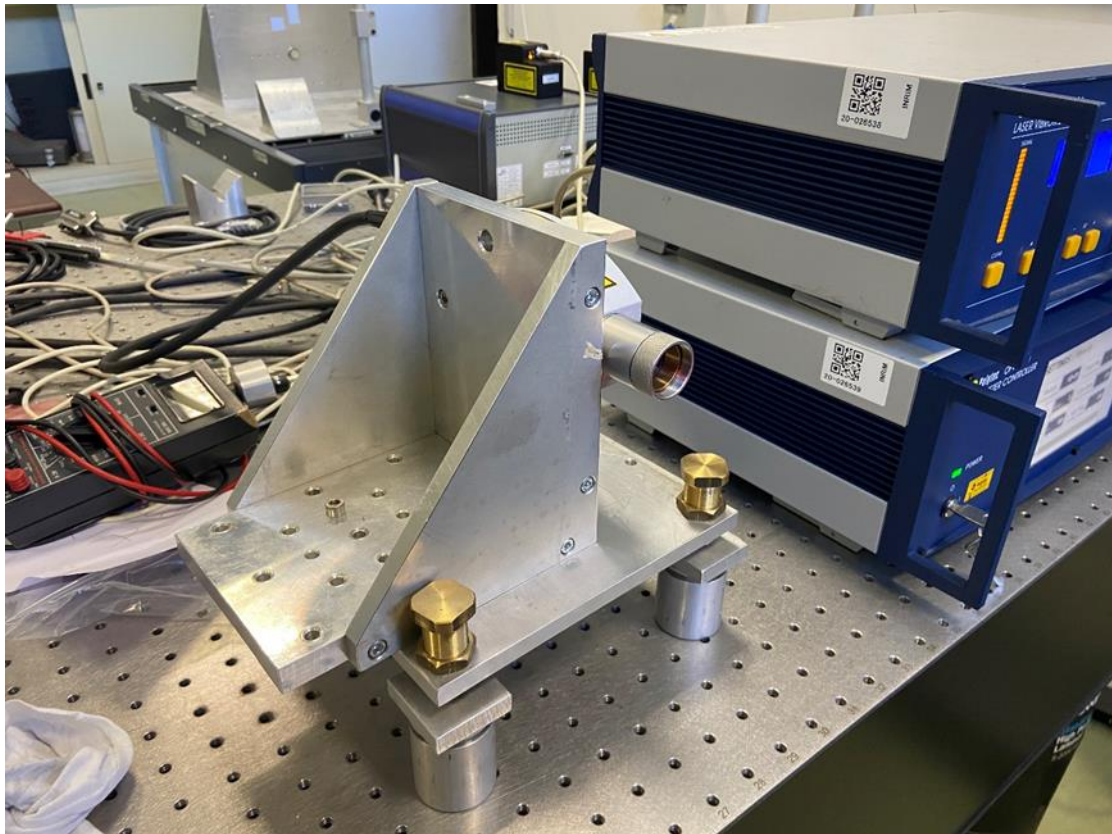


Figure 2.4.1-3 leaser probe



Figure 2.4.1-4 controllers on platform

2.4.2 Vibration Shaker

TMS Shaker 2075E. According to the basic principles of electromagnetics, in principle, the vibrating table and the loudspeaker use the same principle. According to Faraday's law, when a current-carrying conductor passes through a magnetic field, it will receive an electromotive force. Its direction conforms to Fleming's left-hand rule. The force, current and magnetic field are perpendicular to each other. Proportional. When the voice coil inputs an alternating audio current, the voice coil is subjected to an alternating driving force to produce alternating motion, which drives the diaphragm to vibrate, and repeatedly pushes the air to produce sound.

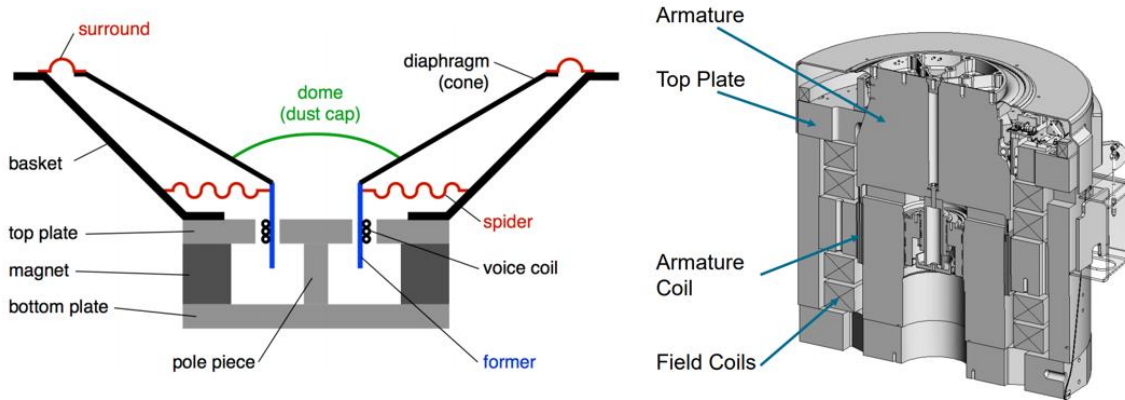


Figure 2.4.2-1 Speaker and shaker

Fleming's left-hand rule: When current flows through a conducting wire, and an external magnetic field is applied across that flow, the conducting wire experiences a force perpendicular both to that field and to the direction of the current flow (i.e they are mutually perpendicular). A left hand can be held, as shown in the illustration, so as to represent three mutually orthogonal axes on the thumb, fore finger, and middle finger. Each finger is then assigned to a quantity (mechanical force, magnetic field, electric current). The right and left hands are used for generators and motors respectively. All three directions are represented by the thumb (for thrust or motion), forefinger (for field), and second finger (for current direction), all held at right angles to each other.

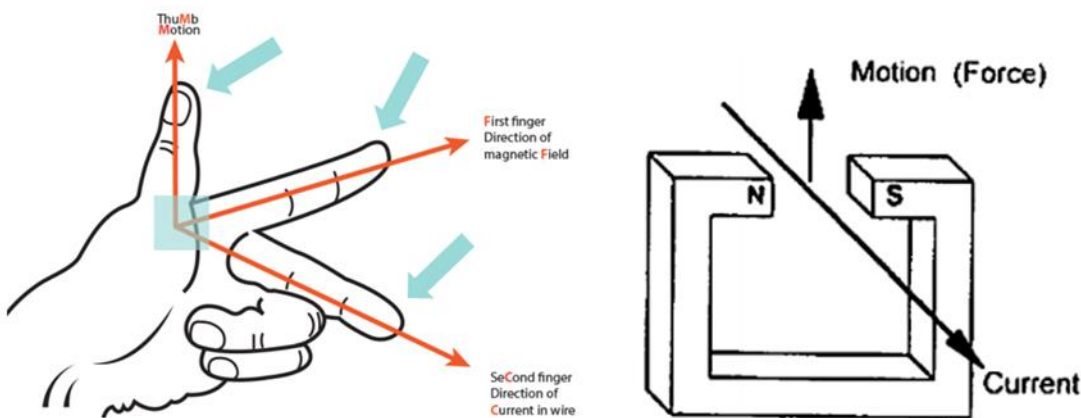


Figure 2.4.2-2 Left-hand rules

Modal Shop's 2075E dual-purpose shaker is a permanent magnet shaker, it is an ideal test platform for testing the vibration of a single component or assembly. And its small size does not prevent it from having powerful functions. It can provide up to 334N sinusoidal output power. The shaker has a round table with a diameter of 8.3cm, which can carry a load of up to 3.2KG. [10]

The vibrating table is installed on the trunnion. The trunnion is a simple support base structure that allows the vibrator to be oriented (between or at an angle) horizontally or vertically. In this test, because the STIM318 sensor is very small. Therefore, I do not need to use the trunnion to adjust the tilt angle of the shaker but test by changing the angle of the sensor. Based on the above considerations, removing the trunnion is a better choice. In this case, the shaker can be kept vertical if it is tightly fixed on a horizontally calibrated laboratory platform. The shaker is directly connected with the platform to maintain stability to reduce errors.

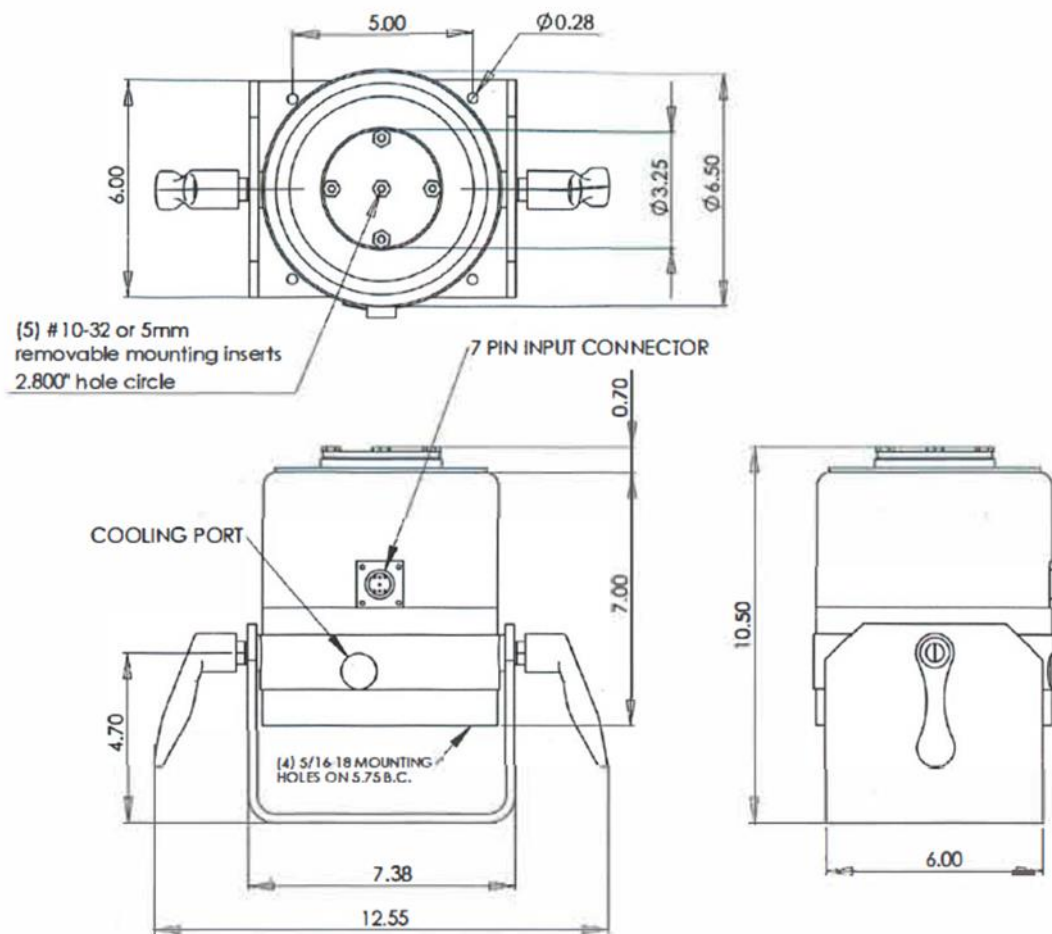


Figure 2.4.2-3 Engineering drawing of shaker

Table 2.4.2-1 Features of Shaker

| PERFORMANCE | | |
|------------------------------------|----------------------------|--------------------------------------|
| Sine Force | | |
| Natural Air Cooling | lbf pk (N pk) | 40 (178) |
| With Forced Air Cooling | lbf pk (N pk) | 75 (334) |
| Random Force | | |
| Natural Air Cooling | lbf rms (N rms) | 17 (76) |
| With Forced Air Cooling | lbf rms (N rms) | 28 (125) |
| Shock Force (50 ms) | lbf pk (N pk) | 75 (334) |
| Max. Displacement | | |
| Continuous pk-pk | in (mm) | 1.0 (25) |
| Between Stops | in (mm) | 1.03 (26) |
| Frequency Range ¹ | Hz | DC-6500 |
| Fundamental Resonance ¹ | Hz | > 4000 |
| Maximum Velocity | ips pk (m/s pk) | 70 (1.8) |
| Acceleration ^{1,2} | | |
| Bare Table | g pk | 75 |
| 1 lb load | g pk | 38 |
| 5 lb load | g pk | 12 |
| Maximum Acceleration | | |
| Resonance | g pk | 120 |
| Peak Shock | g pk | 150 |
| PHYSICAL | | |
| Armature Weight | lb (kg) | 1.0 (0.454) |
| Suspension Stiffness | lbf/in (N/mm) | 60 (10.5) |
| Rated Drive Current | | |
| Natural Cooling | A rms | 11 |
| With Cooling Vacuum | A rms | 22 |
| Stray Magnetic Field | | |
| 1.5" above table | Gauss | <15 |
| 1.0" from body | Gauss | <20 |
| Cooling Air | cfm/15 in H ₂ O | 100 |
| Dimensions | in (mm) HxWxD | 10.5 x 12.55 x 6.5 (267 x 319 x 165) |
| Shaker Weight | lbs (kg) | 35 (16) |

In the shaker test platform, I used a maximum acceleration of 10g and measured in three directions of the sensor, the X-axis, Y-axis, and Z-axis.

3 Devices under test

3.1 KVH Gyroscope 1760-3axis

Fiber optic gyroscope (FOG) is very sensitive to changes in direction, so it can realize the functions of a traditional mechanical gyroscope. The concept of FOG was born. Dating back to 1976, this concept was proposed by Vali and Shortill. Fiber optic gyroscopes can provide very precise rotation information. The vibration, acceleration, and shock generated between the shafts will not have a great impact on the FOG. Compared with traditional inertial spinning gyroscopes, FOG can determine the current state of rotation without moving parts. This makes it not dependent on the inertia of motion. Therefore, FOG is very reliable and can be used in high-performance aerospace. In the field of aviation, military science and technology, and navigation, FOG has a wide range of applications.

The name of the fiber optic gyroscope includes fiber. As the name implies, the fiber optic gyroscope contains a fiber with a length of 5 kilometers. The interference produced when a

beam of light passes through a 5 km fiber optic coil is what the fiber optic gyroscope relies on. At both ends of the same optical fiber, two beams of light are emitted and injected into the optical fiber at the same time. As we all know, the speed of light is fixed. If the fiber optic gyroscope rotates, the path of one beam of light will be slightly longer than that of the other beam. In this optical fiber, there is a phase difference between the two beams, and the interferometer can be used to detect the phase difference between the two beams. The principle of this method is called the Sagnik effect. In this way, the angular velocity component can be converted into a change in the interference pattern that can be measured by the photodetector. Since the 1970s, the rapid development of semiconductor lasers and the rapid development of low-loss single-mode fibers. More and more researchers are beginning to apply the Sagnik effect.

3.1.1 Working principle

The fiber optic gyroscope is a fiber-optic Sagnac interferometer based on the Sagnac effect. As shown in Figure xxx, the light beam emitted by the light source is divided into two by a beam splitter. The two ends merge into the light-sensitive coils, propagate in the clockwise and counterclockwise directions respectively, and return to the beam splitter and superimpose to produce interference. When the circular optical path is stationary relative to the inertial space, the optical path in clockwise and counterclockwise directions is equal. [11]When the angular velocity Ω is rotated relative to the inertial reference frame, due to the existence of Ω , the two beams of light propagating in the clockwise and counterclockwise directions produce an optical path difference ΔL , and ΔL causes a phase difference $\Delta\phi$, so only the phase is measured. The difference $\Delta\phi$, we can know the rotational angular velocity Ω of the loop relative to the inertial space, and the relationship between the phase difference $\Delta\phi$ and the rotational angular velocity Ω will be derived below:

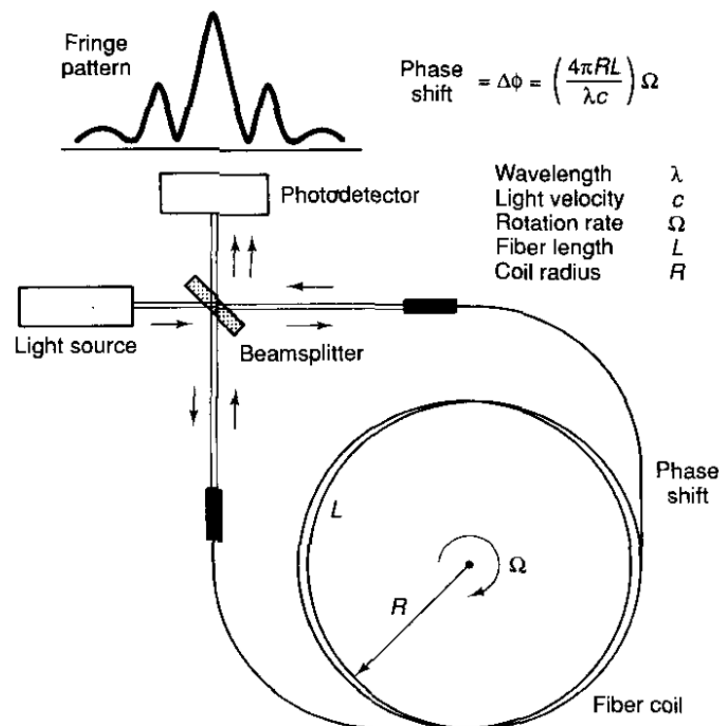


Figure 3.1.1-1 Schematic diagram of FOG

$$V_{cw} = \frac{\frac{2c}{n} + D\Omega}{2 + \frac{D\Omega}{nc}}$$

$$V_{ccw} = \frac{\frac{2c}{n} - D\Omega}{2 - \frac{D\Omega}{nc}}$$

Among them, V_{cw} is the propagation speed of light in the clockwise direction, and V_{ccw} is the propagation speed of light in the counterclockwise direction. Then the propagation times of the two beams of light in the fiber ring are:

$$t_{cw} = \frac{2\pi D(2nc + D\Omega)}{4c^2 - (D\Omega)^2} \approx \frac{\pi D(2nc + D\Omega)}{2c^2}$$

$$t_{ccw} = \frac{2\pi D(2nc - D\Omega)}{4c^2 - (D\Omega)^2} \approx \frac{\pi D(2nc - D\Omega)}{2c^2}$$

The resulting time difference Δt is:

$$\Delta t = \frac{\pi D^2}{c^2} \Omega = \frac{4A}{c^2} \Omega$$

Optical path difference ΔL :

$$\Delta L = \frac{\pi D^2}{c} \Omega = \frac{4A}{c} \Omega$$

In the formula, A is the area enclosed by the circular light path, the unit is m^2 .

When the circular optical path is composed of N circles of fibers, the corresponding optical path difference is:

$$\Delta L = \frac{4NA}{c} \Omega$$

The phase difference of the clockwise and counterclockwise beam can be obtained from the optical path difference ΔL :

$$\Delta\phi = \frac{2\pi\Delta L}{\lambda} = \frac{8\pi NA}{\lambda c} \Omega = \frac{4\pi RLN}{\lambda c} \Omega$$

In the formula:

λ — — — *Wavelength of light*

L — — — *Fiber ring circumference*

Obviously, the angular velocity $\Delta\phi$ can be obtained by detecting the phase difference Ω (that is, the intensity of the interference light). Among them, $K = 4\pi RLN/\lambda c$ is the scale factor of the gyroscope. It can also be seen from the formula that the phase difference $\Delta\phi$ is proportional to the rotation speed Ω of the fiber ring. In the case of a certain fiber coil, the fiber can be increased by increasing the number of coil turns. The total length of the coil is used to improve the sensitivity of the measurement.

3.1.2 Features

KVH's DSP-1760 fiber optic gyroscope has extremely high sensitivity and stability. It performs very well in both bias stability and Angle random walk. From single axis to multi-axis, encapsulated or not encapsulated. Both have a very high degree of freedom, can be selected according to the specific project. The following are some characteristic parameters of the fiber optic gyroscope: [12]

Table 3.1.2-1 Features of FOG

| Performance Specifications | |
|--|---|
| Input Rate (max) | $\pm 490^\circ/\text{sec}$ |
| Bias Instability (25°C) | $\leq 0.1^\circ/\text{hr}$, 1 σ (max), $\leq 0.05^\circ/\text{hr}$, 1 σ (typical) |
| Bias vs. Temperature ($\leq 1^\circ\text{C}/\text{min}$) | $\leq 1.5^\circ/\text{hr}$, 1 σ (max), $\leq 1^\circ/\text{hr}$, 1 σ (typical) |
| Bias Offset (25°C) | $\pm 2^\circ/\text{hr}$ |
| Scale Factor Non-linearity (full rate, 25°C) | ≤ 50 ppm, 1 σ |
| Scale Factor vs. Temperature ($\leq 1^\circ\text{C}/\text{min}$) | ≤ 200 ppm, 1 σ (max), ≤ 100 ppm, 1 σ (typical) |
| Angle Random Walk (25°C) | $\leq 0.012^\circ/\sqrt{\text{hr}}$ (0.7 $^\circ/\text{hr}/\sqrt{\text{Hz}}$) |
| Bandwidth (-3 dB) | Housed: ≥ 440 Hz Unhoused: ≥ 1000 Hz |

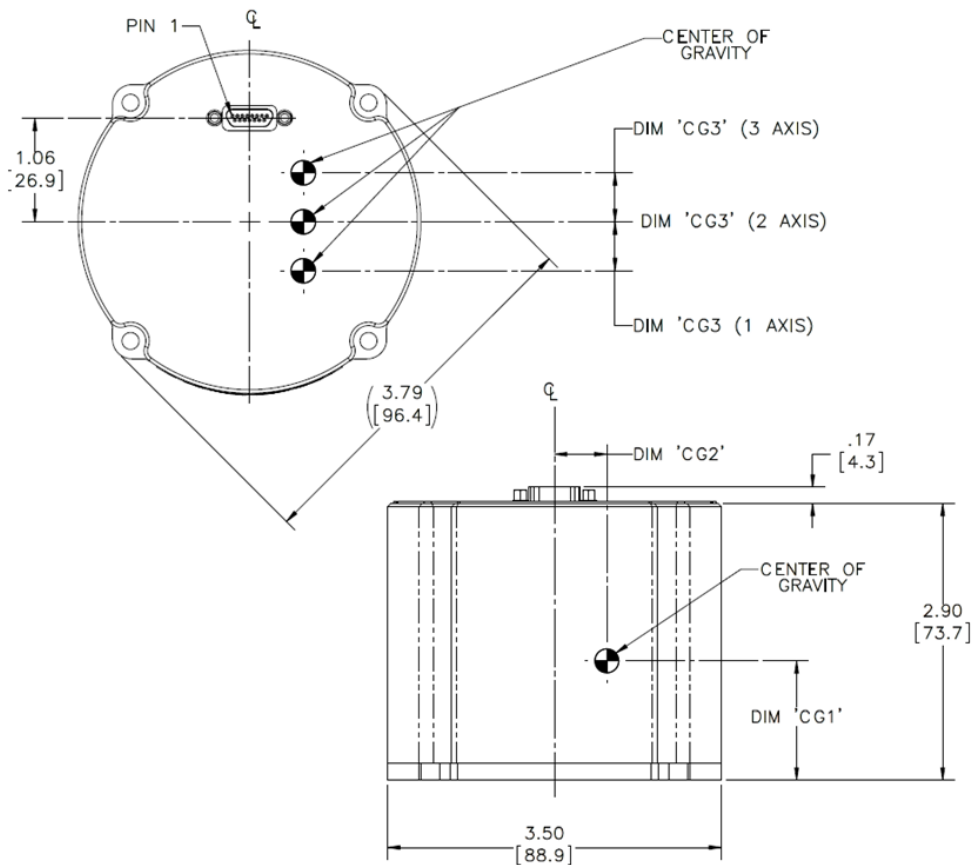


Figure 3.1.2-1 FOG engineering drawing

In our project, we purchased a 3-axis fiber optic gyroscope, the interface type is a 15-socket (female) Micro-D connector, using MIL-DTL-83513 as the standard. Military-level application standards make the fiber optic gyroscope perform well and reliable even under extreme conditions.

3.1.3 Development software

I use the development kit from the KVH company. A set of developer tools is included in the list of buying fiber optic gyroscopes, and using official software is one of the most reliable methods. The sensor interface communication protocol we choose is RS422. To communicate with the PC, a conversion cable is necessary. As shown in the figure, the cable to the fiber optic gyroscope is a Y-type cable, one end of which can be connected to the micro-D interface of the fiber optic gyroscope for communication, and the other end is used as a power supply cable for the fiber optic gyroscope. Connect the micro-D interface of the optical fiber sensor to the data board, and the other side of the data board uses a USB interface for output, which can be connected to a PC.

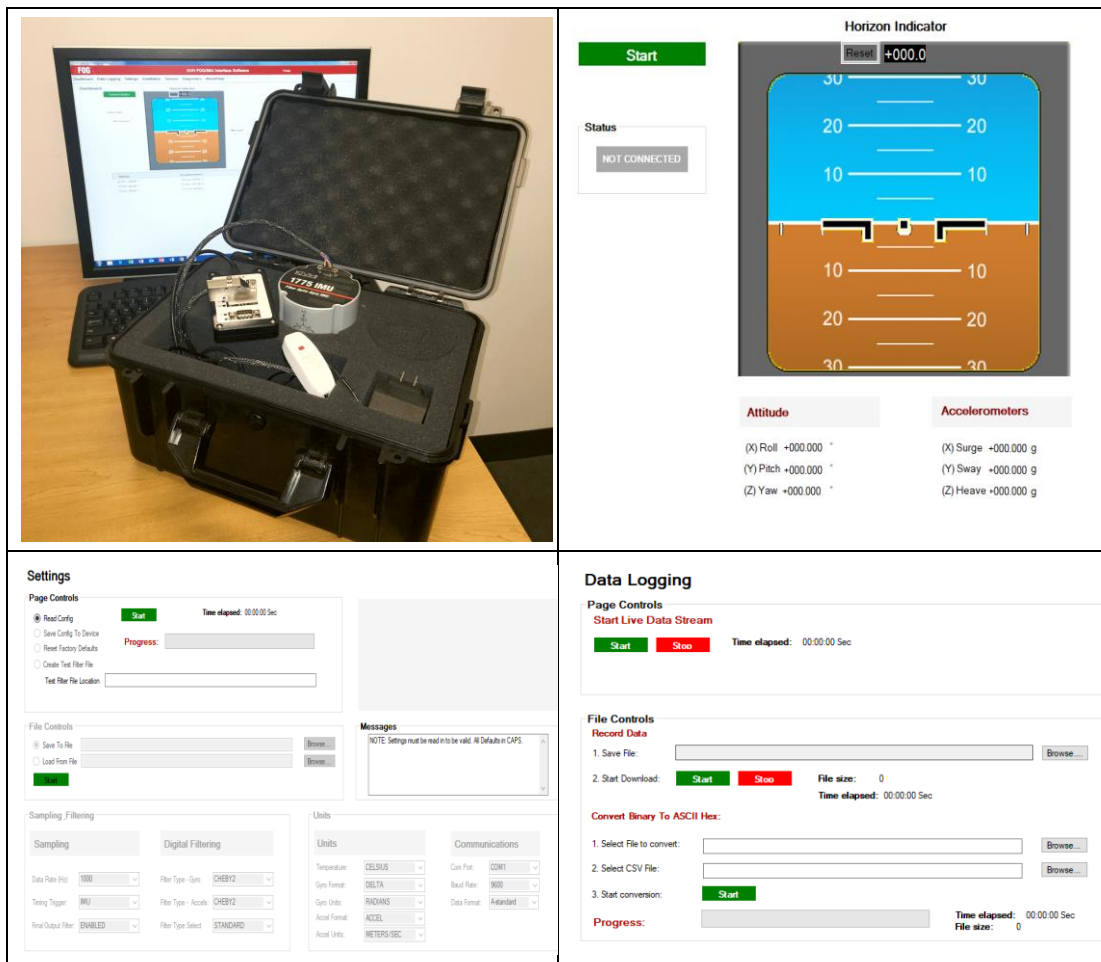


Figure 3.1.3-1 Development software layout

After entering the software, I can see a simulation animation window on the dashboard. When the fiber optic gyroscope is connected, it can display the current status of the gyroscope in real-time. What are the values of yaw, pitch, and roll. In the setting interface, I can select the frequency of data sampling, the highest can be 1000Hz, that is, data is collected every 1 millisecond. You can also set the type and frequency of the low-pass filter to achieve the best results. By default, the data storage format of the fiber optic gyroscope is binary. In order to

visually see the data on the PC side, the software can convert the binary data into ASCII Hex, and the storage format is a CSV file. It can be directly opened and processed through EXCEL. This is very convenient for us to check the test data.

3.2 STIM318 IMU

3.2.1 Work principle

3.2.1.1 Working principle of micromechanical gyroscope

A gyroscope is a kind of instrument that can directly measure the angular velocity of an object. It is designed based on the theory of angular momentum conservation. There are two main measuring principles of a mechanical gyroscope: one is to measure the angular velocity by using the azimuth stability characteristic of a high-speed rotating mechanism in inertial space; the other is to measure the angular velocity by using the Coriolis force generated by high-speed resonant vibration element when rotating. MEMS gyroscope belongs to the latter measurement principle, it is the main characteristic of small volume, light weight, low cost, good reliability, wide measurement range, with the continuous development of MEMS technology, the lower cost of MEMS gyroscope accuracy is higher and higher, has been widely used in mobile equipment, medical equipment, small drone, such as indoor positioning emerging field. [13]

In general, the working principle of the traditional gyroscope is based on the law of conservation of angular momentum. The core idea is as follows: when the torque m of the external force exerted by the particle \vec{M} on a certain reference point, O is zero, then the particle is opposite the point The time rate of change of angular momentum of $d\vec{L}/dt$ is also zero.

MEMS inertial gyroscope is different from the traditional gyroscope, its working principle is based on the elder brother's effect, its core idea is: when the mass point m along a straight line in the two-dimensional plane do harmonic vibration, and the two-dimensional plane perpendicular to the axis of the two-dimensional plane rotates, particle m due to from the force perpendicular to the line direction, also do harmonic vibration. The MEMS inertial gyroscope can indirectly measure the Coriolis acceleration measure by sensing the Coriolis force on the particle M .

As shown in Fig. 3.2.1-1, the dynamic coordinate system of particle M was established, and the acceleration of particle M was calculated through the following derivation, and then the radial acceleration, centripetal acceleration, and Coriolis acceleration of particle M were deduced.

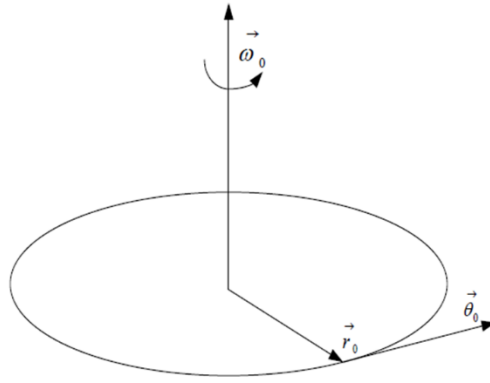


Figure 3.2.1-1 Dynamic coordinate system of particle motion in Coriolis effect

The detailed calculation formula is as follows:

$$\vec{r} = r\vec{r}_0$$

$$\vec{q}_0 = \vec{\omega}_0 \times \vec{r}_0$$

$$\frac{d\vec{r}}{dt} = v_r\vec{r}_0 + r\frac{d\vec{r}_0}{dt} = v_r\vec{r}_0 \times \vec{\omega}$$

$$\frac{d^2\vec{r}}{dt^2} = a_r\vec{r}_0 - 2v_r\vec{r}_0 \times \vec{\omega} - \omega r^2\vec{r}_0$$

$$a_{Coriolis} = -2v_r\vec{r}_0 \times \vec{\omega}$$

According to the above five calculation formulas, it can be obtained that when the Coriolis acceleration of a particle M is equal to zero, it has no radial motion on the circumference.

A gyroscope, usually a MEMS inertial gyroscope, consists of two resonators in the form of sinusoidal oscillations. The internal simplified model of MEMS inertial gyroscope can be regarded as the mass-stiffness-damping coefficient system in Figure 3.2.1.1-3

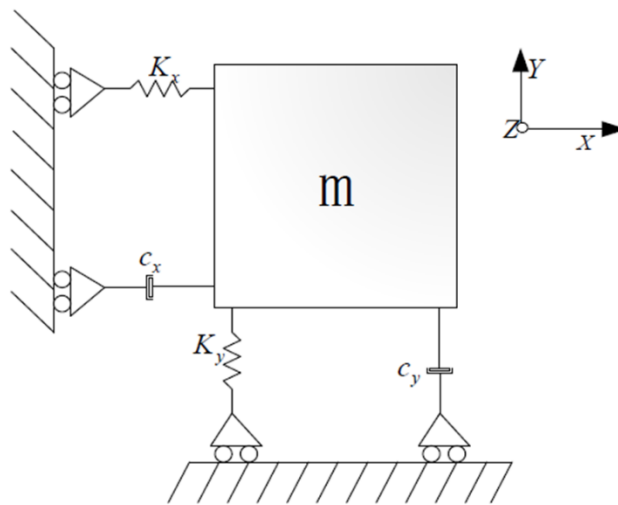


Figure 3.2.1-2 Simplified diagram of internal structure model of MEMS inertial gyroscope

If the MEMS inertial gyroscope is not subjected to any other non-measurement interference from the outside world, the dynamic model of the MEMS inertial gyroscope can be expressed by the following two second-order linear differential equations:

$$mx''(t) + c_x x'(t) + k_x x(t) = f_d$$

$$my''(t) + c_y y'(t) + k_y y(t) = f_c = 2m\Omega(t)x'(t)$$

Among them, in the above two formulas, the electrostatic driving force is f_d , the Coriolis effect force is f_c , the system input angular velocity $\Omega(t)$, and the coefficients k_x and k_y are calculated as follows:

$$k_x = \omega_x^2 m, k_y = \omega_y^2 m$$

Among them, in the formula, ω_x is the resonant frequency of the system in the X-axis direction, and ω_y is the resonant frequency of the system in the Y-axis direction.

$$a_{Coriolis} = -2v_r \vec{r}_0 \times \vec{\omega}$$

The detailed calculation formulas of c and y c are as follows:

$$c_x = \frac{\omega_x m}{Q_x} = 2\xi_x \omega_x m$$

$$c_y = \frac{\omega_y m}{Q_y} = 2\xi_y \omega_y m$$

Among them, in equations, the resonance frequency, quality factor, and damping coefficient of the system in the X-axis direction are ω_x , Q_x and ξ_x respectively. Similarly, the system's resonance frequency in the Y-axis direction the resonance frequency, quality factor, and damping coefficient are ω_y , Q_y and ξ_y respectively.

3.2.1.2 Working principle of micromechanical accelerometer

We usually define an accelerometer as a sensor that can output acceleration data in real-time. It can measure acceleration physical quantity and convert it into corresponding electrical physical quantity output in real-time. With the continuous maturity of the manufacturing process, the precision of MEMS inertial devices is also improving, and the performance of the MEMS accelerometer is also improving, the volume is getting smaller and the performance is becoming more stable. MEMS accelerometer can be divided into resonant type, piezoresistive type, servo type, capacitive type, and tunnel type according to the different working principles. Different accelerometers have significant differences in their structures, and their stability and accuracy are different. In terms of precision, servo type and tunnel type have good performance, but the production and manufacturing process is cumbersome, the cost of the materials used is high, the higher cost is not conducive to widespread promotion.

At the same time, the servo-type and tunnel-type accelerometers are used in a single environment, which restricts their development and use. At present, the mainstream MEMS accelerometer is mainly capacitive. Its manufacturing cost is not only low, but also its manufacturing structure is simple and reliable, and it has a high-cost performance. It can adapt to various working environments and has been widely used in various fields. Especially in

aerospace, strap-down inertial navigation, attitude, and positioning measurement, capacitive MEMS accelerometer is used as the core measurement device.

The construction principle of the MEMS accelerometer is to measure the physical quantity of acceleration based on Newton's law of inertia by using physical knowledge. According to Newton's second law of inertia, the corresponding particle acceleration is as follows by using the mass block's sensitive acceleration physical quantity:

$$F = \frac{dP}{dt} = \frac{d(Mv)}{dt} = Ma$$

A mass block, which interacts with the spring due to the axial acceleration of the sensitive motion, is usually integrated into the micromechanical accelerometer. The spring supports the mass block on the damper. Under the condition of known elastic coefficient and damping coefficient of the spring, we calculate according to the following motion formula. We define the damping coefficient as D and the elastic coefficient as k_s .

$$M \frac{d^2x}{dt^2} + D \frac{dx}{dt} + k_s x = -Ma$$

Through Laplace transform, the transfer function $H(s)$ of the accelerometer can be written as:

$$H(s) = \frac{x(s)}{a(s)} = \frac{1}{s^2 + \frac{D}{M}s + \frac{k_s}{M}} = \frac{1}{s^2 + \frac{\omega_0}{Q} + \omega_0^2}$$

$\omega_0 = \sqrt{k_s/M}$ is the angular frequency, and $Q = \sqrt{\frac{k_s/M}{D}}$ is the quality factor.

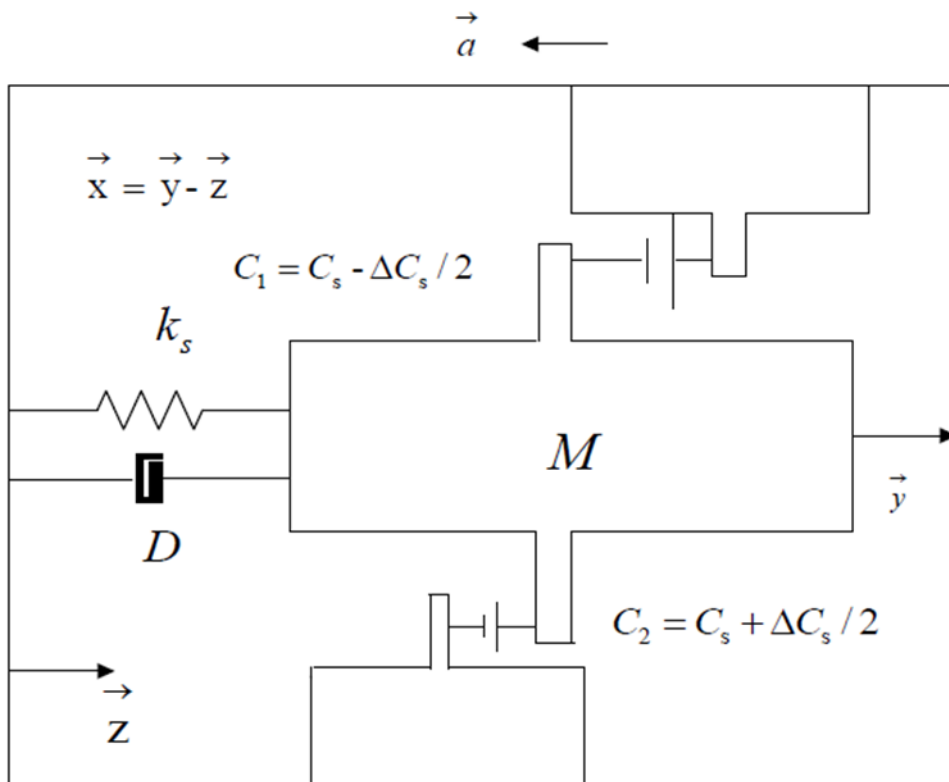


Figure 3.2.1-3 Schematic diagram of MEMS accelerometer principle

As shown in Figure 2.3 above, it is a schematic diagram of the principle of the accelerometer. For the elastic coefficient k_s there are:

$$k_s = k_m - k_e$$

Where k_m and k_e are the mechanical and electrical hardness coefficients of the device, respectively, which can be expressed as:

$$k_m = 4E_x \frac{h}{l} \left(\frac{\omega}{l}\right)^3 \quad k_e = \frac{C_s V_{dd}^2}{2d^2}$$

In the above formula, E_x is Young's modulus of the material in the sensitive axis, and h , ω , and l are the length, width, and height respectively. The Brownian equalized noise (BNEA) of the device at temperature T is:

$$BENA = \frac{\sqrt{4K_B T D}}{M} = \sqrt{\frac{4K_B T \omega_0}{MQ}}$$

The current equivalent noise (CNEA) of the device is:

$$CENA = \frac{\delta C d k_s}{2C_0 M} = \frac{\delta C d \omega_0^2}{2C_0}$$

Then the total output noise density (TNEA) of the accelerometer can be obtained as:

$$TNEA = \sqrt{BNEA^2 + CNEA^2}$$

BNEA is also called thermal noise, usually, the high-frequency component of noise and CNEA is mainly the low-frequency component of noise. It can be seen from the above formula that the thermal noise amplitude of the accelerometer device decreases as the mass of the device mass becomes larger, and they are in a negative correlation. Therefore, the noise of MEMS acceleration is usually large due to the limitation of volume. In the production and manufacture of MEMS accelerometers, it is a huge problem to deal with the relationship between noise and volume.

3.2.2 Features of STIM318

Table 3.2.2-1 Features of STIM318

| | |
|---|--|
| Low noise |  |
| Low bias instability | |
| Excellent performance in vibration and shock environments | |
| 6 axes offered in the same package | |
| Electronically calibrated axis alignment | |
| No intrinsic wear-out effects. | |
| High stability accelerometers | |
| Insensitive to magnetic fields | |
| Full EMI compliance | |
| Digital interface, RS422 | |
| Fully configurable | |

(38.6mm x 44.8mm x 21.5mm)[Ⓢ]

The STIM318 is an IMU(Inertial Measurement Unit) with a 3-axis high-precision gyroscope built using MEMS technology, and it also contains a 3-axis accelerometer. Before leaving the factory, the IMU is calibrated for factors such as deviations and temperature effects. The operating temperature range of the IMU is from -40°C to $+85^{\circ}\text{C}$. It can be powered by $+5\text{V}$ DC power supply. [14]

The interface communication protocol of STIM318 is RS422. Various configurations can be adjusted freely. For example, the frequency of the low-pass filter, the output sampling rate, the output unit, and so on. After each power-on, the IMU will perform a self-check, such as serial number approval, report configuration parameters, and so on.

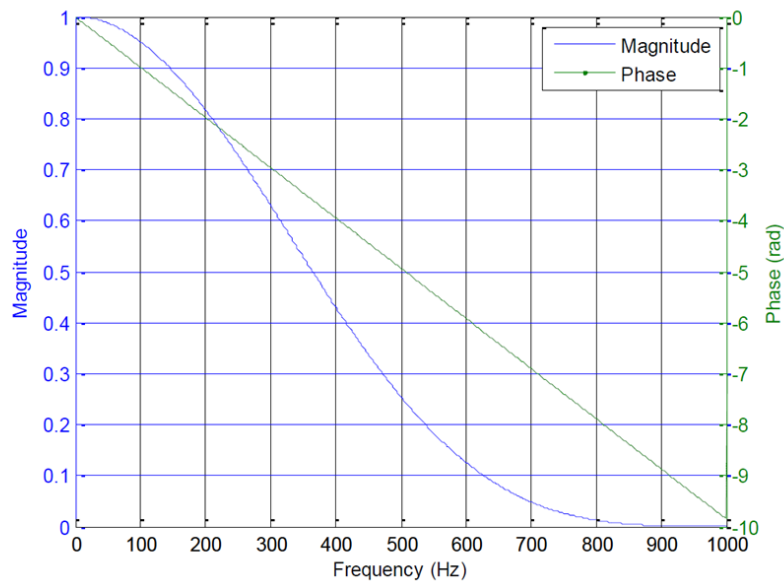


Figure 3.2.2-1 Frequency characteristics of gyros with low-pass filter -3dB frequency set to 262Hz

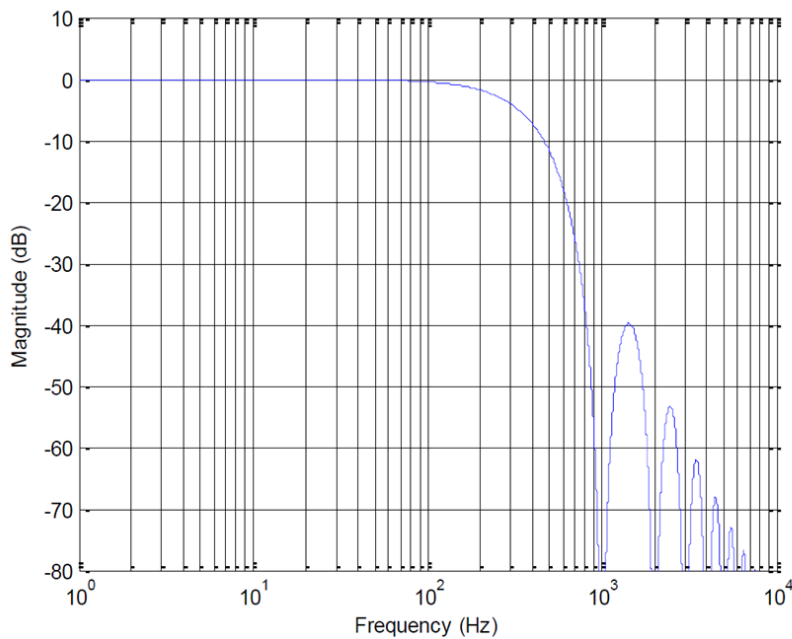


Figure 3.2.2-2 Frequency characteristics of gyros with low-pass filter -3dB frequency set to 262Hz

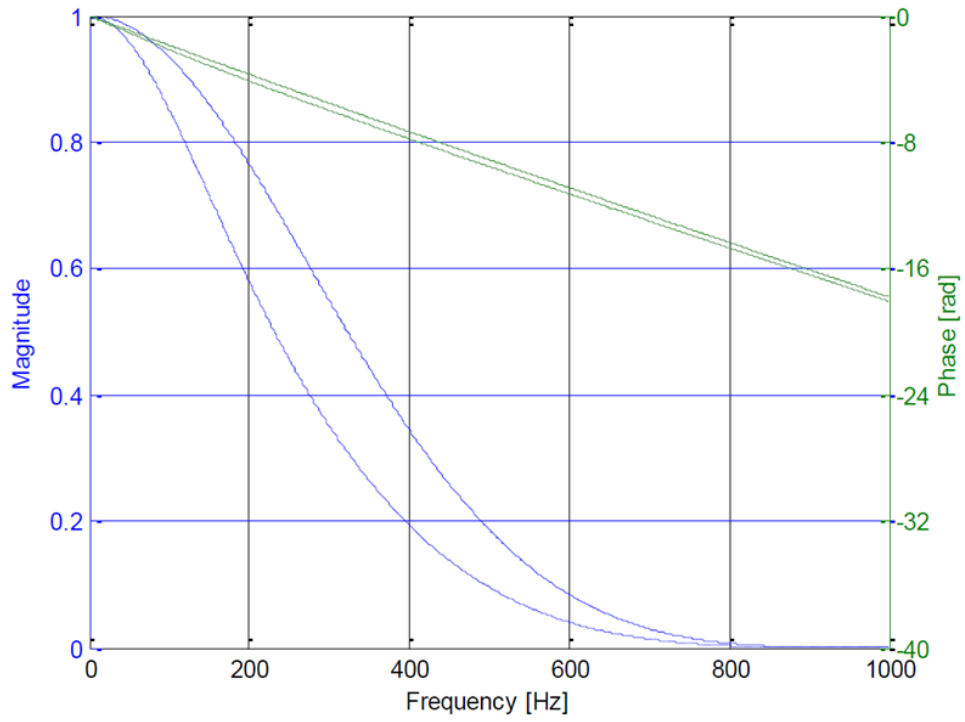


Figure 3.2.2-3 Frequency characteristics of accelerometers with low-pass filter -3dB frequency set to 262Hz

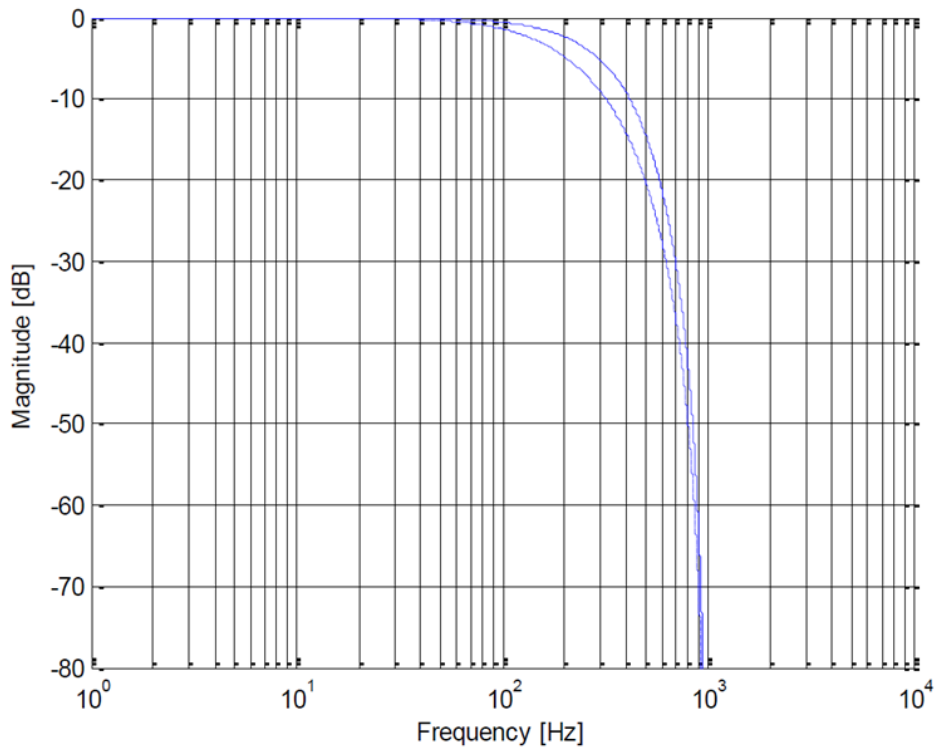


Figure 3.2.2-4 Frequency characteristics of accelerometers with low-pass filter -3dB frequency set to 262Hz

Table 3.2.2-2 Features details

| Parameter | Min | Nom | Max | Unit |
|---------------------------------------|------|--------------------|------|---------|
| GENERAL | | | | |
| Weight | | 55 | | g |
| Operating temperature | -40 | | 85 | °C |
| Supply voltage | 4.5 | 5.0 | 5.5 | V |
| Power consumption | | 1.8 | 2.5 | W |
| Start-up time | | 0.7 | 1 | s |
| Sample rate | | | 2000 | SPS |
| Mechanical shock, any direction | | | 1500 | g |
| RS422 transmission bit rate | | | 5.18 | Mbit/s |
| Misalignment | | 1 | | mrad |
| GYRO | | | | |
| Input range | | ±400 ¹⁾ | | °/s |
| Non-linearity @ ±200 °/s | | 15 | | ppm |
| Resolution | | 0.22 | | °/h |
| Bias instability | | 0.3 | | °/h |
| Angular random walk | | 0.15 | | °/√h |
| Bias error over temperature gradients | | ±10 ²⁾ | | °/h rms |
| Linear acceleration effect | | | | |
| Bias | | 1 ⁴⁾ | | °/h/g |
| Scale factor | | 50 ⁴⁾ | | ppm/g |
| Scale factor accuracy | | ±500 | | ppm |
| ACCELEROMETER | | | | |
| Input range | | ±10 ³⁾ | | g |
| Resolution | | 1.9 | | μg |
| Bias instability | | 0.003 | | mg |
| Velocity random walk | | 0.015 | | m/s/√h |
| Bias 1 year stability | 1.25 | 1.5 ⁵⁾ | | mg |
| Bias error over temperature gradients | | ±0.7 ²⁾ | | mg rms |
| Scale factor accuracy | | ±200 | | ppm |

1) Optional ranges are available

2) Condition: $\Delta T \leq 1^\circ\text{C}/\text{min}$

3) Optional ranges: ±5 g, ±30 g, ±80 g

4) With g-compensation

5) Export controlled version (STIM318e) available with 1.2 mg 1 year bias stability

3.2.3 Development software

The cable of STIM318 has good expansibility and flexibility. In order to facilitate the reading of test data, the data transmission line adopts the conversion chip of Future Technology Devices

International to convert the RS422 interface to USB. Able to handle all USB protocols and signals.

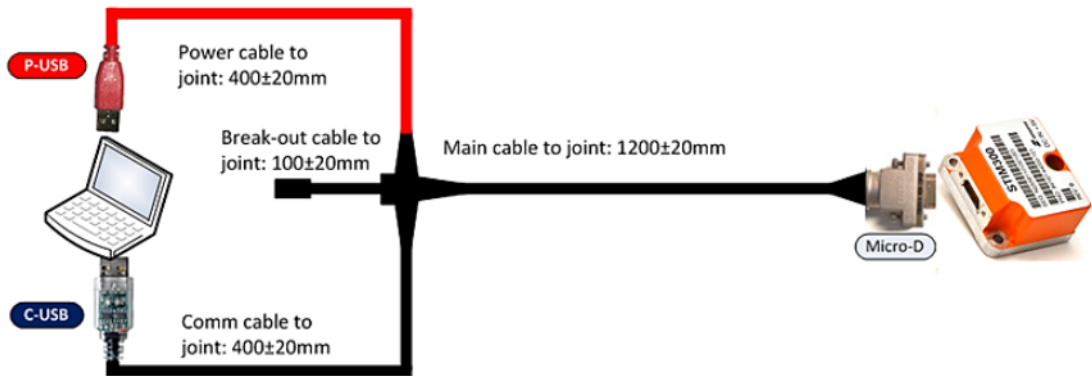


Figure 3.2.3-1 connection of the testing system

The data cable has two USB port cables, one is called C-USB and the other is called P-USB. The P-USB cable is mainly used to power the sensor. The C-USB cable is mainly responsible for data transmission.

Table 3.2.3-1 cables and connector features

|  <p>Development cables of STIM318</p> |  | |
|--|---|---------------------------------------|
| | Feature | Available |
| | Portability across PC-s | Yes (custom SW installation required) |
| | Hardware installation required? | No |
| | Gyro output available | Yes |
| | Accelerometer output | Yes |
| | TOV and External trigger available? | Yes (Break-out-cable) |
| | Transmission rate supported | Up to 3Mbit/s |

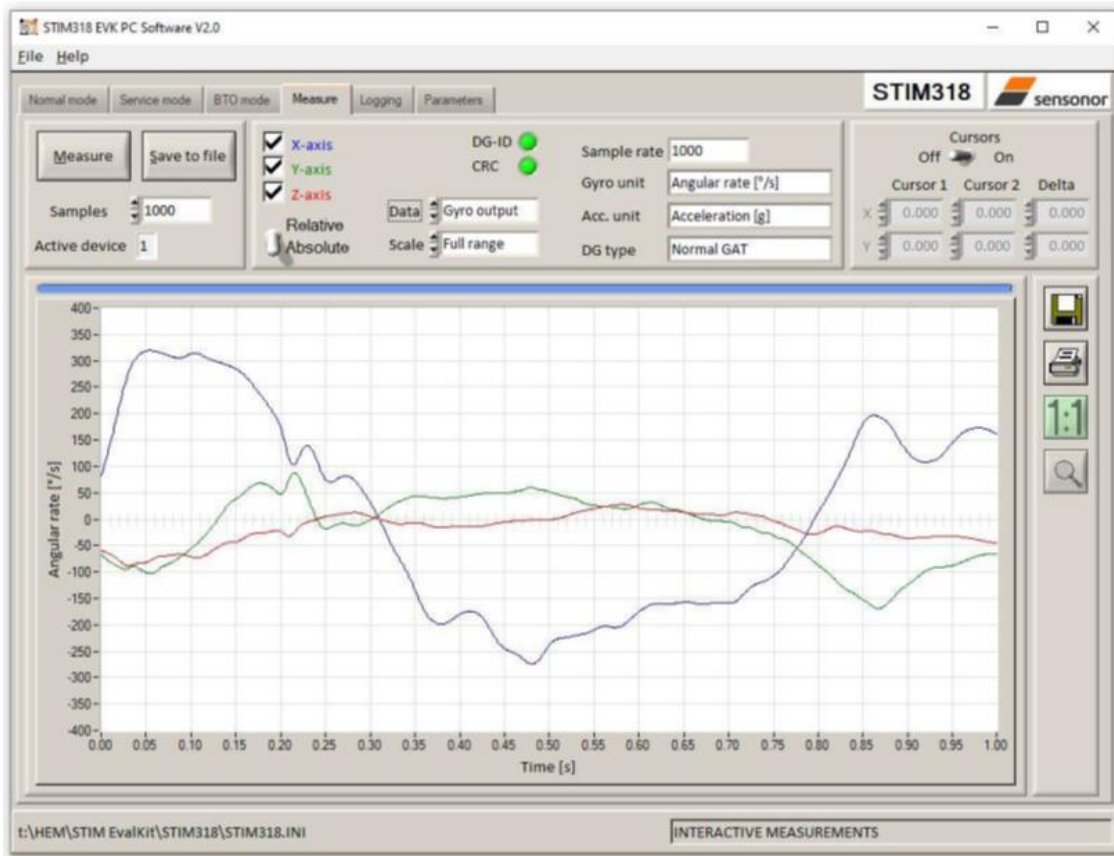


Figure 3.2.3-2 Development software dashboard

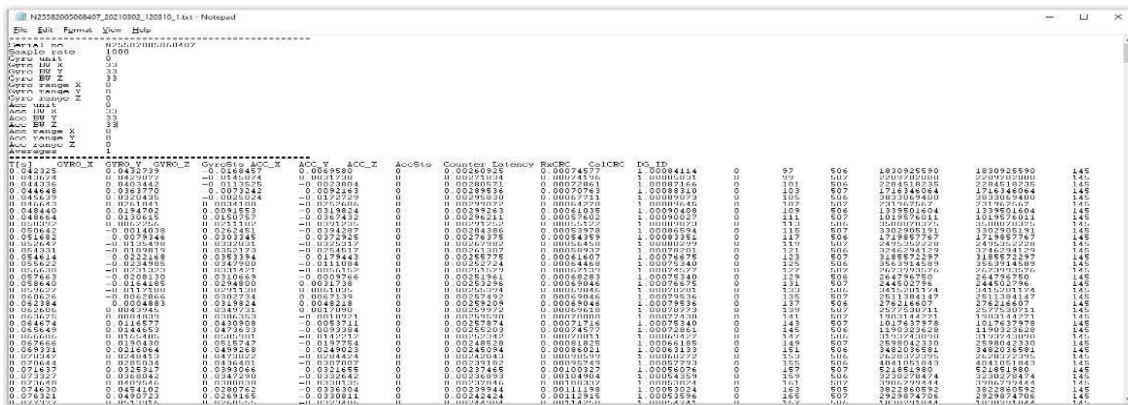


Figure 3.2.3-3 saving data format

As shown in the figure, the software can display the sensor data just collected. The format of the data will be stored in a .txt file. Data can be imported and split through Excel. The data of the gyroscope and accelerometer packaged inside the STIM318 will be recorded at the same time.

3.3 Prototype: The SAIFE Demonstrator

I integrated the sensors into a BOX to make a demonstrator. The demonstrator integrated a fiber optic gyroscope (the FOG), an inertial measurement unit (an IMU, containing an accelerometer

and a gyroscope), and an inclinometer on 3 axes (incorporated in the accelerometer). The box shell and top cover are made of 3D printing engineering technology, and the material is engineering plastics. The base is CNC machined and the material is aluminum. The processor, memory card, and control board are all integrated inside the box, equipped with status indicators and communication interfaces. All components are connected by bolts, screws, and copper pillars. It can be simply understood as a small computer with a sensor inside the box. The following is a picture of the appearance of the demonstrator:

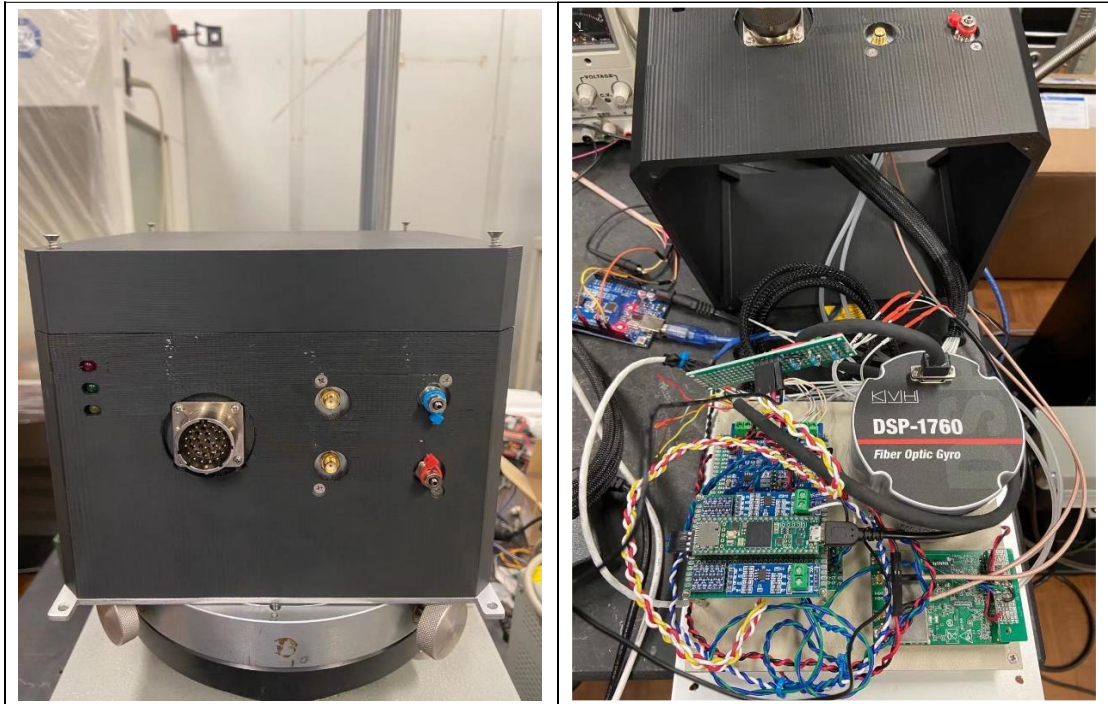


Figure 3.2.3-1 The SAIPE Demonstrator

Since the data is stored directly through the onboard memory card, there is no need to connect the prototype to the PC for communication. Through the given procedure, after the prototype is powered on, the yellow light of the indicator light turns on first, and after a few seconds, the green light of the indicator light turns on. At this time, the various sensors have been prepared and started to automatically record data.

4 Measurement campaign

4.1 Validation workflow

In this calibration experiment, the method I adopted is to use a standard calibration platform to compare the output of theoretical data with the collection of actual data. Look at the final implementation effect.

Because in this experiment, the main equipment I use can be simply divided into 3 dozen parts, the first part is the Arduino UNO control board, the second part is the Oriental's high-precision stepping motor, and the third part is the rotating platform for testing. The fourth part is the fiber optic gyroscope placed on the platform. In this experiment, I need to connect 2 computers, one

computer is connected to the Arduino UNO control board, and the digital signal output is generated by programming the control board. Another computer I used to connect the fiber optic gyroscope and IMU, through the development of software, to collect sensor data.

4.1.1 Signal generation

In this part, I need to generate two outputs, a digital signal that controls the speed of the motor and a signal that controls the direction of the motor's rotation. In Arduino, PIN3 to PIN13 can generate digital signal output. In the first structure construction, I used PIN11 and PIN13 for signal output.

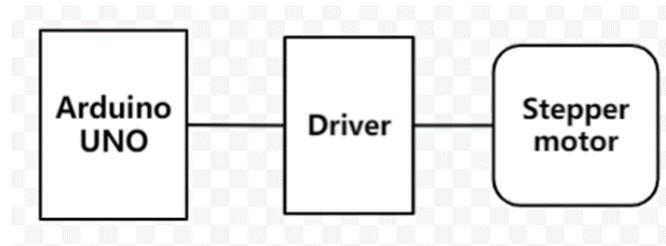


Figure 4.1.1-1 Signal workflow diagram

Considering the stability of the output signal, the first step is to try to generate a pulse signal with a frequency of 100 Hz. Thanks to Arduino's rich function library to choose from, in this experiment, I don't need to change the duty cycle of the pulse signal, just use the 50% duty cycle in the default setting. The tone library of Arduino can generate a square wave signal with a constant duty cycle of 50%. It can be generated at any pin on the Arduino UNO control board. And you can specify the output time of the signal. Examples are as follows:

```

const int Pin = 11;

void setup() {
  pinMode(Pin, OUTPUT);
}

void loop(){
  tone(Pin,100);
}
  
```

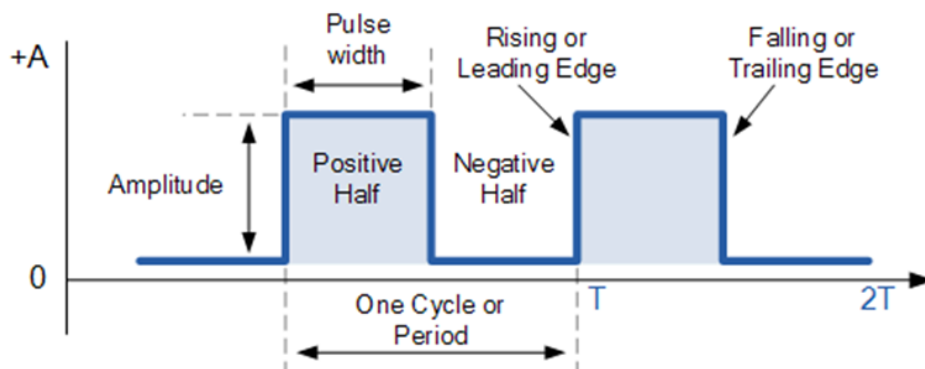


Figure 4.1.1-2 Ideal signal behavior

Connect the oscilloscope to the pin of the Arduino UNO output terminal, you can get the image as follows:

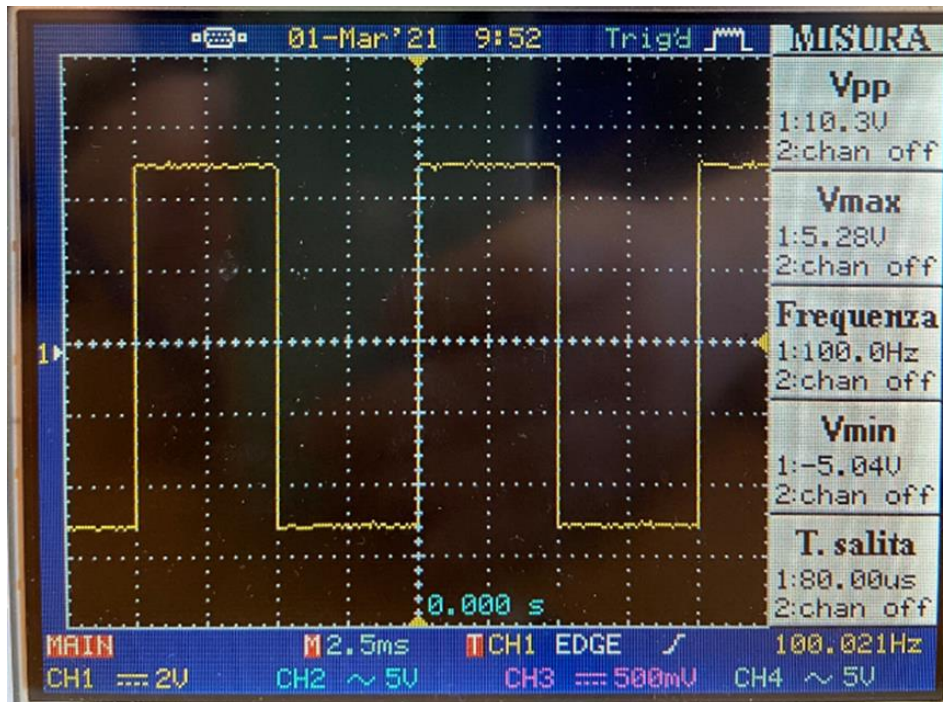


Figure 4.1.1-3 Signal with 100Hz constant

The next step is to add the direction control signal to the program. The purpose is to change the direction of rotation after the motor runs for a period of time. For example: After powering on, the motor will first rotate in a clockwise direction for 10 seconds, and then rotate in a counterclockwise direction. According to the technical manual of the drive control board of the motor, we can know that on the Oriental's high-precision motor, the control signal related to the rotation direction is input by two PIN pins, one is high level, and the other is grounded. Therefore, in order to realize that the motor keeps rotating in one direction first, I set the output high level continuously during the initial test, and then switch to a low level after 10 seconds. In this way, the purpose of realizing the steering of the motor can be achieved. Here are parts of the example code:

```
const int Pin = 11;
const int dirpin = 13;
void setup() {
  pinMode(Pin, OUTPUT);
  pinMode(dirpin,OUTPUT);
}
void loop(){
  digitalWrite(dirpin,HIGH);
  tone (Pin,100) ;
```

```

delay(10000);
digitalWrite(dirpin,LOW);
delay(10000);
}

```

Although the above procedure can realize the direction change of the motor, there is a very big problem at the same time. That is, every time the motor changes direction, the stepper motor will make a lot of noise and vibration. According to Newton's second law of physics, $F = ma$. Speed $v = at$.

Force leads to acceleration, ie, change in velocity. So, the motion is dictated by

$$F = ma = m \frac{dv}{dt}$$

The change in velocity dv in the first moments (which is the question) depends on the infinitesimal time period dt you are considering. This time period can be arbitrarily small, and as the force F is fixed, the change in velocity dv can be arbitrarily small too. So yes, the motion starts 'gradually', which is to say that the stepper motor doesn't have 0 velocities and then 100 °/s without reaching a velocity in between.

Therefore, the vibration and abnormal noise generated by the stepper motor is because at the moment of changing the direction, the value of time t is very very small, so the acceleration becomes infinite. For the motor, at this moment, the torque of the motor rotor is infinite, thus causing abnormal noise and vibration of the motor. In order to solve this problem, I need to consider changing the signal from an instantaneously changing square wave signal to a trapezoidal signal.

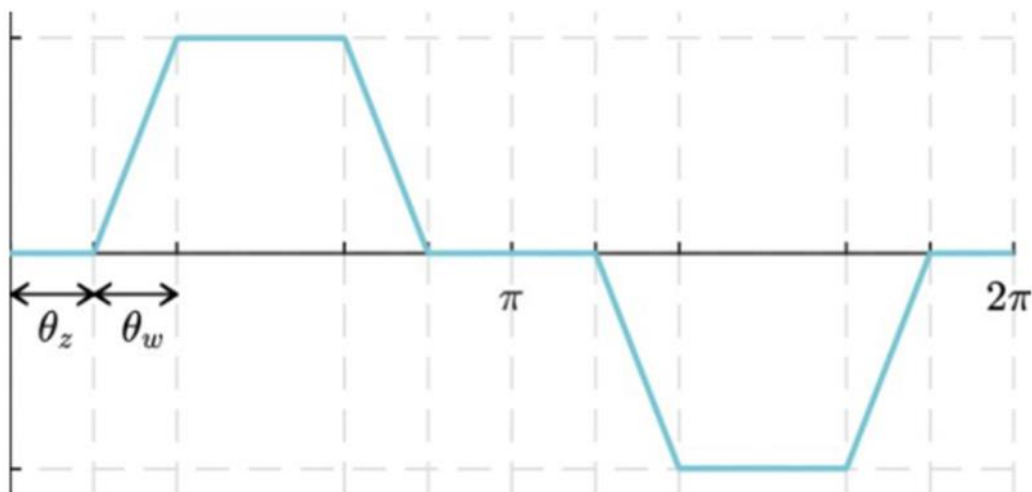


Figure 4.1.1-4 Ideal trapezoidal signal.

The figure above shows the relationship between the speed of the stepper motor and the time. It is assumed that the direction of rotation of the stepper motor is clockwise as the positive direction and counterclockwise as the negative direction. It also rotates at a maximum speed of

100 Hz. When the Arduino UNO is powered on, the frequency linearly increases from 0Hz to 100Hz and keeps it for a period of time. Then reduce to 0Hz. After a period of pause, the stepper motor changes the direction of rotation. At this time, it rotates counterclockwise, and the speed starts to increase linearly. After reaching the maximum speed, it stays for a period of time and then decreases to 0.

However, in the actual state, I found that because Arduino UNO produces a digital signal, not an analog signal. The digital signal is discrete, so in the process of increasing the frequency from 0 to 100Hz, the actual signal frequency and time relationship is a step-like rise.

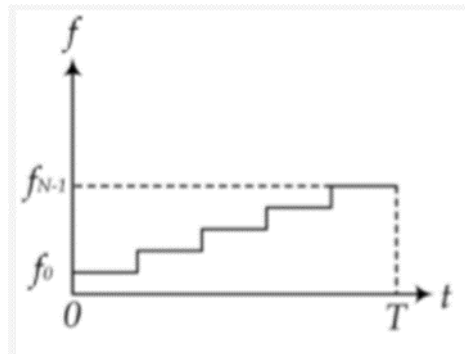


Figure 4.1.1-5 stepper increase signal

When our divisions are large enough, the speed image will be very close to a straight line. Therefore, in the range of 0-100Hz, I will divide it into 100 parts, each time increasing by 1Hz, the duration is 10 milliseconds. code show as below:

```

Void loop{
For(i=0:i<100:i++){
tone(pin,i);
delay(10);
}
}

```

When I compile this code, the IDE shows that the compilation is normal. But when I upload the program to the driver board of the stepper motor. There is a huge problem, in the range of 0-31Hz. Due to the limitation of the tone library, Arduino UNO cannot generate signals with a frequency lower than 31H.

Tones functions are generated by setting up a timer in RTC mode and toggling an output pin (in an Interrupt Service Routine) when the timer reaches a value determined by the contents of its OCR register. With the maximum Prescaler value of 1024, any frequency less than 31 Hz would require a value of greater than 255 in the timer's OCR register. Since Tone uses Timer2 and Timer2 is an eight-bit timer, frequencies less than 31 Hz are not possible.

Method 1, try to use digitalWrite() statement

The digitalWrite() function is used to write HIGH or LOW values to digital pins. If the pin has been configured as OUTPUT via pinMode(), its voltage will be set to the corresponding value: 5V (or 3.3V on a 3.3V board) means HIGH, and 0V (grounded) means LOW. If the pin is configured as INPUT, digitalWrite() will enable (HIGH) or disable (LOW) the internal pull-up

on the input pin. Consider setting `pinMode()` to `INPUT_PULLUP` to enable the internal pull-up resistor. If `PINMode()` is not set to `OUTPUT`, it will not be enabled when `digitalWrite(HIGH)` is called.

```
Void loop() {  
    digitalWrite (pin ,value);  
}
```

But when using `digitalWrite`, it can be found from the oscilloscope that the frequency image will jump suddenly, and the output signal cannot be stable enough. Because the stepper motor is very sensitive, it has a great influence on the speed of the motor.

Method 2: Directly compile PIN by register address.

Using AVR direct port i/o is outside the original parameters set by the OP of using `digitalWrite()`.code above would be faster than digital write, but because of the way the registers work on the AVR it is not atomic which might cause issues if other codes were using that port at ISR levels like saying servo or the infrared library. You could make it atomic by blocking interrupts and restoring them around the statement which adds additional instructions which create additional latency. Parts of code like below:

```
while (1) {  
    currentMicros = micros();  
    elapsedMicros = currentMicros - previousMicros;  
    if (elapsedMicros >= halfPeriod) {  
        PINB = PINB | 0b00001000; // toggle D11  
        previousMicros = previousMicros + halfPeriod;  
    }  
}
```

When compiling the register, the signal output pin that controls the direction of the motor cannot be in the same half area as the output pin that controls the speed signal. Because when writing the register address, the output value of the direction signal will be changed. So I changed the direction signal output from 13 pins to 7 pins.

After reaching the extreme speed, the frequency of the signal is very stable on the oscilloscope, but after measuring with a cymometer, it will be found that the frequency value jumps very obviously and is not stable. The most important thing for us in the experiment is to maintain stability when spinning at extreme speeds.

After judging the final signal stability, I decided to continue to use `Tone(function)` library to generate signals. Facts also proved that after using `Tone(function)`, the signal spectrum has better smoothness. On the other hand, our goal is to stabilize the signal at extreme speeds, so `Tone(function)` cannot produce the first 31Hz defect and will not have a bad influence on the test.

4.1.2 Input signal frequency calibration

To ensure accurate test results, we use a frequency meter to calibrate the output signal frequency of the Arduino UNO. The frequency meter will calculate the collected frequency every 10 seconds and display the result on the screen. The number displayed on the frequency meter is the period of the current signal in milliseconds, and the frequency value of the current signal is obtained by taking the reciprocal. In this test, three frequencies are used, 100Hz, 200Hz, and 300Hz. I performed 4 rounds of testing, sampling each frequency 50 times in each round. Finally, the average value of each frequency was calculated. The results are shown in the following table:

Table 4.1.2-1 Arduino UNO frequency calibration

| test times | 100Hz | 200Hz | 300Hz |
|---------------------------|-------------|-------------|-------------|
| 1st | 100.1791213 | 200.3582948 | 300.5373606 |
| 2nd | 100.179182 | 200.3582542 | 300.5373872 |
| 3rd | 100.1791537 | 200.3582593 | 300.5373845 |
| 4th | 100.1791327 | 200.358264 | 300.5373936 |
| | | | |
| nominal frequency (Hz) | 100.1791474 | 200.3583655 | 300.5373815 |
| nominal angle rate (° /s) | 36.06449307 | 72.12901158 | 108.1934573 |

For the subsequent data analysis, I will use the calibrated signal frequencies, i.e. 100.179Hz, 200.358Hz, and 300.537Hz.

4.1.3 Connect the stepper motor

Installing the driver

During the installation of the drive board, it is necessary to keep it horizontal or vertical. The drive board is directly fixed on the heat dissipation aluminum fin with screws, and the heat dissipation silicon grease is applied between the heat dissipation capacitor and the heat dissipation plate.

Table 4.1.3-1 Screws used in the driver board

| | |
|--|----------|
| Driver model | CRD5114P |
| M3 screws | 4 pieces |
| M3 spring washers | 4 pieces |
| M3 nuts (Not necessary if screw holes are provided in the enclosure.) | 4 pieces |
| Spacers [5mm or more] | 4 pieces |
| Note: Torque the mounting screw to $0.5 N \cdot m$ | |

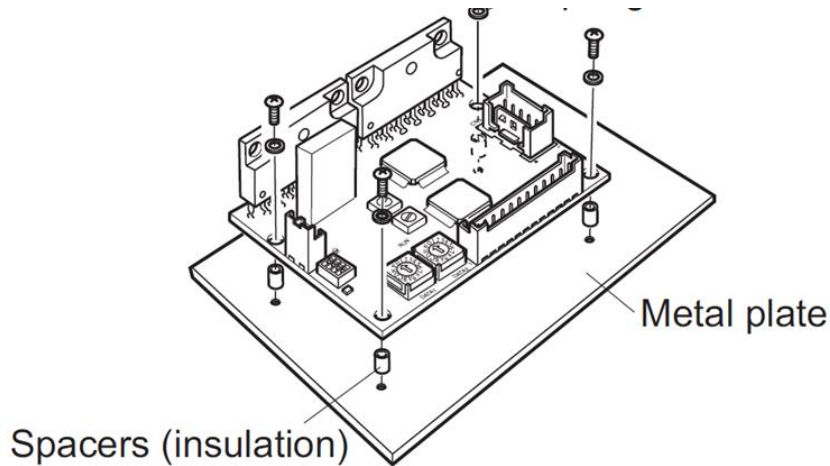


Figure 4.1.3-1 Driver board

It should be noted that, because in the process of running the stepper motor, the various electronic devices on the drive plate will also generate heat, so do not put the drive plate near other equipment with a lot of heat. Make sure the ventilation around the equipment is good and the ambient temperature is below 40 degrees Celsius. The case of the MOSFET Array on the drive plate is insulated, and they are the electronic components that generate the most heat during the operation of the stepper motor. To ensure the good performance of the drive plate, I apply cooling silicone grease on the back of the MOSFET Array and then fix the MOSFET Array on the cooling aluminum fin with screws. Silicone grease is an ideal choice because of its low cost and good thermal conductivity. During the operation of the stepper motor, the maximum surface temperature of the MOSFET array shall not exceed 90 ° C, otherwise, the experiment must be stopped and the operating conditions checked.

Connecting a power filter at the input end of a 24V DC Power Supply can effectively prevent the noise generated in the drive plate from entering the power line and prevent the noise from spreading outward through the power line. Use a larger cable to connect the drive plate and the power filter. Both the drive plate and the power filter must be grounded. The cable at the ground end must be grounded to the shortest possible distance. This has the advantage of avoiding potential differences at the ground position as much as possible. The joints shall have a large contact area, a conductive surface, a thick and uniform material. Connect the stepper motor, drive board, and Arduino Uno control board to the connection point to avoid potential differences between the ground parts. If relays or electromagnetic switches are needed, power filters and RC circuits can be used to suppress the surge generated by these devices. Separate the power supply line of each device from the signal cable for communication function at a distance of about 100 mm to 200 mm.

motor and driver installation and wiring

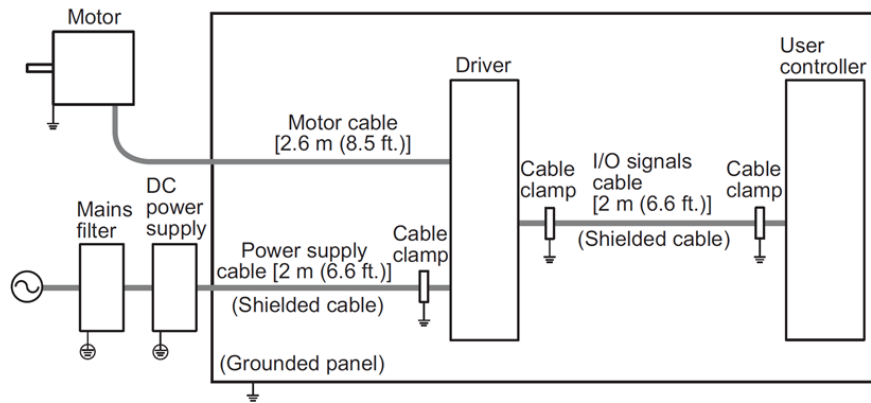


Figure 4.1.3-2 layouts of stepper motor

Because the step Angle adjusting knob of the stepping motor is installed on the control board, it is necessary to adjust the step Angle when the power is on. Insulated screwdrivers must be used to prevent static electricity generation that could damage or malfunction the drive plate.

Connector pin assignments for driver

| Connector No. | Pin No. | Type | Signal | Description | |
|---------------|---------|--------|------------|-------------|--------------------------------------|
| CN1 | 1 | Input | POWER | + | +24 VDC |
| | 2 | Input | | - | GND |
| CN2 | 1 | Input | PLS (CW) | + | Pulse input (CW pulse) |
| | 2 | Input | | - | |
| | 3 | Input | DIR. (CCW) | + | Rotation direction input (CCW pulse) |
| | 4 | Input | | - | |
| | 5 | Input | A.W.OFF | + | All windings off input |
| | 6 | Input | | - | |
| | 7 | Input | C/S | + | Step angle select input |
| | 8 | Input | | - | |
| | 9 | Input | C.D.INH | + | Current cutback release input |
| | 10 | Input | | - | |
| | 11 | Output | TIMING | + | Excitation timing output |
| | 12 | Output | | - | |
| CN3 | 1 | Output | MOTOR | | Blue motor lead |
| | 2 | Output | | | Red motor lead |
| | 3 | Output | | | Orange motor lead |
| | 4 | Output | | | Green motor lead |
| | 5 | Output | | | Black motor lead |

Connector pin assignments for connector-type motor

| Terminal No. | 1 | 2 | 3 | 4 | 5 |
|-------------------|------|-----|--------|-------|-------|
| Motor-leads color | Blue | Red | Orange | Green | Black |

Figure 4.1.3-3 motor connection pin

When the cable connecting the stepper motor needs to be disconnected, the force pulling the connector must be parallel to the direction of the output shaft of the stepper motor. The connector of this stepping motor has a locking mechanism, so it is necessary to release the locking mechanism before unloading the connector. In order to prevent damage to the stepping motor and connector, it is forbidden to pull out the cable by force. The operation process is shown in the figure below:

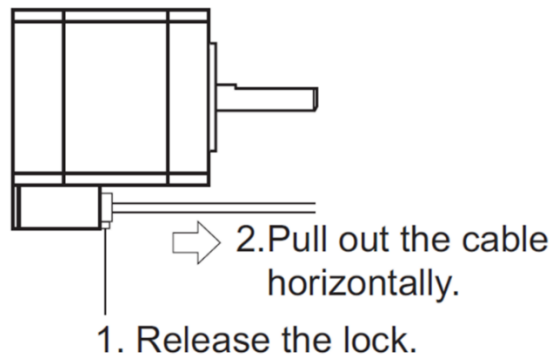


Figure 4.1.3-4 motor unlock

When connecting cables, pay attention to the polarity of the power supply. It is likely to damage the drive plate if the polarity is reversed. To prevent failure or damage due to weak connectors, the connectors must be securely inserted to protect the stepper motor or drive plate. Use a screwdriver to pull out the connector to better protect the plastic parts and locking mechanism of the connector.

Table 4.1.3-2 Motor performance

| | |
|-------------------------------|-----------------|
| Driver model | CRD5144P |
| Power supply input voltage | 24VDC \pm 10% |
| Power supply current capacity | 2.5 A or more |

step angle switching

The stepper motor has two step angle setting switches, called DATA1 and DATA2.

Data 1 switch is used by default in factory Settings. With each of the two switches, step angles can be preset in 16 steps and the desired setting can be selected through C/S (step angle switching) input. With each of the two switches, step angles can be preset in 16 steps. To change the step angle, change the DATA1 or DATA2 dial setting using a precision screwdriver. Step

angles 1 and 2 can be set to any one of 16 settings from [0] through [F], respectively. The step angles corresponding to the respective graduations are shown below.

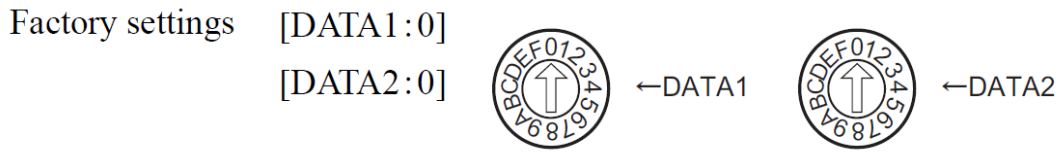


Figure 4.1.3-5 step angle switch

Table 4.1.3-3 step angle resolution table

| R1 | | | | R2 | | | |
|----------------|--------------------------------|-----------------|------------------|----------------|--------------------------------|-----------------|------------------|
| DATA1 DATA2 | Number of divisions 1 | Resolution 1 | Step angle 1 (°) | DATA1 DATA2 | Number of divisions 2 | Resolution 2 | Step angle 2 (°) |
| 0 | 1 | 500 | 0.36 | 0 | ×2.5 | 200 | 0.9 |
| 1 | 2 | 1000 | 0.18 | 1 | ×1.25 | 400 | 0.45 |
| 2 | 2.5 | 1250 | 0.144 | 2 | 1.6 | 800 | 0.225 |
| 3 | 4 | 2000 | 0.09 | 3 | 2 | 1000 | 0.18 |
| 4 | 5 | 2500 | 0.072 | 4 | 3.2 | 1600 | 0.1125 |
| 5 | 8 | 4000 | 0.045 | 5 | 4 | 2000 | 0.09 |
| 6 | 10 | 5000 | 0.036 | 6 | 6.4 | 3200 | 0.05625 |
| 7 | 20 | 10000 | 0.018 | 7 | 10 | 5000 | 0.036 |
| 8 | 25 | 12500 | 0.0144 | 8 | 12.8 | 6400 | 0.028125 |
| 9 | 40 | 20000 | 0.009 | 9 | 20 | 10000 | 0.018 |
| A | 50 | 25000 | 0.0072 | A | 25.6 | 12800 | 0.0140625 |
| B | 80 | 40000 | 0.0045 | B | 40 | 20000 | 0.009 |
| C | 100 | 50000 | 0.0036 | C | 50 | 25000 | 0.0072 |
| D | 125 | 62500 | 0.00288 | D | 51.2 | 25600 | 0.00703125 |
| E | 200 | 100,000 | 0.0018 | E | 100 | 50000 | 0.0036 |
| F | 250 | 125,000 | 0.00144 | F | 102.4 | 51200 | 0.003515625 |

In this test, I only need 2 gears, the '0' position and the '6' position in the knob "DATA 1". That is, the part filled with yellow in table 3.2.1.2-3. Do not switch the signal input or the step angle setting switch while the motor is operating, or the motor may misstep and stall.

Table 4.1.3-4 workflows of motor

| |
|--|
| 1. Connect a DC ammeter between the motor and the driver. |
| 2. Turn the C.D.INH (current cutback release) input to "ON." Do not apply other input signals. |
| 3. Turn on the driver's power supply (24 VDC). |

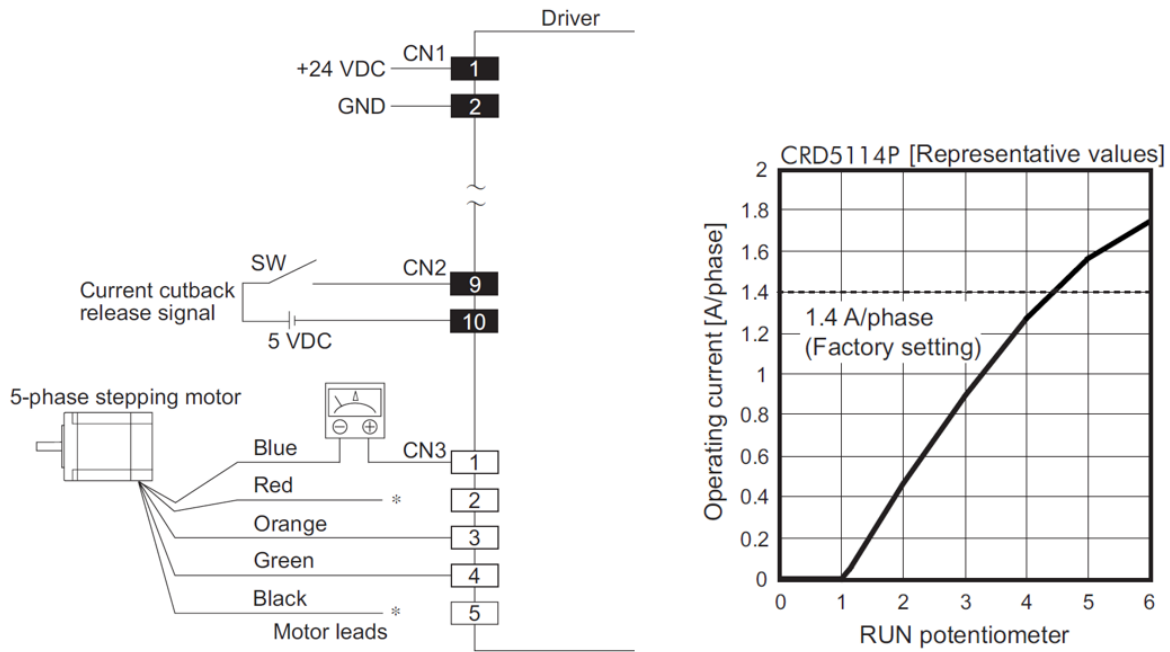


Figure 4.1.3-6 cables connection and operation current graph

On the driver board, use a screwdriver to adjust the RUN knob to change the operating current. Do not adjust the working current during the operation of the stepper motor, it must be cut off first. To prevent personal injury or damage to the motor.



Figure 4.1.3-7 Physical display

4.1.4 Platform horizon adjustment

Adjust the base of the detection device through the knob to make the magnet of the base firmly adhere to the platform. The coarse adjustment bolt moves the digital indicator probe 1 mm

above the round table and then fine-tunes the screw to make the probe press down on the round table plane. At this time, the pointer on the digital indicator begins to change, and a certain value after one turn of the pointer is selected as the reference. Then start to turn the round table manually. Ideally, if the whole round table is at a horizon level, the value of the digital indicator will not change. In actual use, I judge the overall horizon level according to the magnitude of the pointer offset from the reference value.



Figure 4.1.4-1 roundness platform horizon calibration

4.2 Methodology in the data processing

Regression analysis is a statistical analysis method based on the correlation analysis between phenomena and the quantitative calculation of the variation trend of the independent variable X and the dependent variable Y by fitting the mathematical model. Regression analysis should be carried out on the premise of correlation between phenomena, and then the regression equation suitable for fitting the changes of independent variable X and dependent variable Y is determined to determine its quantitative relationship. The significance test of the fitting regression equation is carried out, and finally, the obtained relationship is used to calculate and predict. [15]

The relationship between regression analysis and correlation analysis is very close. There are both connections and differences between the two. The connection lies in that both are the analysis of the quantitative dependence of objective things, and the regression analysis is carried out on the basis of the correlation analysis. If there is no qualitative explanation of whether there is a correlation between the phenomena, and there is no quantitative explanation of the degree of the correlation, it is not suitable to carry out regression analysis, even if the regression analysis is carried out, it will not have any practical significance. Regression analysis can not only understand the relationship between things, but more importantly, it can use this relationship to calculate and predict the future development trend, so it can be seen that regression analysis is the continuation and expansion of correlation analysis. By fitting the regression equation to the correlation between the phenomena through regression analysis, it is possible to calculate and predict, and correlation analysis can play a better role. If there is only correlation analysis without regression analysis, the function of statistical analysis will be lost just like a head without a tail.

The difference between regression analysis and correlation analysis is that they have different concepts and functions, and they illustrate the interdependence between phenomena from different perspectives. Correlation analysis can only explain whether the phenomena are

correlated and the direction and degree of correlation, but it cannot explain how much the other phenomenon will change when one phenomenon changes in a certain amount. Regression analysis can measure the amount of such change by establishing the appropriate regression equation, which is an important basis for calculation and prediction.

The univariate linear regression model is a mathematical equation that analyzes the relationship between two variables. Its general expression is

$$\hat{y} = ax + b$$

where \hat{y} represents the estimated value of the dependent variable y , x represents the independent variable, and a, b are called the undetermined parameters of the regression model, where b is also called the regression coefficient.

The above regression equation is expressed as a straight line in the plane coordinate system, that is, the regression line.

When $b > 0$, y increases with the increase of x , and the relationship between the two variables is positive.

when $b < 0$, y decreases with the increase of x , and the relationship between the two variables are negative.

when $b = 0$, y is a constant and does not change with the change of x . This provides us with a standard for judging the relationship between phenomena and analyzing whether they are in a normal state.

The establishment of a univariate linear regression model can generally be divided into four steps.

- ① Analysis of the relationship between variables, usually based on theoretical qualitative analysis, using a correlation table or correlation diagram to observe, and then calculating the correlation coefficient.
- ② By testing the correlation coefficient Significance, to judge the objective and true status of the correlation coefficient;
- ③ Determine the independent variable and dependent variable according to the research purpose.
- ④ Estimate the model parameters based on the survey data to establish a regression model.

(1) Significance test

① Correlation coefficient

The correlation coefficient is a statistical analysis index that illustrates the closeness of the correlation between two phenomena under the condition of linear correlation. The correlation coefficient is usually r or r^2 ,

$$r^2 = \frac{SSR}{SST} = 1 - \frac{SSE}{SST}$$

Where

$$SSR = \Sigma(\bar{y}_i - \hat{y}_i)^2$$

$$SSE = \Sigma(y_i - \hat{y}_i)^2$$

$$SST = \Sigma(y_i - \bar{y})^2$$

And

$$SST = SSR + SSE$$

r represents the linear correlation direction and degree of correlation between variables x and y , and the value range is $-1 \leq r \leq 1$.

When $-1 < r < 0$, the distribution of the correlation graph shows a trend that y decreases with the increase of x , which is a negative correlation.

When $r = 0$, the distribution of the correlation graph shows an irregular state, and the variable y is not affected by x . It shows that there is no linear correlation between x and y , but other relations cannot be arbitrarily excluded, such as a curve-phase relationship.

When $0 < r < 1$, the correlation distribution shows a trend that y increases with the increase of x , which is a positive correlation.

When $|r| = 1$, the relevant scatter points present a straight line, that is, y and x are completely linearly related. $r = 1$, showing a complete positive correlation; $r = -1$, showing a complete negative correlation.

In order to judge the degree of correlation between phenomena, the standard for judging the degree of correlation through the correlation coefficient is $r = 0$, indicating that x and y are completely uncorrelated; when $0 < |r| < 0.3$, x and y are considered uncorrelated; When $0.3 < |r| \leq 0.5$, x and y are considered to be lowly related; when $0.5 < |r| \leq 0.8$, x and y are considered to be significantly related; when $0.8 < |r| \leq 1$, x and y are considered to be highly related

② Significance test

The significance test can be based on the correlation coefficient, the degree of freedom ($n - m$, where n is the sample size and m is the number of parameters to be determined in the regression model), and the given significance level α value (in socioeconomic phenomena, given The significance level of α is generally 0.05), and the critical value $r_{\alpha(n-m)}$ is found from the correlation coefficient test table, and based on this, it is judged whether the linear relationship is established. If $|r| \geq r_{\alpha(n-m)}$, it indicates that the linear relationship between variables is significant under the condition of significant level α , so the linear regression model to be established is very meaningful; if $|r| < r_{\alpha(n-m)}$, it indicates that it is not appropriate To establish a linear regression model, which needs to be further analyzed and then processed.

(2) Test of regression model

After the regression equation is established, the model needs to be tested to test the representativeness of the regression model. Use the t-test method. If the correlation between the two variables is highly correlated, the equation is highly representative, and this linear

correlation cannot be explained. Whether the relationship is reliable, in order to demonstrate the reliability of this correlation, the correlation coefficient must be tested by t. The formula is:

$$t = \frac{r\sqrt{n-2}}{\sqrt{1-r^2}}$$

r and b have the same sign, and the statistic t obeys $t(n-2)$ distribution. Calculate the t value according to a set of sample sizes, and then check the t distribution table according to the given significance level α and the degree of freedom $n-2$, and find the corresponding critical value $t_{\alpha/2}$. If $|t| \geq t_{\alpha/2}$. This shows that t is statistically significant, that is, there is a linear relationship between the two variables in the population, and this relationship is reliable, otherwise it is considered that there is no linear relationship between the two variables.

4.3 Data analysis with Excel

In order to achieve convenient and fast data processing and visualization, all our data in this test is saved in .csv format. You can use Excel to open the file in this format and analyze it. A complete data analysis needs to go through several steps:

Table 4.1.4-1 Steps of data analysis

| | |
|------------------------|---|
| data acquisition | the original data |
| clear analysis purpose | what information you want to get with this data and what problems to solve |
| observation data | each data field Meaning, Symbols, and English interpretation |
| data cleaning | invalid value, missing value, repeated value processing, whether the data structure is consistent, etc. |
| analysis process | analysis around the purpose; making visualization-making charts and visual reports. |

At the same time, Excel provides a wealth of function tools that can be used according to needs, such as judgment statements, average values, and so on.

5 Results

5.1 Analysis data

5.1.1 Fiber optic gyroscope

5.1.1.1 Fiber optic gyroscope angle rate

On the Z-axis,

The first axis I test is Z-axis. In this round of testing, because the test platform is a rotating round table. At the same time, according to the FOG datasheet, I know that the vertical direction of the product is the Z-axis. The round table has been adjusted to a horizontal state, so it is a good choice to give priority to testing the Z-axis gyroscope data without additional equipment.



Figure 5.1.1-1 FOG test on Z-axis

The first test is 100Hz signal, 200Hz,300Hz. And 100Hz divided into 10. This means that the rotary speed of the table is reduced by a factor of 10. According to the previous frequency calibration, at 100 Hz, 200 Hz. In the 300 Hz frequency range, I obtain frequencies of 100.179 Hz, 200.2358 Hz, 300.3568 Hz.

The data results produced during the first trial run are shown below.

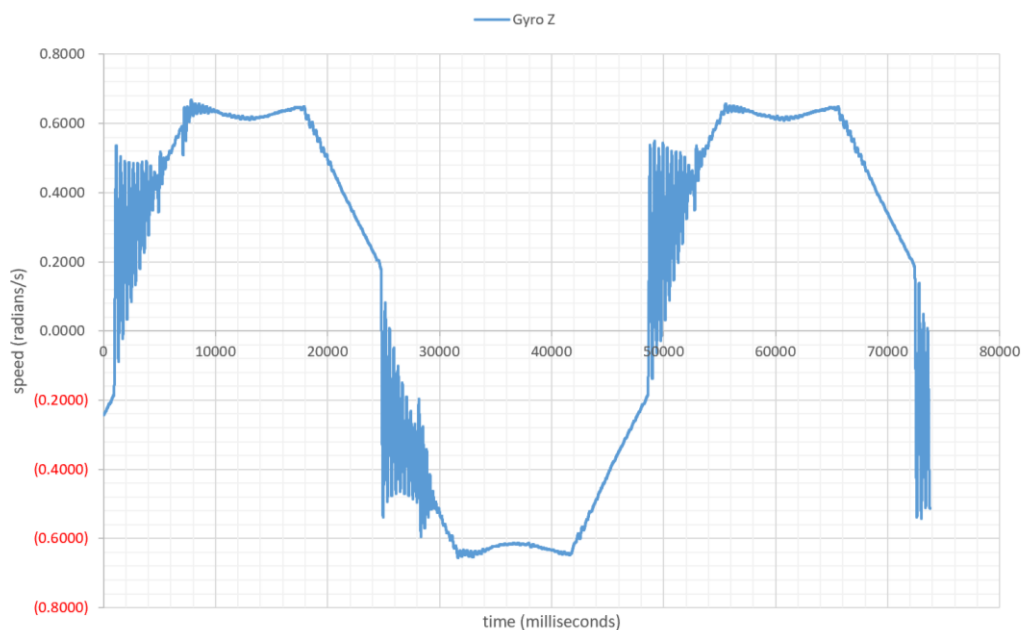


Figure 5.1.1-2 Z-axis test run

In the red circle marks, I can find every peak and trough of the image, and the velocity value of the Z-axis is not constant. According to the calculation, the theoretical velocity at this signal

frequency is 0.63radians/s. Then the time required for each rotation of the circular table is $T = 360^\circ/36^\circ = 10s$

According to the image shown on the Z-axis, I find that the duration of the peak phase is greater than or equal to 10s. Therefore, the speed image generated by the Z-axis is formed after one complete cycle of rotation.

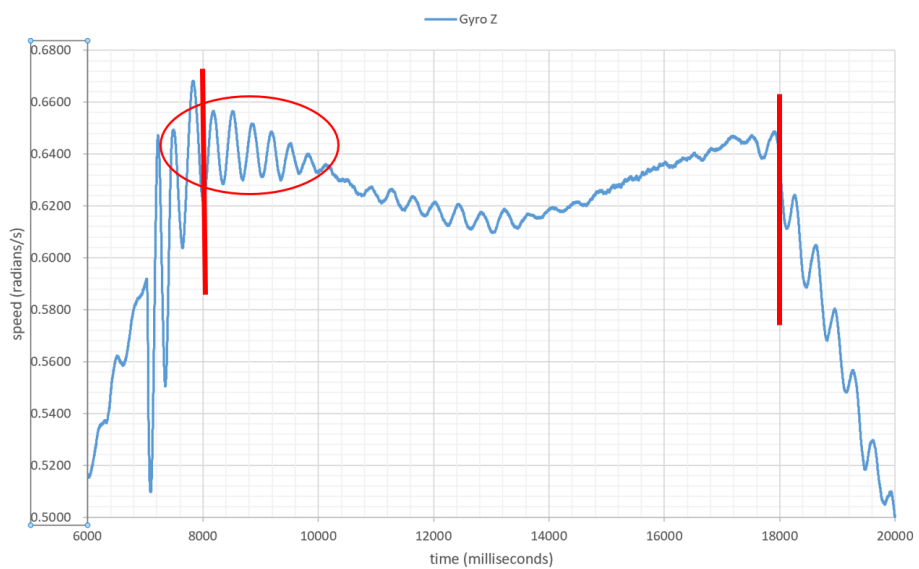


Figure 5.1.1-3 Half period of rotation

Assuming that the fixed speed of the Z-axis ends at 180,000 milliseconds, and the time for the round table to rotate one round is 10,000 milliseconds, I can get the starting point at 8,000 milliseconds from the figure.

But in the interval of 8000-10000 milliseconds, compared to the interval of 16000-18000 milliseconds. The speed value of the former fluctuates greatly. Therefore, it is not suitable for value calculation.

So now I carry out the second test and increase the fixed frequency duration of the signal to 30 seconds. This means that the round table will run at a fixed speed for 30 seconds. According to the results of the previous test, the round table is theoretically fixed at 30 seconds. It will rotate 3 times at speed.

As shown in the figure, I now have the data for 3 complete cycles of the round table rotation. It is known that a round of the round table is 10 seconds, so I only need to intercept the 20-second interval in this 30-second period. For example, in this interval, I choose the interval of 10000-30000 milliseconds. In excel I use average formula” =AVERAGE(D10000:D30000)” , the value =-0.6296 radians/s. And also the “AVERAGE(D5000:D7000)”, the value = +0.6297 radians/s.

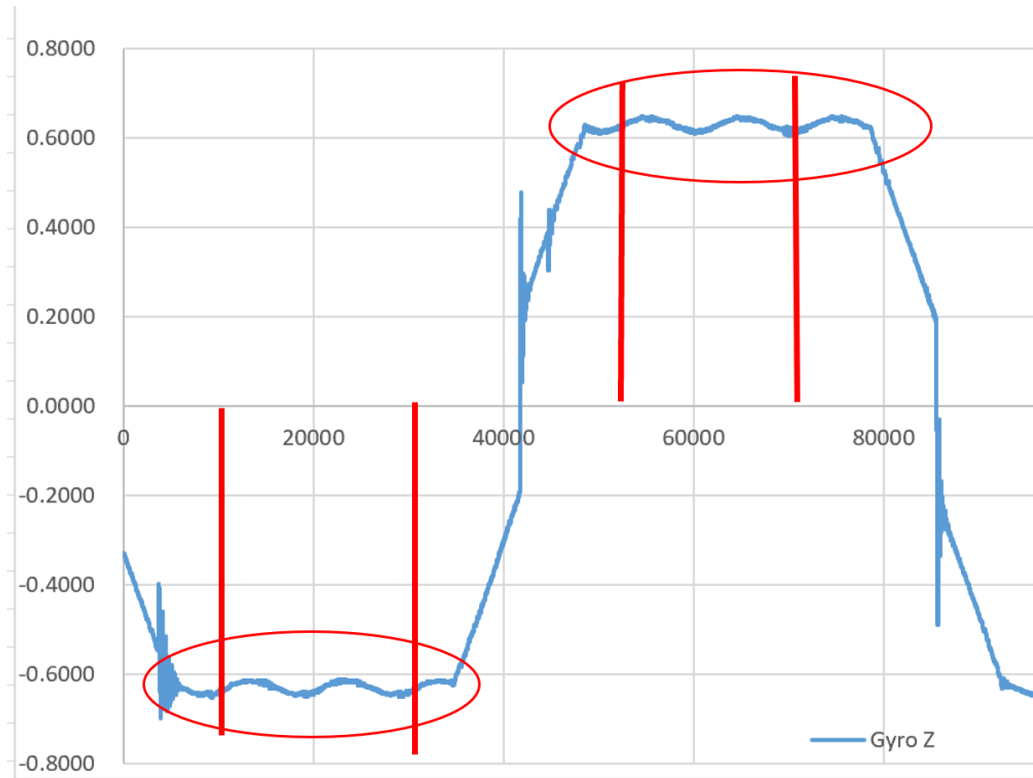


Figure 5.1.1-4 GYRO Z-axis period collection

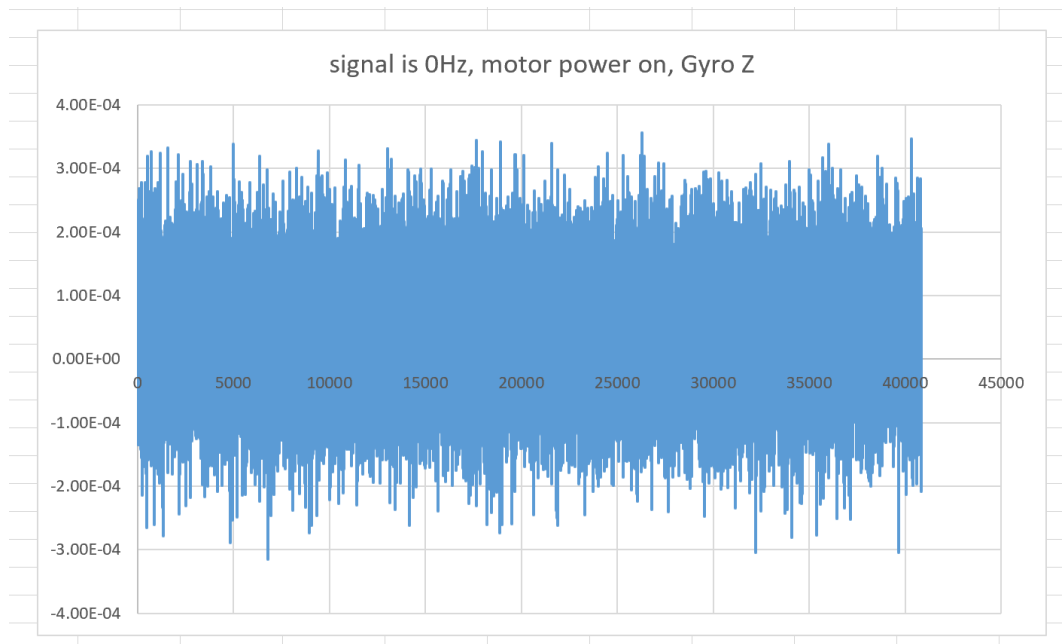


Figure 5.1.1-5 GYRO Z-axis with 0Hz

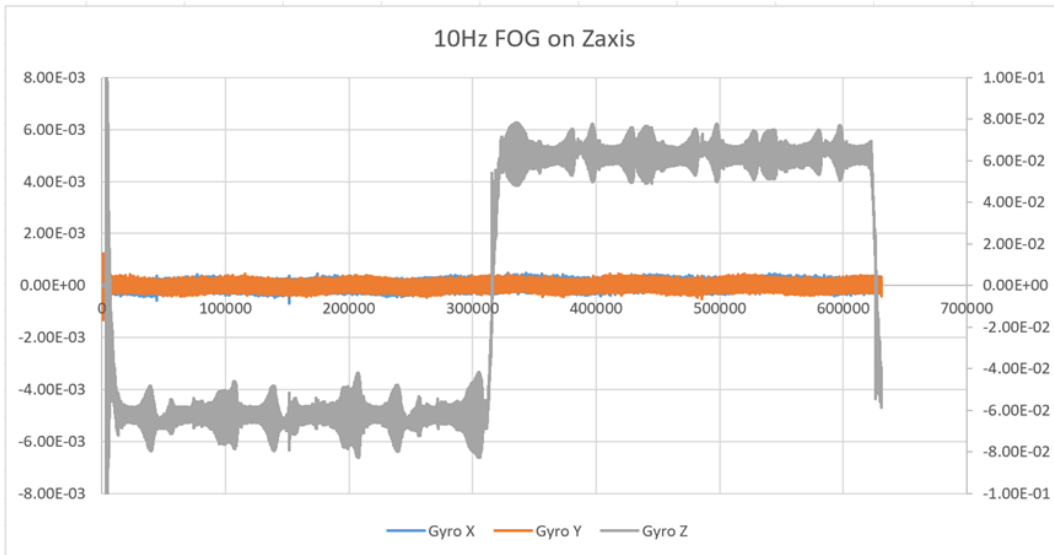


Figure 5.1.1-6 GYRO Z-axis with 10Hz

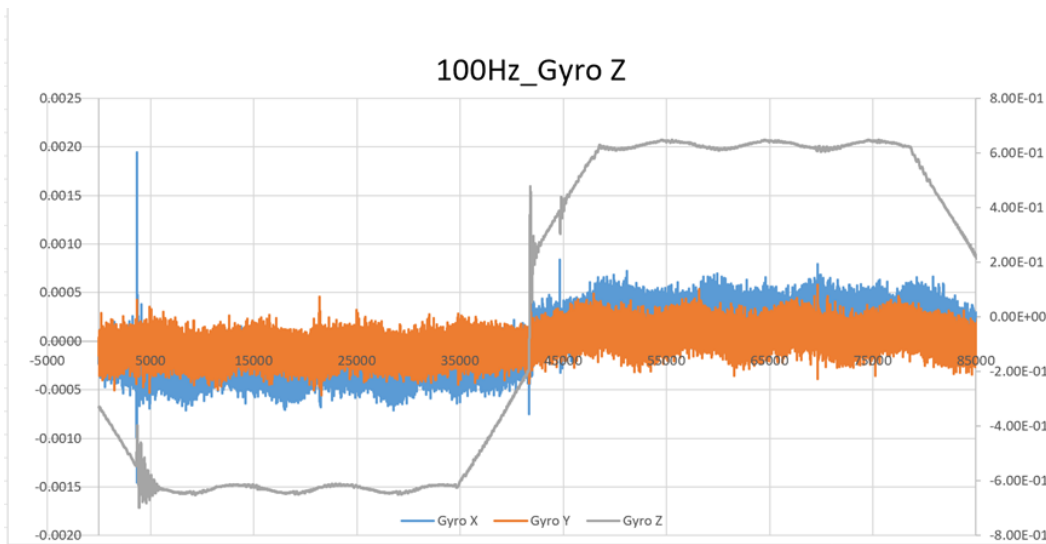


Figure 5.1.1-7 GYRO Z-axis with 100Hz

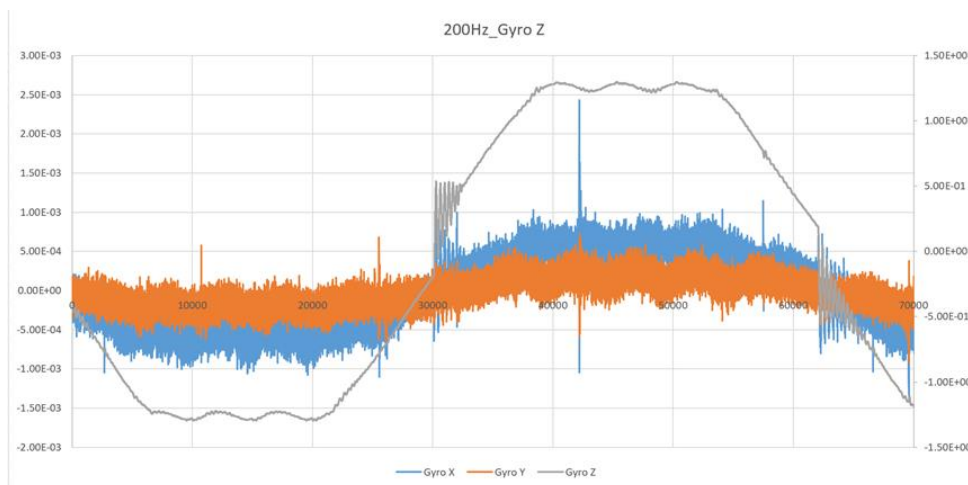


Figure 5.1.1-8 GYRO Z-axis with 200Hz

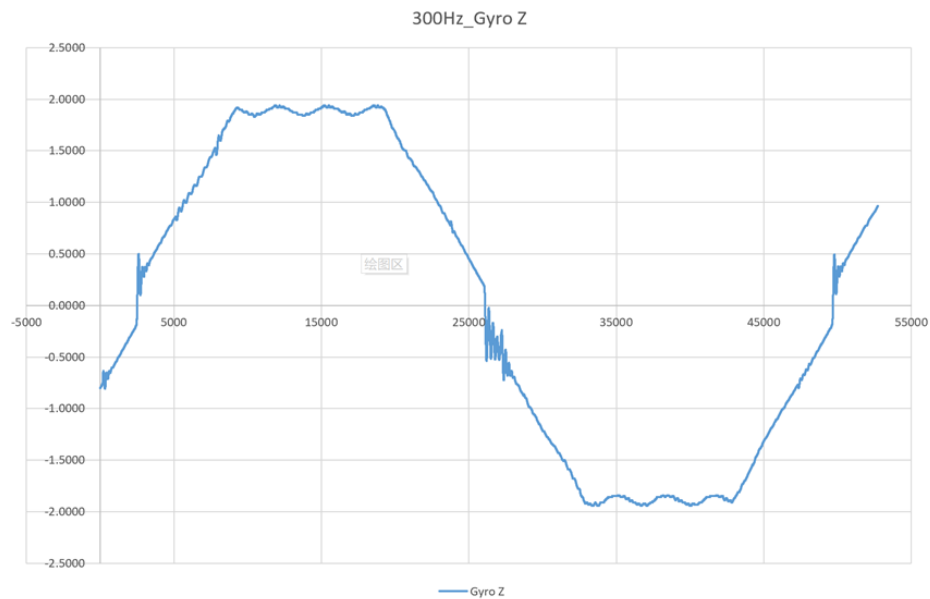


Figure 5.1.1-9 GYRO Z-axis with 300Hz

At signal frequencies of 100 Hz, 200 Hz, and 300 Hz, the waveform is similar to the sine curve when the signal frequency is continuously output. When the step angle of the motor is adjusted to 0.036° , the jitter caused by the digital signal input of the working current will be more obvious. Therefore, the waveform jitters at a fixed point during each rotation period.

Table 5.1.1-1 GYRO Zaxis data

| FOG rotation speed test data on Zaxis | | | | |
|---------------------------------------|------------------------------|--------------|-------------|--------------|
| Nomianl speed($^\circ/s$) | Measured spped($^\circ/s$) | | | |
| Nomianl speed($^\circ/s$) | X | Y | Z | ERRORS |
| -108.193 | -0.045300703 | -0.017029128 | -108.221318 | 0.000189856 |
| -72.129 | -0.031719981 | -0.011218405 | -72.1488298 | -0.001744449 |
| -36.064 | -0.016162552 | -0.005842744 | -36.0707071 | 0.000955432 |
| -3.606 | -0.001567392 | -0.001008781 | -3.60176331 | 0.002518828 |
| 0 | 0.000294996 | -0.000432483 | 0.002550898 | -0.0002091 |
| 3.606 | 0.001687013 | 0.000144246 | 3.607168076 | -0.00263406 |
| 36.064 | 0.01656851 | 0.004728986 | 36.07661304 | -0.00056946 |
| 72.129 | 0.031892581 | 0.009914365 | 72.13180482 | 0.009199543 |
| 108.193 | 0.045541516 | 0.015721206 | 108.2213179 | -0.00570986 |

Table 5.1.1-2 Regression on GYRO Zaxis

| Regression Statistics of Zaxis | |
|--------------------------------|----------|
| Multiple R | 1.000000 |
| R Square | 1.000000 |
| Adjusted R Square | 1.000000 |
| Standard Error | 0.004380 |

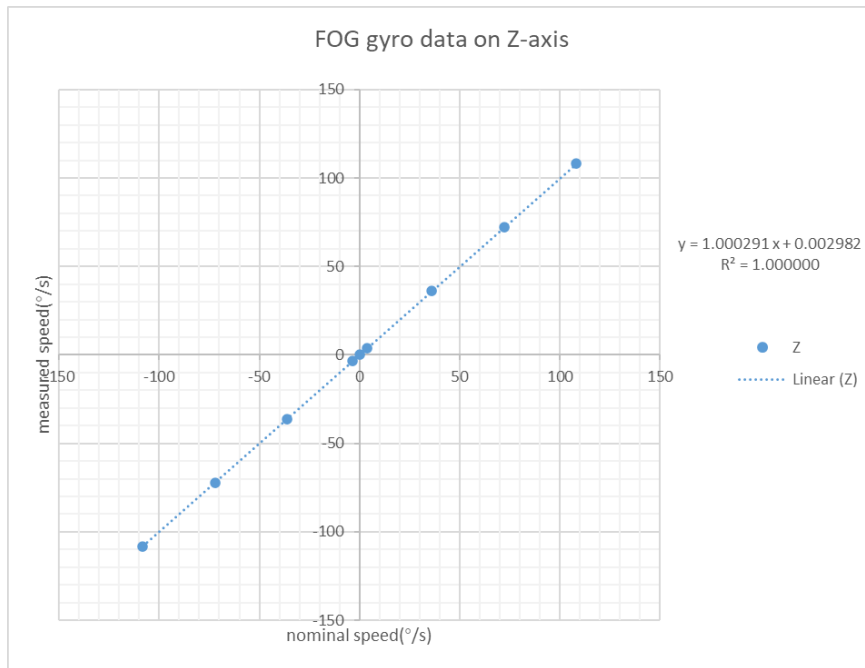


Figure 5.1.1-10 FOG gyro data on Z-axis

Intercept: $a = 0.002982$; Slope: $b = 1.000291$; Correlation coefficient: $R = 1$; Determination coefficient: $R^2 = 1$; standard deviation (standard error): $s = 0.004380$.

The model is

$$\hat{y} = 1.000291x + 0.002982$$

Therefore, $R^2 = 1$ indicates that the regression model has extremely high fitting with test data, this unary linear regression model can be used for data prediction and fitting. $b = 1.000291$ shows that the measured value is very close to the actual value.

One step further, the X-axis and Y-axis can also calculate the regression equation.

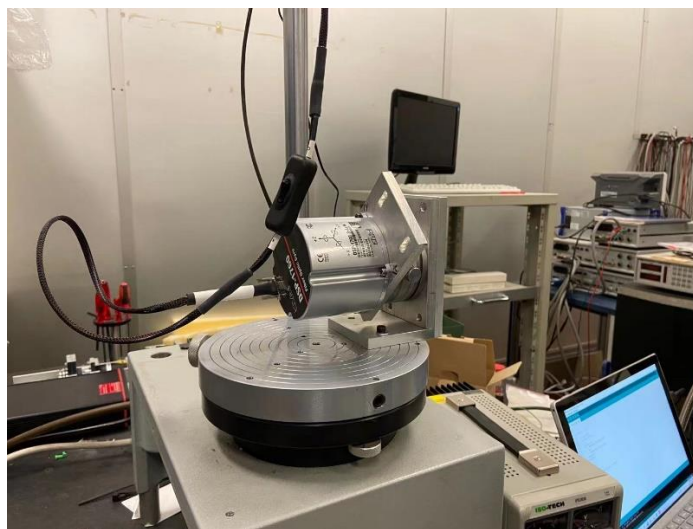


Figure 5.1.1-11 FOG test on X-axis & Y-axis

Table 5.1.1-3 GYRO X-axis data

| FOG_GYRO_Xaxis_data | |
|---------------------|---------------------|
| NOMINAL SPEED(°/s) | measured speed(°/s) |
| -144.2592 | -144.3448233 |
| -108.19292 | -108.2175864 |
| -72.129 | -72.13706794 |
| -36.064 | -36.06582737 |
| -3.606 | -3.599547671 |
| 0 | 0.003267915 |
| 3.606 | 3.605488274 |
| 36.064 | 36.07371836 |
| 72.129 | 72.15004945 |
| 108.19292 | 108.2262363 |
| 144.2592 | 144.3300601 |

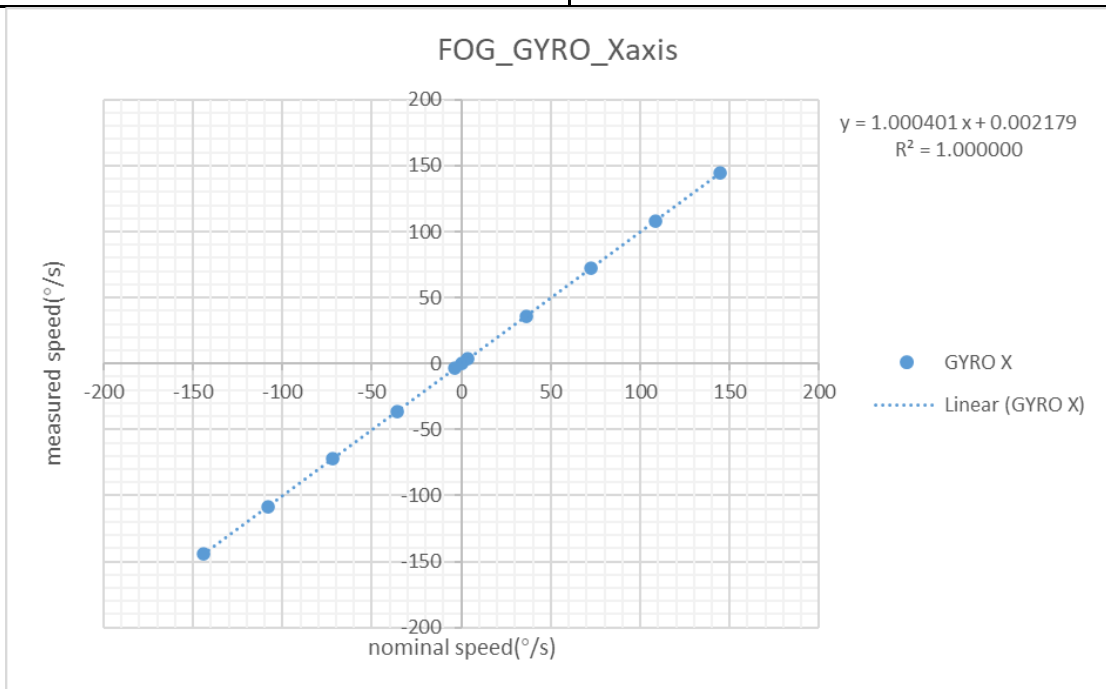


Figure 5.1.1-12 GYRO Xaxis output

Intercept: $a = 0.002179$; Slope: $b = 1.000401$; Correlation coefficient: $R = 1$;
 Determination coefficient: $R^2 = 1$; standard deviation (standard error): $s = 0.015262$.

The model is

$$\hat{y} = 1.000401x + 0.002179$$

On the Y-axis:

Table 5.1.1-4 GYRO data on Y-axis

| FOG_GYRO_Yaxis_data | |
|---------------------|---------------------|
| NOMINAL SPEED(°/s) | measured speed(°/s) |
| -144.2592 | -144.3365312 |
| -108.19292 | -108.2316283 |
| -72.129 | -72.14754025 |
| -36.064 | -36.05350931 |
| -3.606 | -3.60365073 |
| 0 | 0.00279658 |
| 3.606 | 3.609161461 |
| 36.064 | 36.05860694 |
| 72.129 | 72.12591244 |
| 108.19292 | 108.2177434 |
| 144.2592 | 144.3321131 |

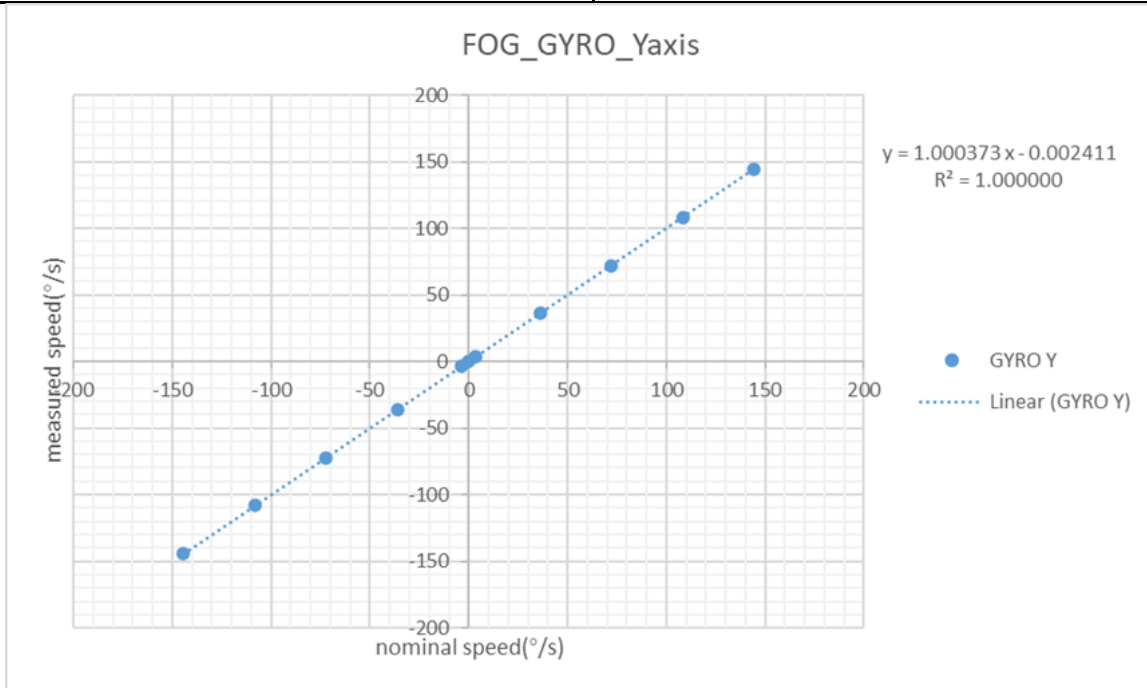


Figure 5.1.1-13 GYRO Yaxis output

Intercept: $a = 0.002411$; Slope: $b = 1.000373$; Correlation coefficient: $R = 1$;
 Determination coefficient: $R^2 = 1$; standard deviation (standard error): $s = 0.018321$.

The model is

$$\hat{y} = 1.000373x + 0.002411$$

5.1.1.2 Earth rotation

In addition, since this is a military high-precision fiber optic gyroscope, I need to verify whether it is affected by the rotation of the earth. The theoretical rotation speed of the earth, calculated on the basis of the earth's rotation within 24 hours a day, has already rotated 360° for one revolution. Then the angular velocity of the earth's rotation is:

$$\omega = \frac{360^\circ}{24 * 60 * 60} = 0.004167 \text{ }^\circ/\text{s}$$

Let's take the Y-axis as an example for analysis. The input signal frequency is 0 Hz. In theory, the sensor is only affected by the rotation of the earth at this time. I fixed the fiber optic gyroscope on the round table, started the data collection, and rotated the platform clockwise about 90° after every 30 seconds, and repeated 4 times to complete a circular rotation. Since the data is very small, in order to facilitate subsequent calculations, I magnify the data by 1×10^8 times in excel. The enlarged image is as follows:

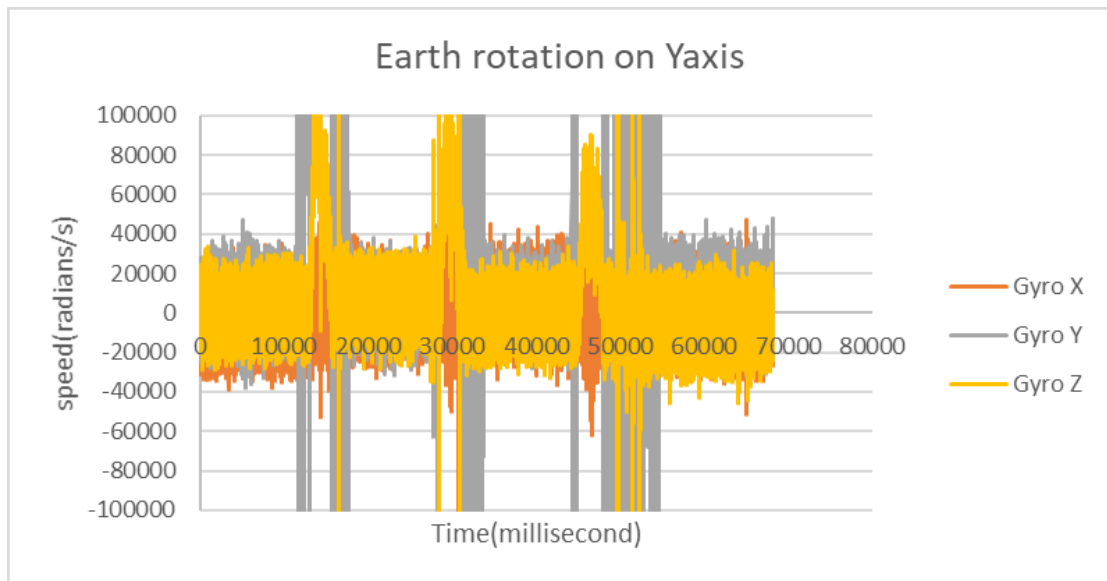


Figure 5.1.1-14 Earth rotation on Y-axis

The speed of each rotation of the circular table is much greater than the rotation speed of the earth, so it is very easy to distinguish each rotation of the circular table in the image. But at this time, the image noise data is mixed with the measured data, and effective information cannot be extracted. The next step is needed, where the moving average method is used to process the data, and the average is calculated every 2000 milliseconds to achieve the effect. After calculating the moving average, as shown below:

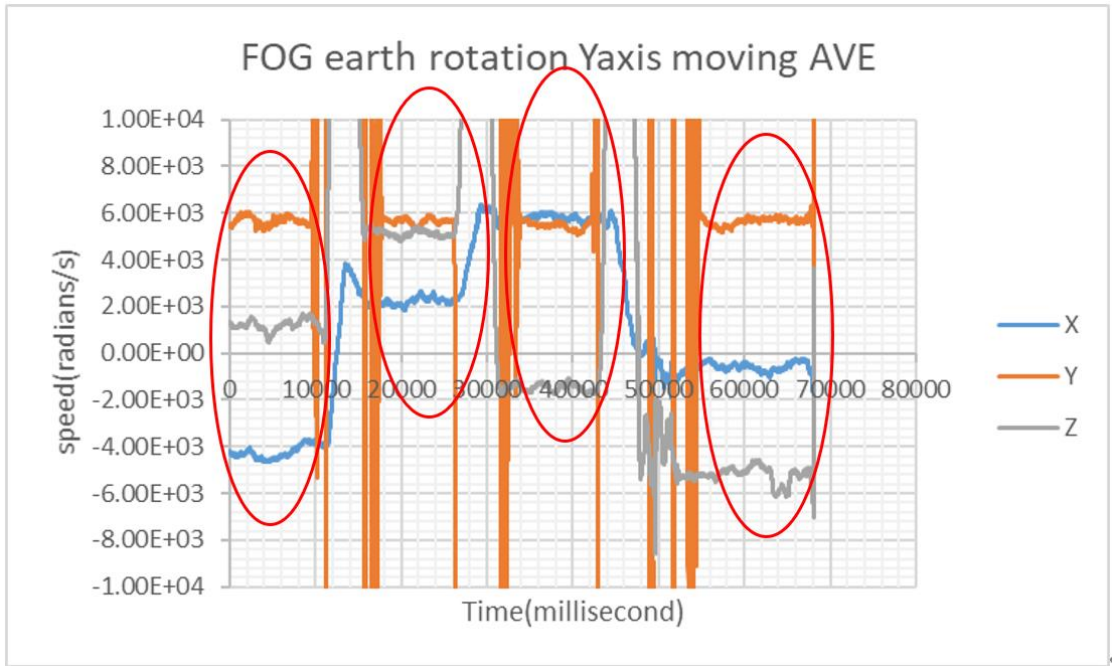


Figure 5.1.1-15 Moving average calculated on Y-axis

As shown in the figure, the measured speed of the X-axis, Y-axis, and Z-axis can be calculated at the four red circles. The table analysis is shown below:

Table 5.1.1-5 earth rotation data on Y-axis

| Table of FOG earth rotation on Yaxis data | | | | | | | | | |
|---|------------|----------|-----------|-----------|------------|------------|----------|-----------|---|
| Angle(°) | X | Y | Z | x p.p. | z p.p. | HOR | VER | TOT rad/s | |
| 0 | -4.28E+03 | 5.62E+03 | 1.19E+03 | 1.01E+04 | 1.03E+04 | 5.11E+03 | 5.59E+03 | 7.57E-05 | 0.00434 °/s |
| 90 | 2.24E+03 | 5.64E+03 | 5.11E+03 | | | | | | real angular Earth's speed |
| 180 | 5.84E+03 | 5.50E+03 | -1.47E+03 | | | | | | |
| 270 | -6.09E+02 | 5.61E+03 | -5.20E+03 | | | | | | |
| 360 | -4282.5697 | 5618.69 | 1189.4625 | | | | | | after subtraction of the earth rotation at 45° parallel |
| 450 | 2240.21738 | 5637.449 | 5110.8915 | | | | | | |
| 540 | 5841.38968 | 5502.564 | -1472.584 | | | | | | |
| 630 | -608.62545 | 5605.268 | -5202.83 | | | | | | |
| | | | | X | Y | Z | | | |
| media(offset) | 7.98E-06 | 5.59E-05 | -9.38E-07 | 4.570E-04 | 2.548E-04 | -5.372E-05 | °/s | | |
| factory test report | | | | 1.000E-04 | -4.700E-05 | -8.060E-05 | °/s | | |

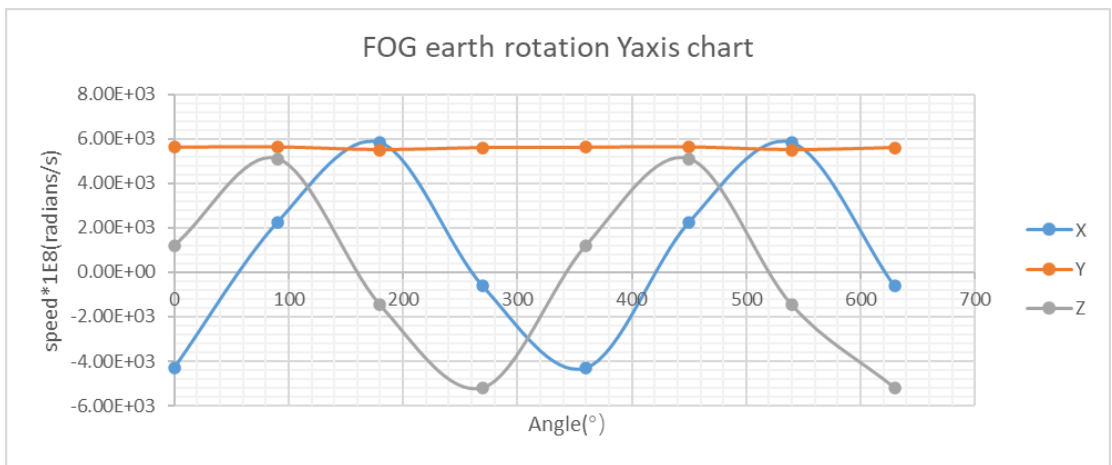


Figure 5.1.1-16 earth rotation on Y-axis

Because the coordinates of Turin on the earth are approximately 45° north latitude, I use the Pythagorean theorem when calculating the rotation angular velocity:

$$c = \sqrt{a^2 + b^2}$$

In the formula, a is the average of x p.p and z p.p, and b is the average rotation speed on Y-axis. The calculated value of the earth's rotation is $0.00434^\circ/s$, and the theoretical value is $0.00417^\circ/s$. The two values are very close, and from the image, the X-axis and Z-axis waveforms have a 90° phase difference.

After analyzing the Y-axis, I analyze the Z-axis and X-axis in the same way. Calculate the angular velocity of the earth's rotation.

On the Z-axis:

Table 5.1.1-6 earth rotation data on Z-axis

| clockwise | Earth rotation effect Z | | | | | | | | |
|----------------------------|-------------------------|-------------|----------|------------------|-------------------|-------------------|----------|-------------|--|
| ANGLE (°) | X | Y | Z | y p.p. | x p.p. | hor | VER z | TOT rad/s | |
| 0 | 1.67E-07 | -5.67E-05 | 4.51E-05 | 9.81E-05 | 1.06E-04 | 5.10E-05 | 4.45E-05 | 6.77202E-05 | 0.00388 ° /s |
| 90 | 6.03E-05 | -5.18E-06 | 4.61E-05 | | | | | | real angular Earth's speed 0.00417 ° /s |
| 180 | 5.93E-06 | 4.15E-05 | 4.33E-05 | | | | | | |
| 270 | -4.58E-05 | -9.82E-06 | 4.36E-05 | | | | | | |
| 360 | 1.667E-07 | -5.6652E-05 | 4.51E-05 | | | | | | |
| 450 | 6.025E-05 | -5.1752E-06 | 4.61E-05 | | | | | | |
| 540 | 5.926E-06 | 4.14534E-05 | 4.33E-05 | | | | | | |
| 630 | -4.58E-05 | -9.8194E-06 | 4.36E-05 | -0.002621 | -0.00056261 | 0.0024963 | | | |
| | | | | X | Y | Z | | | |
| media (offset) | 5.15E-06 | -7.55E-06 | 4.45E-05 | 2.950E-04 | -4.325E-04 | -3.977E-04 | | | ° /s |
| factory test report | | | | 1.000E-04 | -4.700E-05 | -8.060E-05 | | | ° /s |

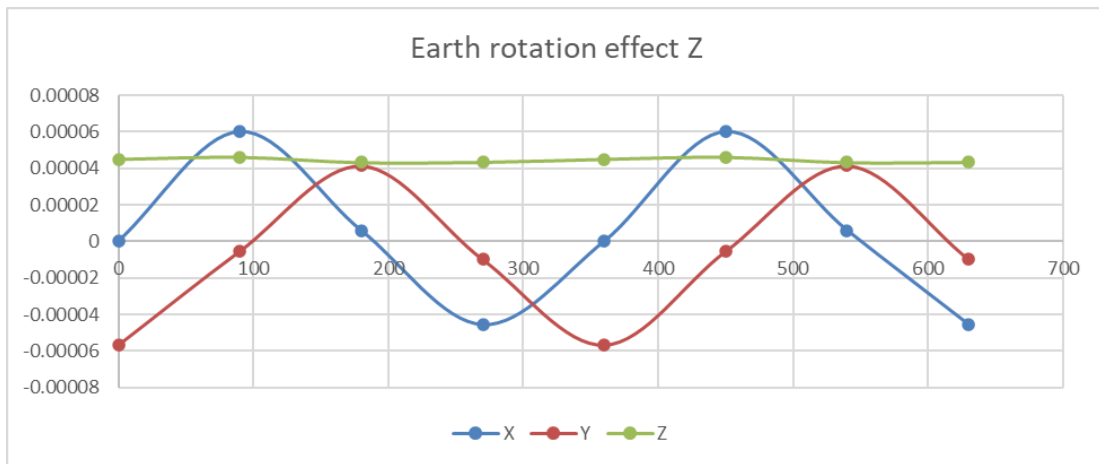


Figure 5.1.1-17 earth rotation on Z-axis

The calculated value of the earth's rotation is $0.00388^\circ/s$, and the theoretical value is $0.00417^\circ/s$.

On the X-axis:

Table 5.1.1-7earth rotation data on X-axis

| Clockwise | earth rotation effect on Xaxis | | | | | | | | | |
|---------------------|--------------------------------|----------|-----------|------------------|-------------------|-------------------|-------------|-----------|-----------------------------------|--------------------|
| | GYRO X | GYRO Y | GYRO Z | Y p. p. | z p. p. | HOR | VER X | TOT rad/s | | |
| 0 | 6.12E-05 | 1.61E-05 | -5.23E-05 | 9.46E-05 | 1.02E-04 | 4.91E-05 | 6.16799E-05 | 7.88E-05 | 0.004515° /s | |
| 90 | 6.07E-05 | 4.81E-05 | 1.646E-05 | | | | | | real angular Earth's speed | 0.00417° /s |
| 180 | 6.35E-05 | -1.3E-05 | 4.936E-05 | | | | | | | |
| 270 | 6.13E-05 | -4.6E-05 | -2.02E-05 | | | | | | | |
| 360 | 6.12E-05 | 1.61E-05 | -5.23E-05 | | | | | | | |
| 450 | 6.07E-05 | 4.81E-05 | 1.646E-05 | | | | | | | |
| 540 | 6.35E-05 | -1.3E-05 | 4.936E-05 | | | | | | | |
| 630 | 6.13E-05 | -4.6E-05 | -2.02E-05 | | | | | | | |
| | | | | X | Y | Z | | | | |
| media(offset) | 6.17E-05 | 1.09E-06 | -1.66E-06 | 3.534E-03 | 6.234E-05 | -3.044E-03 | | | | |
| factory test report | | | | 1.00E-04 | -4.700E-05 | -8.060E-05 | | | | |

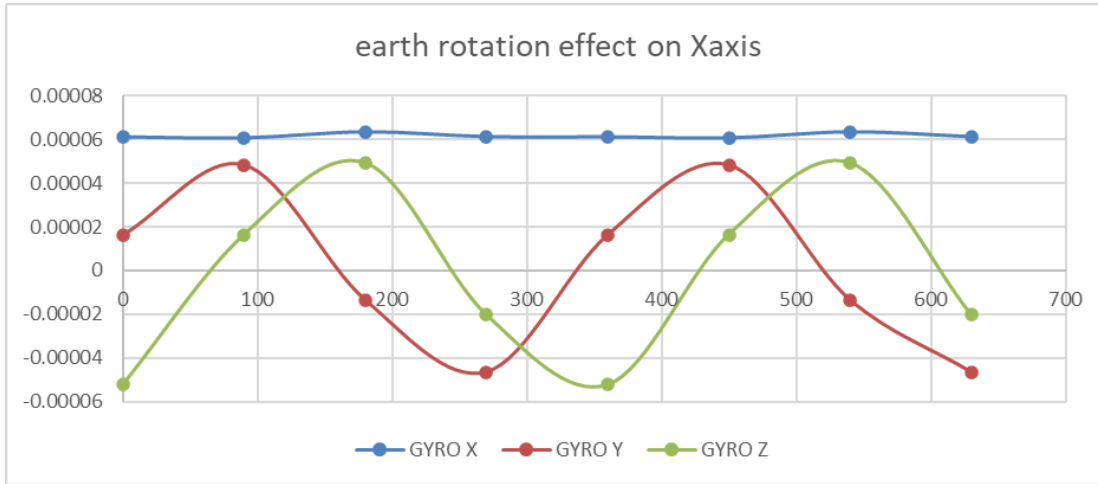


Figure 5.1.1-18 earth rotation on X-axis

The calculated value of the earth's rotation is 0.004515°/s, and the theoretical value is 0.00417°/s.

5.1.2 IMU

5.1.2.1 For the gyro part

There is a three-axis gyroscope inside the IMU. Considering that this function can be used as an optional function in the future, I will test the gyroscope. The test procedure is the same as the test content of the fiber optic gyroscope. Use the Arduino UNO board to generate signals of different frequencies and use these digital signals to control the rotation of the stepping motor to drive the rotation of the round table. For the testing on the Z-axis, use the pressure piece and two M5 hexagon socket bolts to fix the sensor.

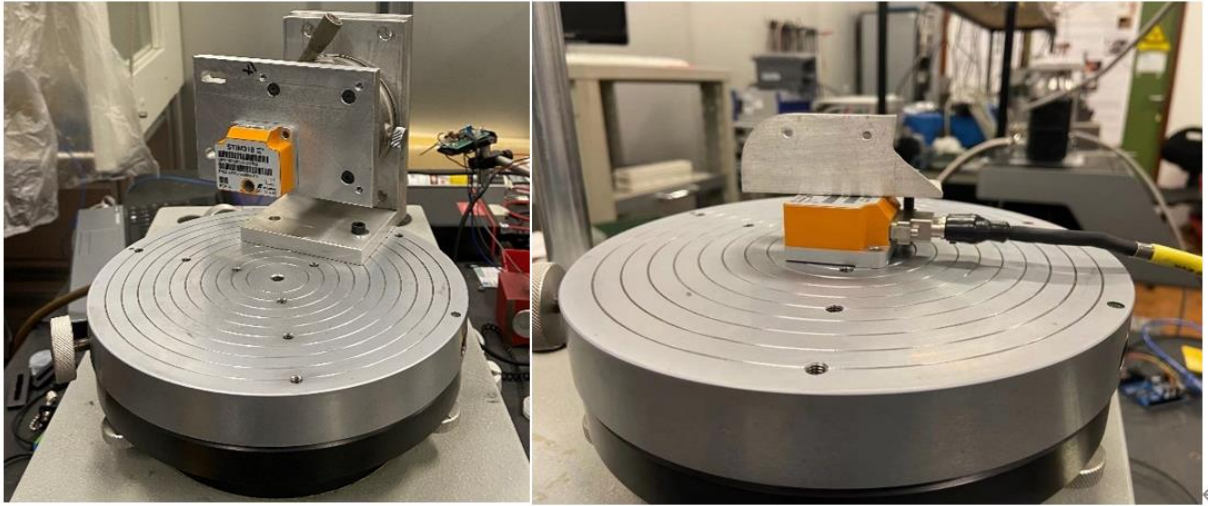


Figure 5.1.2-1 STIM318 on platform

First, the data of IMU gyro-X-axis:

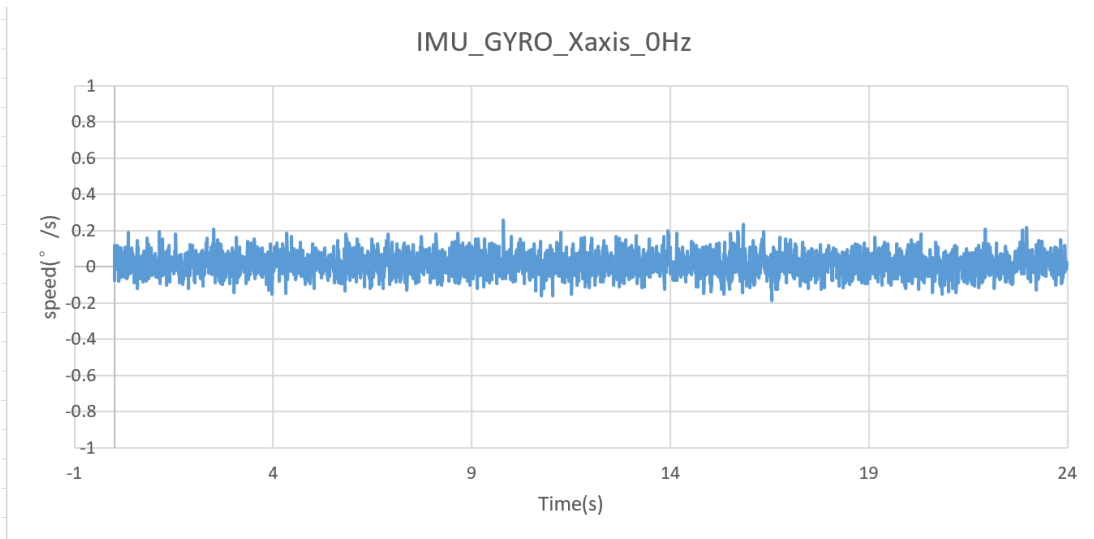


Figure 5.1.2-2 IMU gyro X-axis with 0Hz

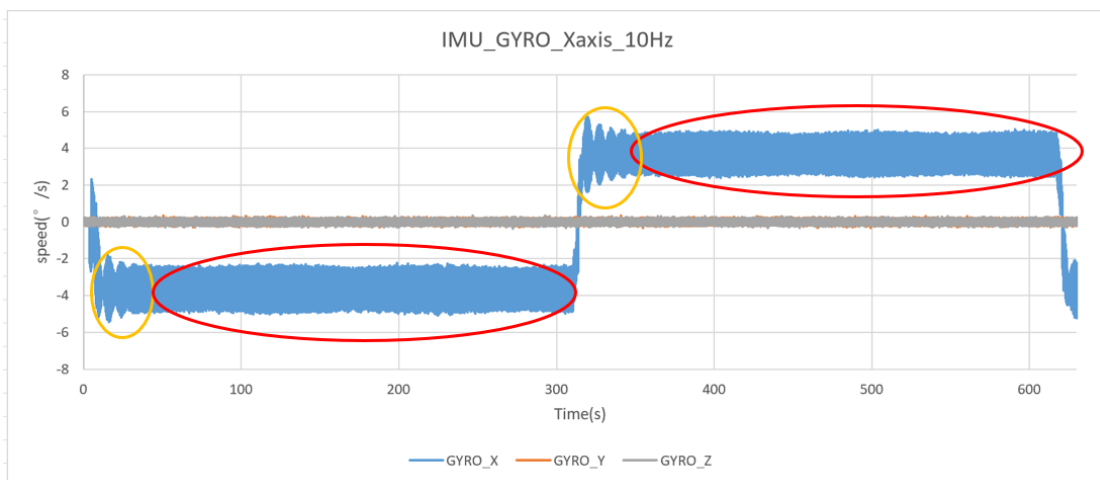


Figure 5.1.2-3 IMU GYRO X-axis with 10Hz

It can be roughly seen from the image that the performance of the gyroscope is very stable. When the input frequency is 10Hz and the rotation speed is 3.6°/s, at the red circle mark in Figure XXX, the sensor is at a fixed speed, and the speed value fluctuates uniformly and densely. , Thus forming a thick line in the image. This is because, in the case of extremely low speed, the digital input signal will cause the stepper motor to vibrate. Because the signal changes between 0 and 1, it is a high frequency for the motor to start and stop again and again. It can be observed from the power supply that the working current of the stepper motor jumps between 0.5A and 1A. In addition, when each section of the motor just reaches the normal speed, the vibration amplitude of the motor will be greater. In order to ensure that the data is closer to the true value, in data processing, I only use the second half of the mean value calculation.

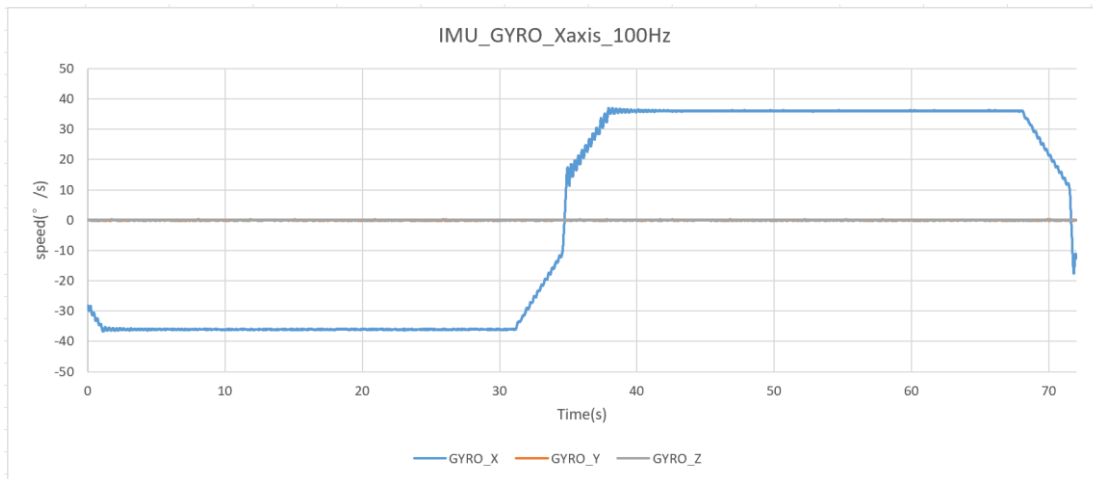


Figure 5.1.2-4 GYRO X-axis with 100Hz

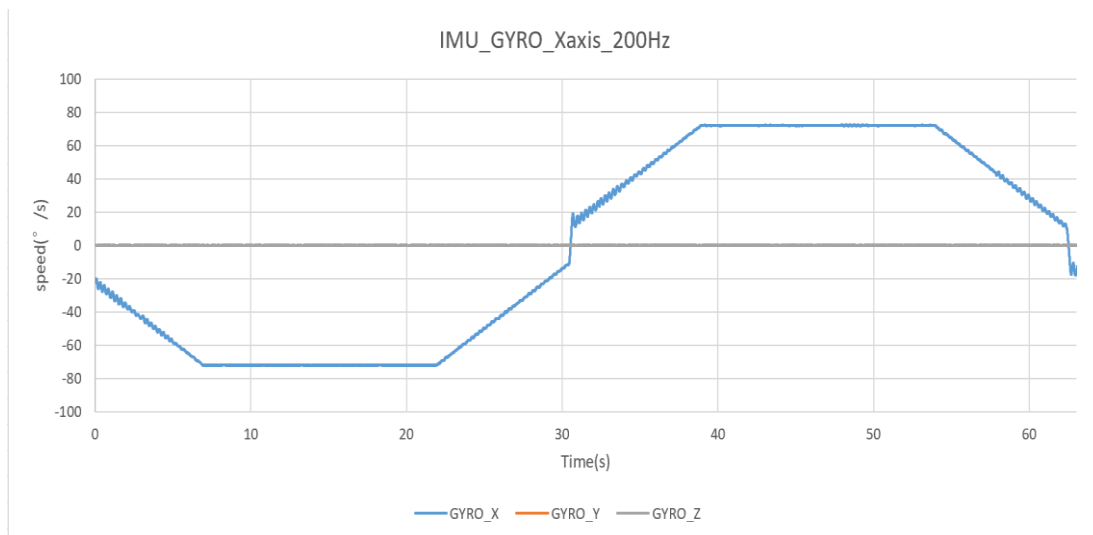


Figure 5.1.2-5 GYRO X-axis with 200Hz

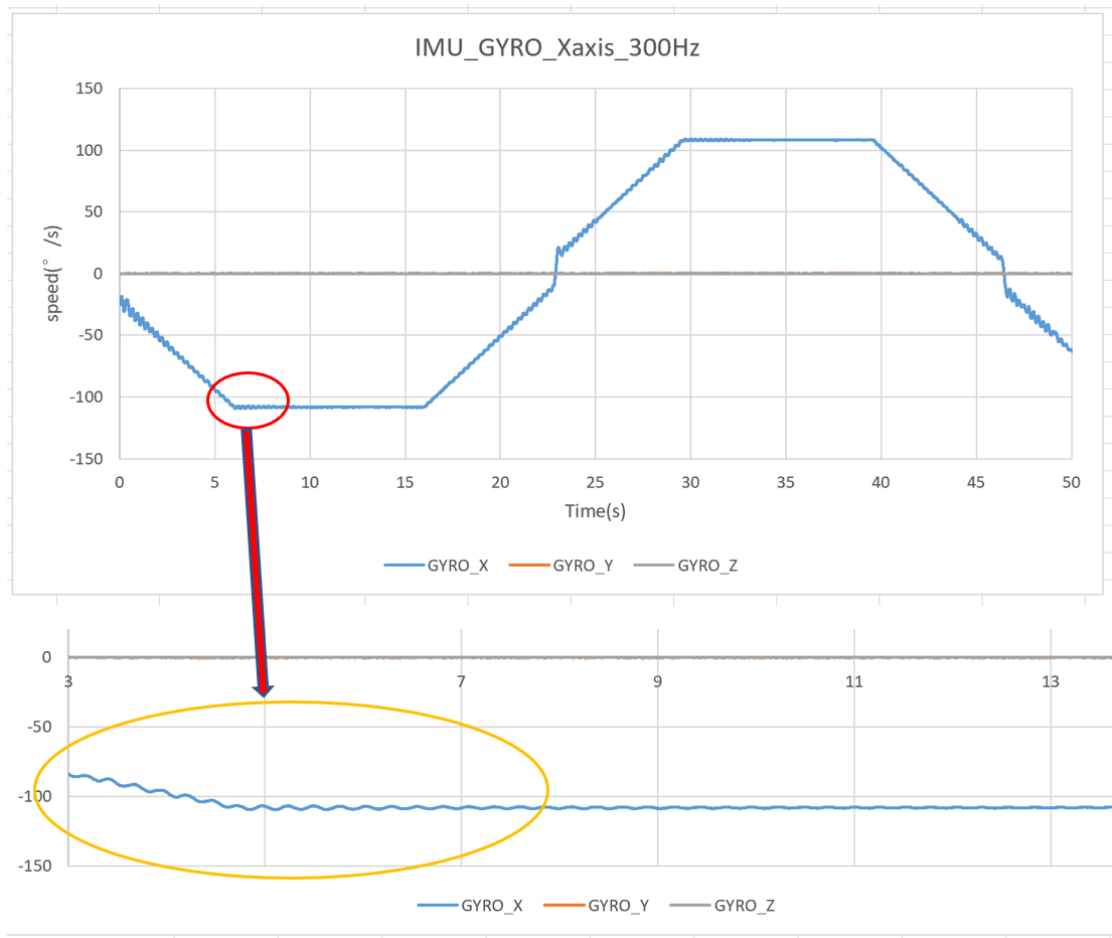


Figure 5.1.2-6 GYRO X-axis with 300Hz

In order to avoid this problem also appearing in other frequency tests, when I zoomed in the image of 300Hz frequency, I can also find that the motor speed jittered when entering the initial stage of constant speed. Therefore, for all gyroscope data processing, I will all take the second half of the constant speed range for calculation. The following is the calculation result table:

Table 5.1.2-1 GYRO X-axis data

| Signal frequency(Hz) | Nominal speed(° /s) | Measured speed(° /s) |
|----------------------|---------------------|----------------------|
| 300.5374 | 108.1934573 | 108.2015484 |
| 200.3584 | 72.12901158 | 72.11124319 |
| 100.1791 | 36.06449307 | 36.0734221 |
| 100.1791 | 3.606449307 | 3.623369699 |
| 0 | 0 | 0.016211 |
| 100.1791 | -3.606449307 | -3.591364965 |
| 100.1791 | -36.06449307 | -36.04332759 |
| 200.3584 | -72.12901158 | -72.08095778 |
| 300.5374 | -108.1934573 | -108.1610059 |

According to the data in the table, I calculate the linear regression relationship between the nominal speed and the measured speed.

Table 5.1.2-2 GYRO X-axis regression

| Regression Statistics of X-axis | | | | |
|---------------------------------|--|--|--|----------|
| Multiple R | | | | 1.000000 |
| R Square | | | | 1.000000 |
| Adjusted R Square | | | | 1.000000 |
| Standard Error | | | | 0.011335 |
| Observations | | | | 9 |

| | Coefficients | Standard Error | t Stat | P-value |
|-------------------------|--------------|----------------|-------------|-------------|
| Intercept | 0.016571 | 0.003778194 | 4.385932018 | 0.00321123 |
| Nominal speed (° /s) | 0.999785 | 5.93734E-05 | 16838.95623 | 6.87969E-28 |

| ANOVA | | | | |
|------------|----|-------------|-------------|-------------|
| | df | SS | MS | F |
| Regression | 1 | 36428.51099 | 36428.51099 | 283550446.8 |
| Residual | 7 | 0.000899309 | 0.000128473 | |
| Total | 8 | 36428.51189 | | |

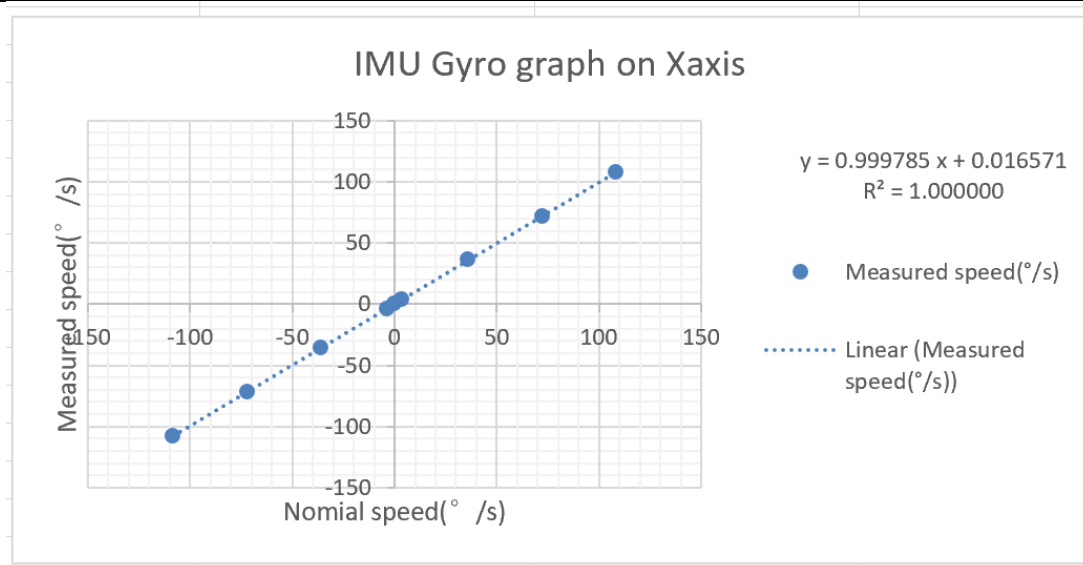


Figure 5.1.2-7 IMU_GYRO X-axis output

Finally, read the regression results as follows:

Intercept: $a = 0.016571$; Slope: $b = 0.999785$; Correlation coefficient: $R = 1$;
 Determination coefficient: $R^2 = 1$; F value: $F = 283550446.8$; t value: $t = 16838.95623$;
 standard deviation (standard error): $s = 0.011335$; regression sum of squares: $SSR = 36428.51099$

; the residual sum of squares: $SSE = 0.000899309$; The error sum of squares of y is the total sum of squares: $SST = 36428.51189$.

The model is

$$\hat{y} = 0.999785x + 0.016571$$

Therefore, $R^2 = 1$ indicates that the regression model has extremely high fitting test data within the range of 0-100°/s angular velocity required by the test, this unary linear regression model can be used for data prediction and fitting.

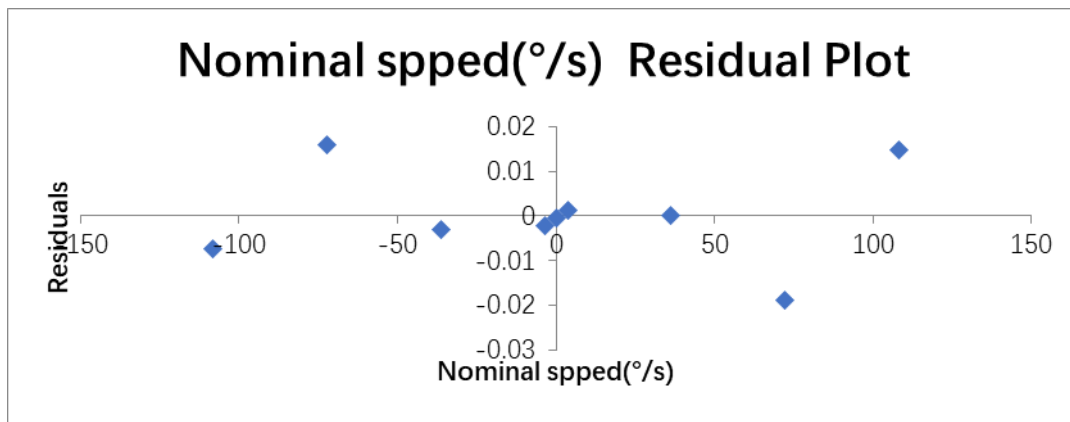


Figure 5.1.2-8 Residual of IMU GYRO X-axis

The data on the Y-axis and Z-axis

Through the test of the X-axis, I can know that the relationship between the gyro data output of the IMU and the input signal is very linear. Therefore, in the process of testing the Y-axis and Z-axis, I can simplify the test data. I will select the maximum frequency and zero frequency for testing.

The following table shows the data collection results of the Y axis:

Table 5.1.2-3 IMU_GYRO_Yaxis data

| Nominal Frequency (Hz) | Nominal speed(°/s) | Measured speed(°/s) |
|------------------------|--------------------|---------------------|
| 300.5374 | 108.1934573 | 108.173761 |
| 0 | 0 | 0.007385183 |
| -300.5374 | -108.1934573 | -108.1424659 |

Plotting and linear regression analysis based on data:

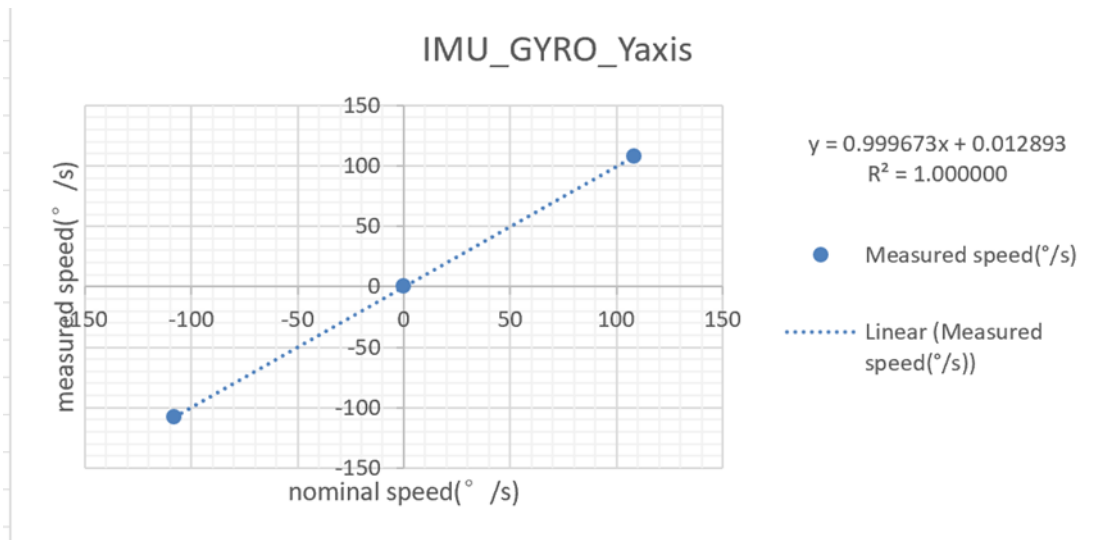


Figure 5.1.2-9 IMU_GYRO_Yaxis

Table 5.1.2-4 Regression of IMU GYRO Y-axis

| Regression Statistics of Y-axis | |
|---------------------------------|----------|
| Multiple R | 1.000000 |
| R Square | 1.000000 |
| Adjusted R Square | 1.000000 |
| Standard Error | 0.006746 |
| Observations | 3 |

Intercept: $a = 0.012893$; Slope: $b = 0.999673$; Correlation coefficient: $R = 1$; Determination coefficient: $R^2 = 1$; standard deviation (standard error): $s = 0.006746$. So the model of the Y-axis is:

$$\hat{y} = 0.999673x + 0.012893$$

This means this regression model has extremely high fitting test data.

For the Z axis testing. More same as Y axis. The following table shows the data collection results of the Z axis:

Table 5.1.2-5 IMU GYRO z-axis data

| NOMINAL FREQUENCY(Hz) | nominal speed(°/s) | measured speed(°/s) |
|-----------------------|--------------------|---------------------|
| 300.5373815 | 108.1934573 | 108.1070803 |
| 0 | 0 | 0.0015035 |
| -300.5373815 | -108.1934573 | -108.0551597 |

Plotting and linear regression analysis based on data:

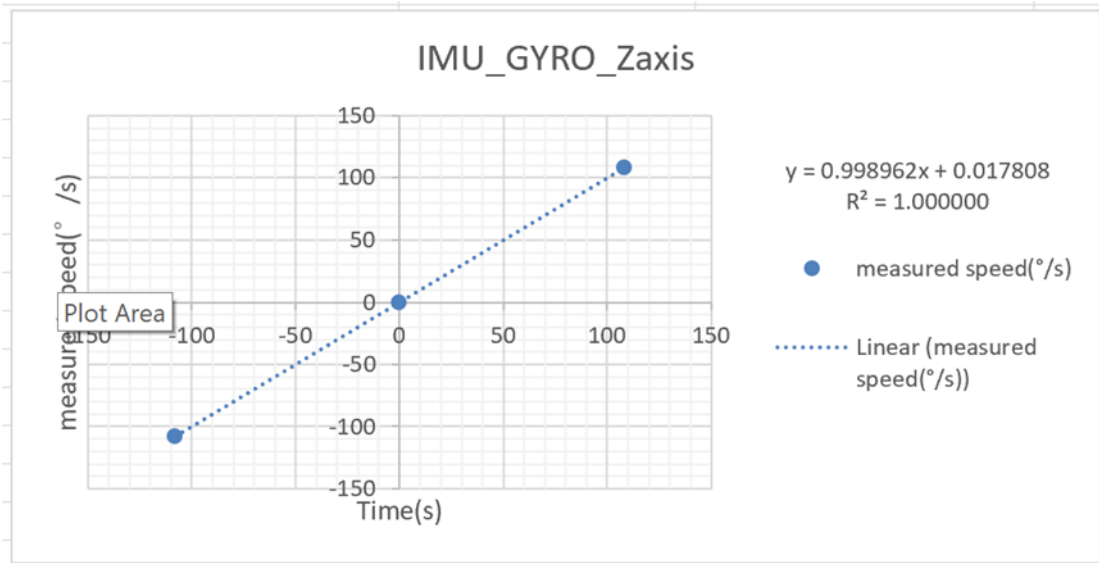


Figure 5.1.2-10 IMU GYRO z-axis

Table 5.1.2-6 Regression on IMU GYRO z-axis

Regression Statistics of Z-axis

| | |
|-------------------|----------|
| Multiple R | 1.000000 |
| R Square | 1.000000 |
| Adjusted R Square | 1.000000 |
| Standard Error | 0.019969 |
| Observations | 3 |

Intercept: $a = 0.017808$; Slope: $b = 0.998962$; Correlation coefficient: $R = 1$; Determination coefficient: $R^2 = 1$; standard deviation (standard error): $s = 0.019969$. So the model of the Z-axis is:

$$\hat{y} = 0.998962x + 0.019969$$

This means this regression model has extremely high fitting test data.

5.1.2.2 Accelerometer data

In the accelerometer test, I will use three different experimental platforms to test the accelerometer performance of the IMU. The test content includes low-frequency motion and high-frequency motion. I test the accelerometer performance under low-frequency motion on the horizontal shaker, test the performance under high-frequency motion on the horizontal slide platform and vertical shaker. Here is the sensor tested on two kinds of the testing platform:

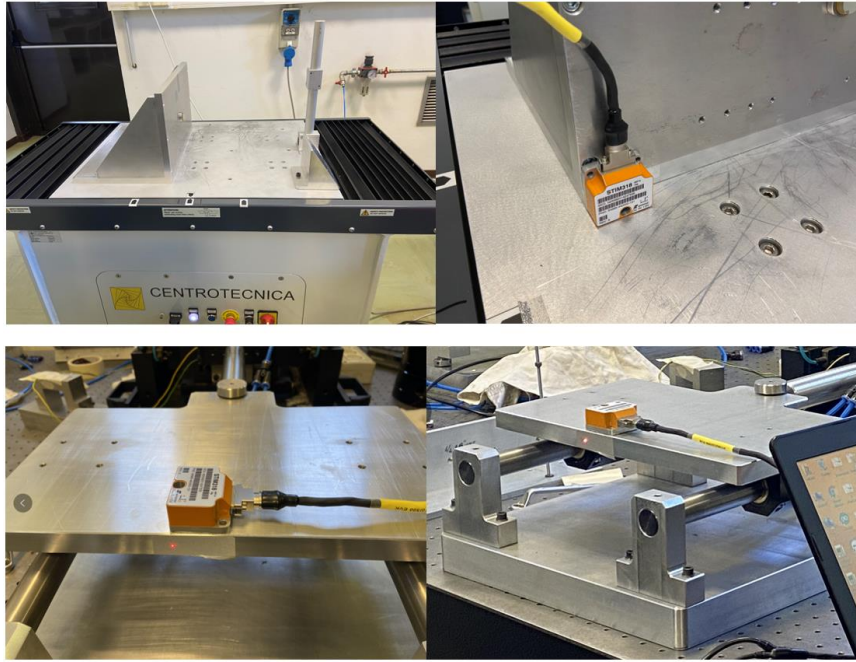


Figure 5.1.2-11 sensor on the Horizon platform

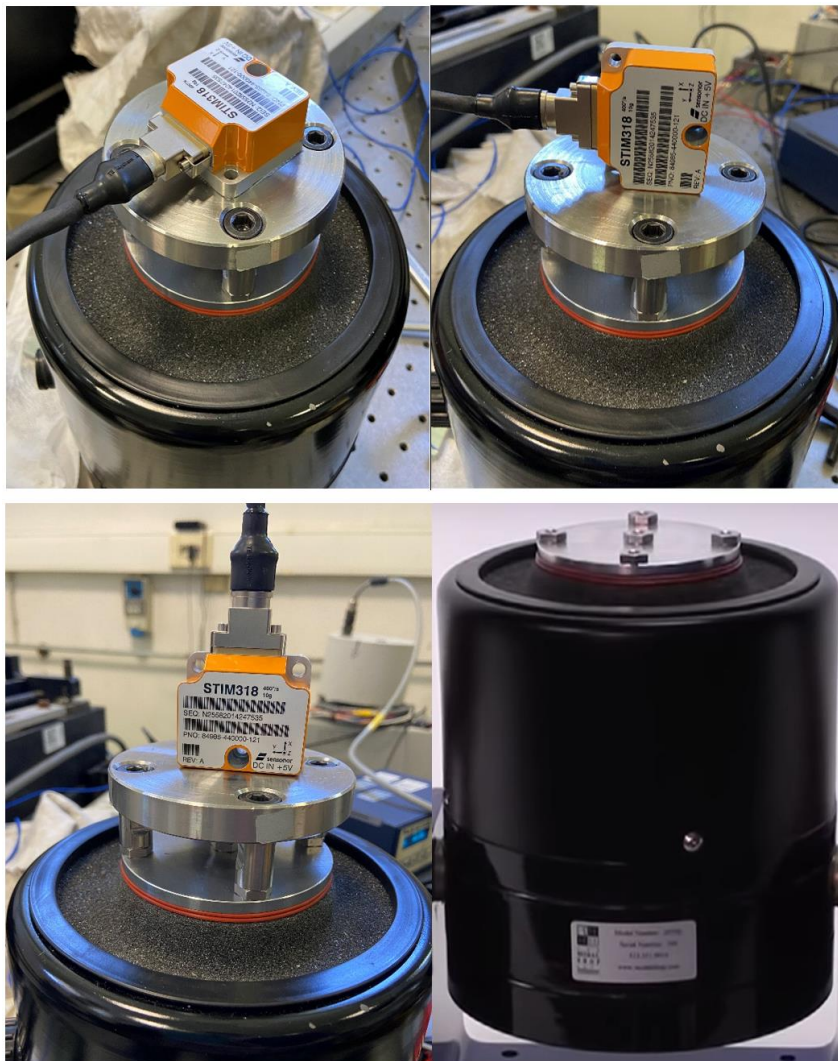


Figure 5.1.2-12 sensor on the vertical testing platform

For the low-frequency test

In the low-frequency test, the image generated by the data will have obvious jitter, and the jitter change of the value is very regular. I am quite sure that the signal curve generated by LabVIEW must be a sinusoid curve. The reason for this kind of situation is that the movement of the horizontal shaker is controlled by the air pump, which will jitter at low frequencies. Therefore, when processing the data, I create a fitting curve, and by continuously adjusting the parameters of this curve, the value of each point on the original image and the corresponding value on the fitting curve are calculated as residuals. When the total residual is the smallest, it means that this fitted curve is the best-fitted curve. Its most basic form as a function of time (t) is:

$$y(t) = A\sin(2\pi ft + \varphi) = A\text{sine}(\omega t + \varphi)$$

A : amplitude, the peak deviation of the function from zero.

f : ordinary frequency, the number of oscillations (cycles) that occur each second of time.

ω : $\omega = 2\pi f$, angular frequency, the rate of change of the function argument in units of radians per second

φ : phase shift (the image moves left and right on the x-axis)

For example, the graph of X-axis with 1Hz:

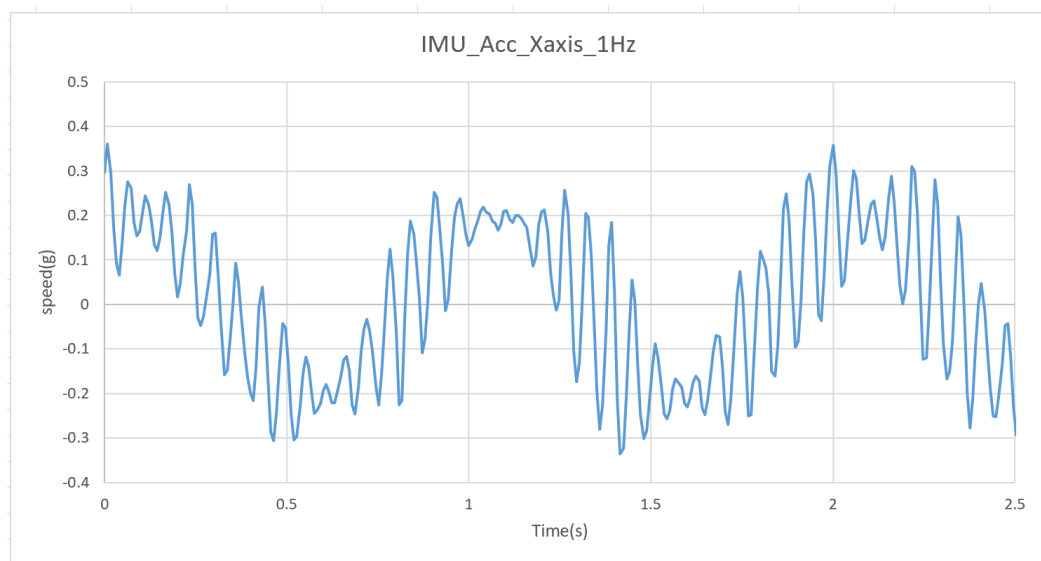


Figure 5.1.2-13 Acc output with 1Hz

In this case, the signal frequency is 1Hz, the acceleration I set is 0.2g. So the amplitude of the sinusoidal curve $A = 0.2$, $\omega = 2\pi f = 2\pi \approx 6.2832$. Thus I could get the model formula:

$$y(t) = 0.2 \sin(6.2832t + \varphi)$$

Create 3 columns of workspace in excel, the first column calculates the fitted curve, the second column calculates the variance, and the third column calculates the average of the variance. The variance calculation is done through each point on the original curve and the point on the fitted curve. First, adjust the phase displacement variable φ , Minimize the sum of variance, when it reaches the minimum, start to adjust the amplitude A . The fitting curve is showing below:

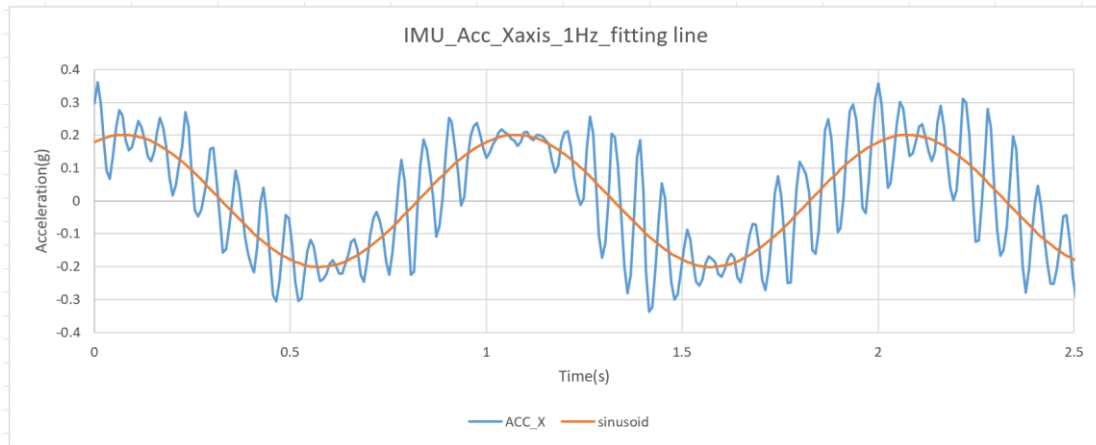


Figure 5.1.2-14 fitting line of acc X-axis 1Hz

The best sinusoid function is:

$$y(t) = 0.2010 \sin(6.2832t + 1.100)$$

After obtaining the best-fitting sinusoid function, I only need to pay attention to the amplitude of the function, which is the variable A. The nominal output amplitude value of the test platform is 0.2g, and the gain between the actual data and the nominal data can be obtained as:

$$\frac{0.201}{0.2} = 1.005$$

According to the data processing method of the X-axis, the following is the performance of the Y-axis and Z-axis in low-frequency motion.

Table 5.1.2-7 IMU ACC gain of each axis

| Frequency(Hz) | gain on each axis | | |
|---------------|-------------------|-------|-------|
| | X | Y | Z |
| 0.5 | 1.006 | 1 | 1.002 |
| 1 | 1.008 | 1.005 | 1.005 |
| 2 | 1.004 | 1.004 | 1.004 |

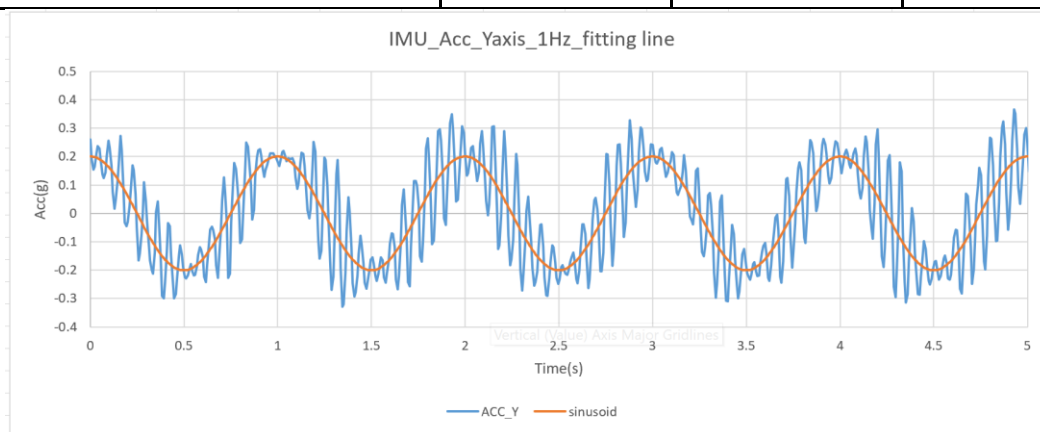


Figure 5.1.2-15 IMU Acc Y-axis 1Hz fitting line

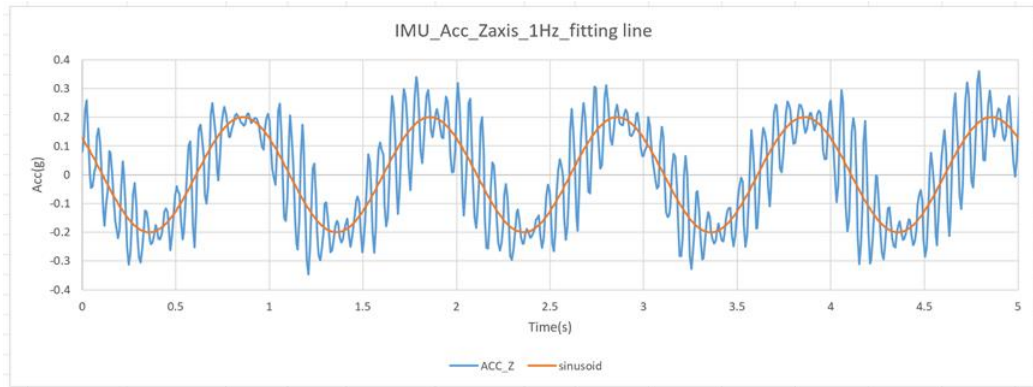


Figure 5.1.2-16 IMU Acc Z-axis 1Hz fitting line

For the High-Frequency test

By observing the output results under high-frequency motion, take the X-axis as an example. It can be seen from the image that under high-frequency motion, the image collected by the accelerometer is very smooth. At the same time, I noticed that there will be noise at the position of the peak and trough of the image. follow a periodic pattern, which means the noise is deterministic. In this image, the value that affects the amplitude has two forms. I decided to calculate the average of the first, and then calculate the two averages to find a common average. In theory, I may have potential risks in doing so, but in the actual IMU test, I have observed that its effect is very good. The overall performance is very good.

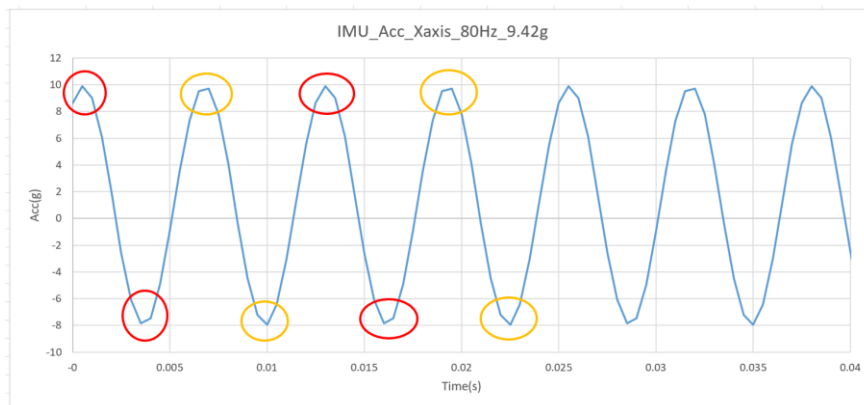


Figure 5.1.2-17 IMU ACC X-axis 80Hz 9.42g

In excel, I process the data. Because the image period is constant, the different peak values produced by the two types of noise have regular changes. For example, the first wave peak is produced at 0.0005 seconds. In the excel table, the data's position is column B, row 3. The second peak of the same performance occurs at 0.013 seconds, that is, column B, row 28. The time interval is 0.0125 seconds, and there is a difference of 25 rows between the two rows of data. According to the INDEX formula in excel, I set:

$$INDEX(B:B, (ROW(B2) - 1) * 25 - 22,)$$

In this formula, $B:B$ means I will analyze the whole data in the B column. The number 25 I set to collect data once every 25 rows. The first data I collect is B3, so I need $ROW(B2) - 1) * 25 - 22$, the result of this part is $ROW(B3)$.

Table 5.1.2-8 IMU Acc X-axis 80Hz calculated data

| | | positive peak | negative peak | acc(g) | POSITIVE | NEGATIVE | Acc(g) | AVE g |
|---------------|-------|---------------|---------------|------------|-------------|------------|-------------|-------------|
| POSITIVE part | ROW3 | 9.8925095 | -7.8538418 | 8.87317565 | 9.7258034 | -7.9456177 | 8.83571055 | 8.853769971 |
| | ROW28 | 9.8965473 | -7.8505096 | 8.87352845 | 9.7270451 | -7.9450016 | 8.83602335 | |
| | ROW16 | 9.8946438 | -7.8545647 | 8.87460425 | 9.7260513 | -7.9439354 | 8.83499335 | |
| | ROW41 | 9.8953552 | -7.8507061 | 8.87303065 | 9.7282295 | -7.9456768 | 8.83695315 | |
| NEGATIVE part | ROW9 | 9.8919125 | -7.8517036 | 8.87180805 | 9.7280178 | -7.9465866 | 8.8373022 | |
| | ROW34 | 9.8941402 | -7.8496819 | 8.87191105 | 9.7274857 | -7.946413 | 8.83694935 | |
| | ROW22 | 9.892313 | -7.8518009 | 8.87205695 | 9.7285347 | -7.9436588 | 8.83609675 | |
| | ROW47 | 9.8928776 | -7.8500023 | 8.87143995 | 9.7297001 | -7.9446449 | 8.8371725 | |
| | | 9.8897552 | -7.8491306 | 8.8694429 | 9.7279701 | -7.9448776 | 8.83642385 | |
| | | 9.8946438 | -7.8481369 | 8.87139035 | 9.7288914 | -7.9443474 | 8.8366194 | |
| | | 9.8911171 | -7.8492489 | 8.870183 | 9.7281399 | -7.9448109 | 8.8364754 | |
| | | 9.8932438 | -7.8468857 | 8.87006475 | 9.7300472 | -7.9445438 | 8.8372955 | |
| | | 9.8895569 | -7.8470879 | 8.8683224 | 9.7295952 | -7.9453888 | 8.837492 | |
| | | 9.8940544 | -7.8458405 | 8.86994745 | 9.7310085 | -7.9446487 | 8.8378286 | |
| | | 9.8914261 | -7.8481483 | 8.8697872 | 9.7296181 | -7.9456673 | 8.8376427 | |
| | | 9.8924656 | -7.846035 | 8.8692503 | 9.7310619 | -7.9441109 | 8.8375864 | |
| | | 9.8894939 | -7.8449631 | 8.8672285 | 9.7303734 | -7.9463444 | 8.8383589 | |
| | | 9.8903313 | -7.8435478 | 8.86693955 | 9.7308712 | -7.9458256 | 8.8383484 | |
| | | 9.8883877 | -7.8462906 | 8.86733915 | 9.7310886 | -7.9451675 | 8.83812805 | |
| | | 9.8911648 | -7.8430672 | 8.867116 | 9.731638 | -7.9460258 | 8.8388319 | |
| | | | | ave= | 8.870428328 | ave= | 8.837111615 | |

Use the same data processing method on the Y-axis and Z-axis. Under the condition of a fixed frequency of 80Hz, I test different acceleration values for analysis. And get the results of the X-axis, Y-axis, and Z-axis respectively.

Table 5.1.2-9 IMU Acc X-axis with 80Hz

| ACC_Xaxis_80Hz_behavior | | |
|-------------------------|----------------|-----------------|
| signal frequency(Hz) | nominal Acc(g) | measured Acc(g) |
| 80 | 0.695 | 0.653160435 |
| 80 | 1.242 | 1.165900371 |
| 80 | 2.56 | 2.408275724 |
| 80 | 5.04 | 4.733247591 |
| 80 | 8.08 | 7.60520241 |
| 80 | 9.42 | 8.853769971 |

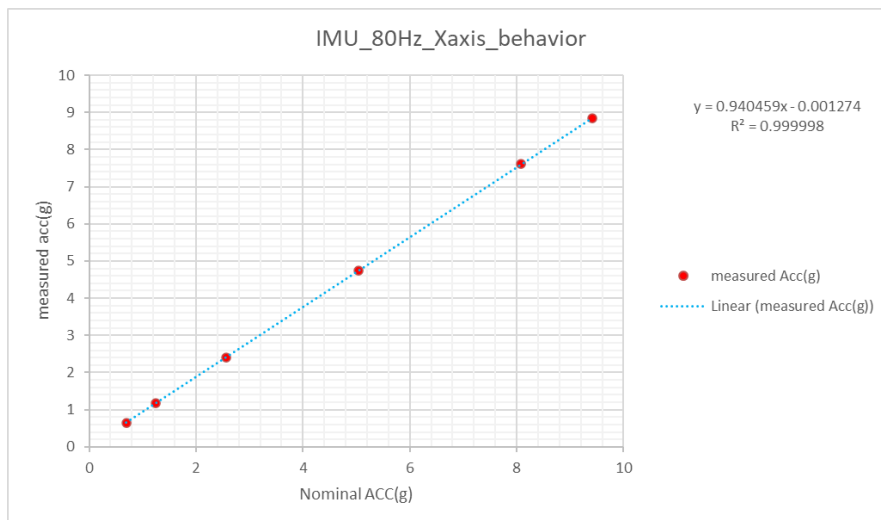


Figure 5.1.2-18 IMU_80Hz_X-axis behavior

Table 5.1.2-10 Regression of X-axis with 80Hz

| Regression Statistics of Xaxis_80Hz | | | | |
|-------------------------------------|--------------|----------------|--------------|-------------|
| Multiple R | | | | 0.999999 |
| R Square | | | | 0.999998 |
| Adjusted R Square | | | | 0.999998 |
| Standard Error | | | | 0.005204 |
| Observations | | | | 6 |
| ANOVA | | | | |
| | df | SS | MS | F |
| Regression | 1 | 58.52529624 | 58.52529624 | 2161258.349 |
| Residual | 4 | 0.000108317 | 2.70793E-05 | |
| Total | 5 | 58.52540455 | | |
| | Coefficients | Standard Error | t Stat | P-value |
| Intercept | -0.001274 | 0.003581 | -0.355808352 | 0.739955819 |
| nominal Acc (g) | 0.940459 | 0.000640 | 1470.121882 | 1.28451E-12 |

Intercept: $a = -0.001274$; Slope: $b = 0.940459$; Correlation coefficient: $R = 0.999999$; Determination coefficient: $R^2 = 0.999999$; standard deviation (standard error): $s = 0.005204$.

The model is

$$\hat{y} = 0.940459x - 0.001274$$

Therefore, $R^2 = 0.999998$ indicates that the regression model has extremely high fitting with test data, this unary linear regression model can be used for data prediction and fitting. One step further, the Y-axis and Z-axis can also calculate the regression equation.

Table 5.1.2-11 IMU Acc Y-axis 80Hz

| ACC_Yaxis_80Hz_behavior | | |
|-------------------------|-----------------|-----------------|
| signal frequency(Hz) | nominal Acc (g) | measured Acc(g) |
| 80 | 1.4 | 1.287564323 |
| 80 | 2.09 | 1.983607 |
| 80 | 4.14 | 3.931889633 |
| 80 | 8.11 | 7.719745545 |

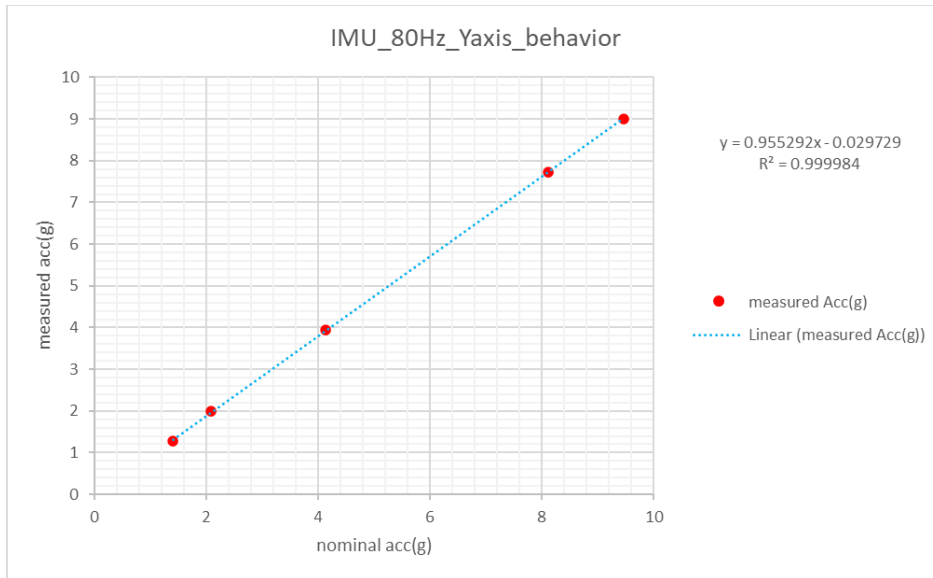


Figure 5.1.2-19 IMU_80Hz_Yaxis behavior

Intercept: $a = -0.029729$; Slope: $b = 0.955292$; Determination coefficient: $R^2 = 0.999984$; standard deviation (standard error): $s = 0.015967$.

The model is

$$\hat{y} = 0.955292x - 0.029729$$

On the Z-axis:

| ACC_Zaxis_80Hz_behavior | | |
|-------------------------|-----------------|------------------|
| Frequency (Hz) | nominal acc (g) | measured acc (g) |
| 80 | 0.11 | 0.104152728 |
| 80 | 0.502 | 0.475255913 |
| 80 | 1.01 | 0.95865712 |
| 80 | 2.01 | 1.901414074 |
| 80 | 4.01 | 3.78487949 |
| 80 | 5.99 | 5.64255381 |
| 80 | 7.94 | 7.47470212 |
| 80 | 8.452 | 7.969751933 |
| 80 | 9.55 | 8.99746957 |

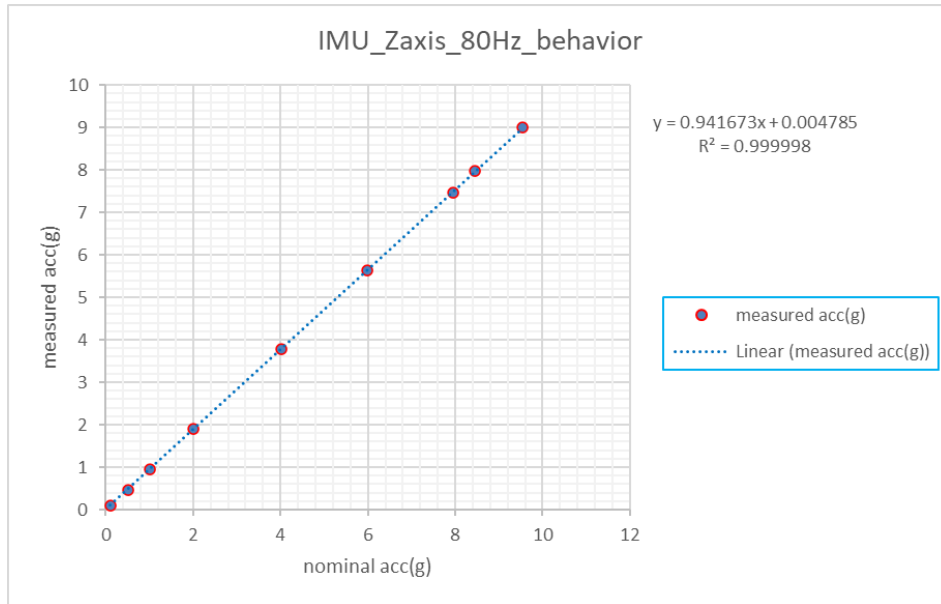


Figure 5.1.2-20 IMU_80Hz_Z-axis behavior

Intercept: $a = 0.004785$; Slope: $b = 0.941673$; Determination coefficient: $R^2 = 0.999998$; standard deviation (standard error): $s = 0.004683$.

The model is

$$\hat{y} = 0.941673x + 0.004785$$

In the above three regression equations, the regression coefficients are all-around 0.95. It means that there is about 5% difference between the measured value and the output value. For sensor applications, this is not a good enough result. The closer the regression coefficient is to 1, the closer the sensor measured value is to the true value. At the same time, I can also find that in the low-frequency exercise test, the regression coefficient is very close to 1. Because I need to further test the performance of the accelerometer at different frequencies.

Table 5.1.2-12 X-axis different frequency

| X-axis frequency behavior | |
|---------------------------|-------------|
| frequency (Hz) | gain |
| 0.5 | 1.006 |
| 1 | 1.008 |
| 2 | 1.004 |
| 5 | 1.012998295 |
| 10 | 1.02085804 |
| 20 | 1.018963904 |
| 40 | 0.990647056 |
| 80 | 0.961667394 |

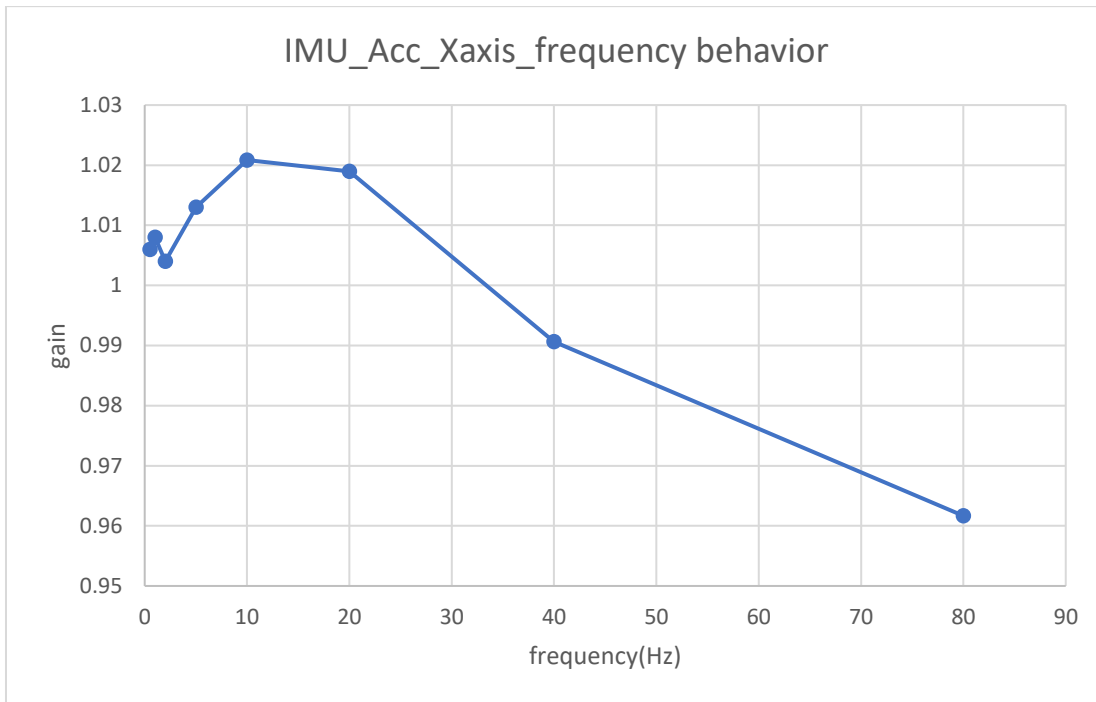


Figure 5.1.2-21 X-axis different frequency

On the Y-axis:

Table 5.1.2-13 ACC Y-axis different frequency

| Y-axis frequency behavior | |
|---------------------------|-------------|
| frequency(Hz) | gain |
| 0.5 | 1 |
| 1 | 1.005 |
| 2 | 1.004 |
| 5 | 1.0064469 |
| 20 | 1.019675067 |
| 40 | 0.99221546 |
| 80 | 0.952062426 |

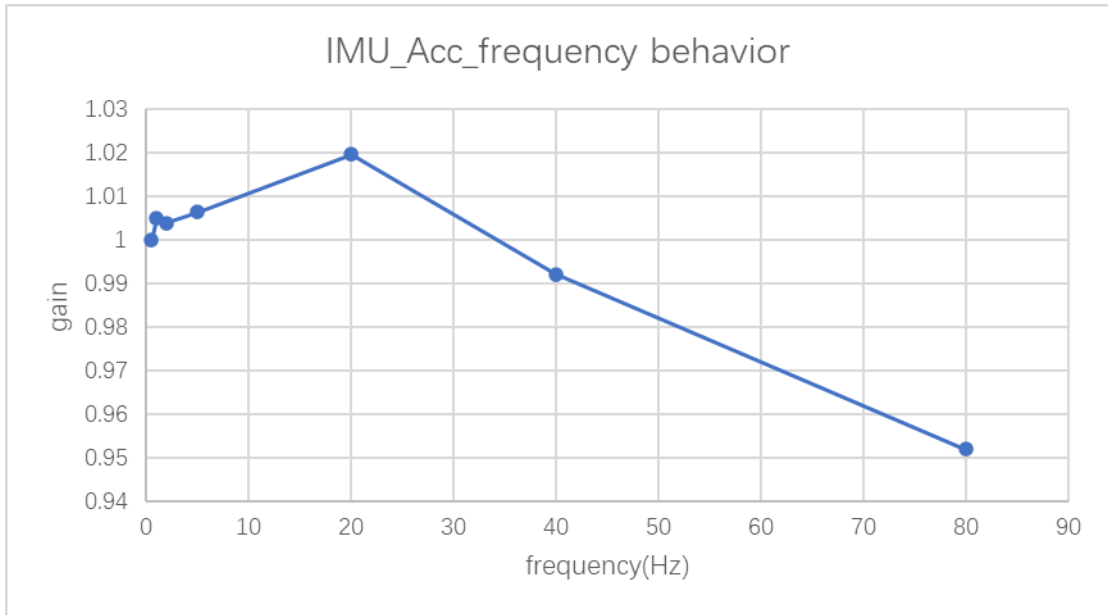


Figure 5.1.2-22 Acc Y-axis different frequency

On the Z-axis:

Table 5.1.2-14 Acc z-axis different frequency

| Z-axis frequency behavior | |
|---------------------------|-------------|
| FREQUENCY (Hz) | gain |
| 0.5 | 1.002 |
| 1 | 1.005 |
| 2 | 1.004 |
| 20 | 0.998098641 |
| 40 | 0.988292873 |
| 50 | 0.980304281 |
| 60 | 0.973995138 |
| 70 | 0.969079843 |
| 80 | 0.942100147 |

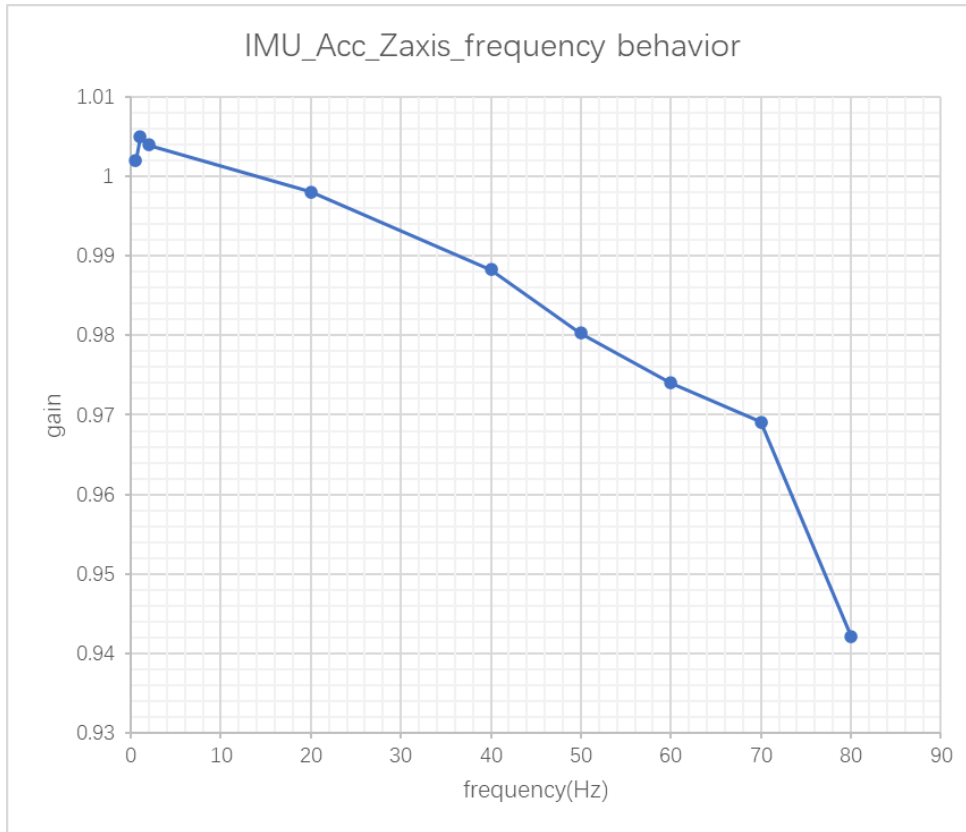


Figure 5.1.2-23 ACC z-axis different frequency

From the frequency response images of the above three-axis, when the frequency is greater than or equal to 40Hz, the gain will become less than 0.99.

Table 5.1.2-15 Acc z-axis large frequency

| IMU_Acc_Zaxis_large frequency behavior | | | |
|--|----------------|-----------------|-------------|
| FREQUENCY(Hz) | NOMINAL ACC(g) | Measured Acc(g) | gain |
| 0.5 | 0.1 | 0.1002 | 1.002 |
| 1 | 0.2 | 0.2005 | 1.005 |
| 2 | 0.1 | 0.1004 | 1.004 |
| 20 | 0.699 | 0.69767095 | 0.998098641 |
| 40 | 0.926 | 0.9151592 | 0.988292873 |
| 50 | 0.654 | 0.641119 | 0.980304281 |
| 60 | 0.617 | 0.600955 | 0.973995138 |
| 70 | 0.702 | 0.68029405 | 0.969079843 |
| 80 | 0.682 | 0.6425123 | 0.942100147 |

| | | | |
|-----|-------|------------|-------------|
| 90 | 0.66 | 0.6180401 | 0.936424394 |
| 100 | 0.641 | 0.59361175 | 0.926071373 |
| 120 | 0.616 | 0.55192565 | 0.895983198 |
| 160 | 0.585 | 0.48140715 | 0.822918205 |
| 200 | 0.613 | 0.4737978 | 0.772916476 |
| 240 | 0.609 | 0.40871905 | 0.671131445 |
| 315 | 0.741 | 0.3714771 | 0.501318623 |

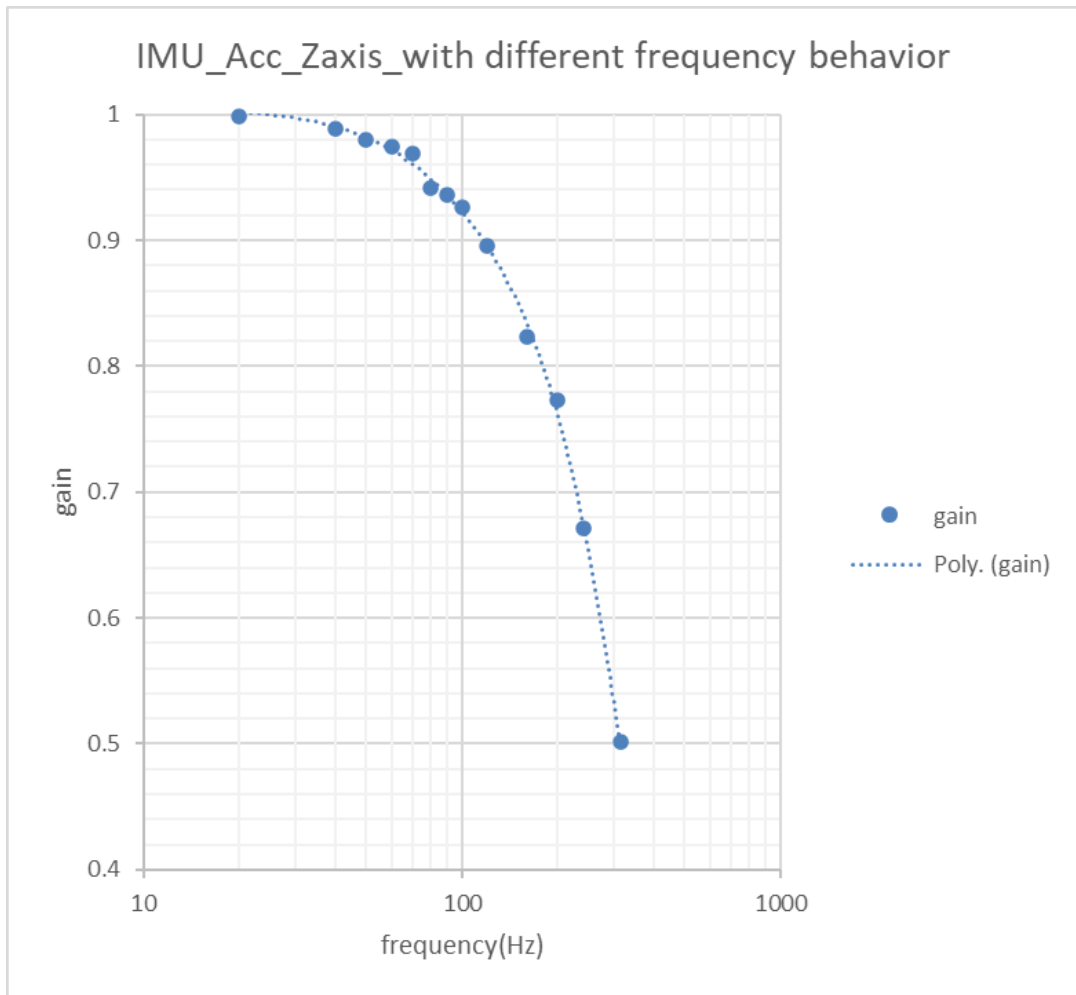


Figure 5.1.2-24 IMU_Acc_Zaxis frequency range behavior

From the large-scale high-frequency verification of the Z-axis, the frequency response curve conforms to the signal filtering performance of the low-pass filter in the datasheet.

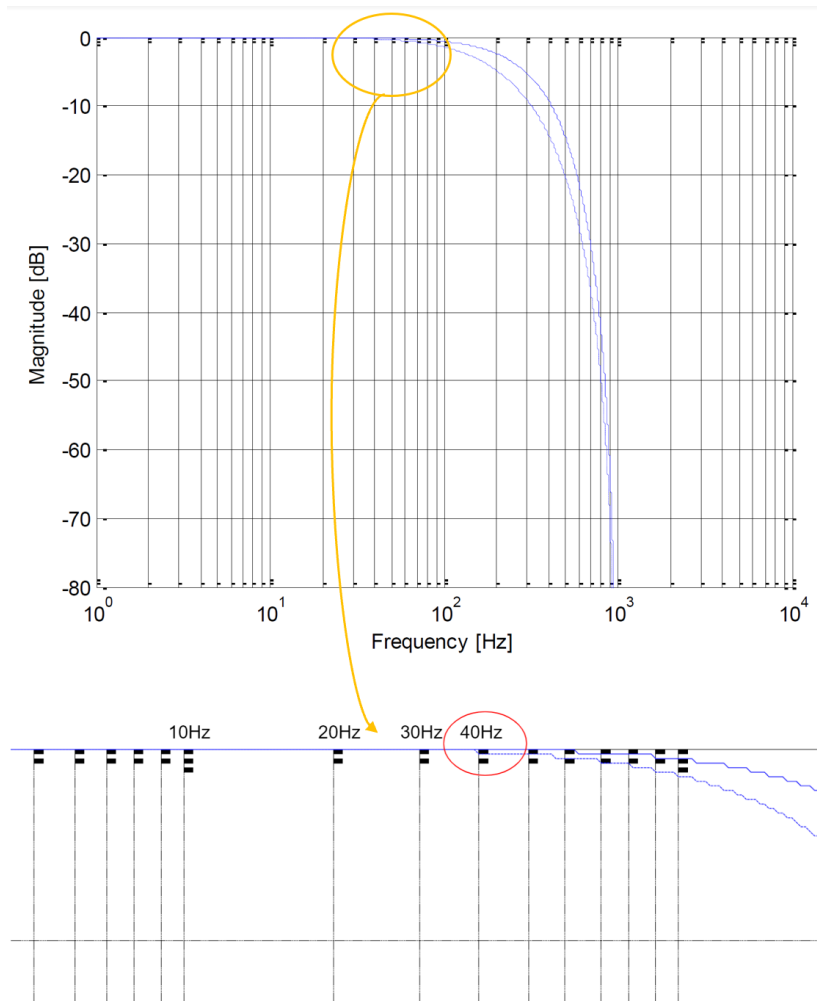


Figure 5.1.2-25 low pass filter at 262Hz frequency behavior

By partially zooming in the image, I can observe that when the frequency is greater than 40 Hz, the magnitude of the signal will begin to decrease. In the previous analysis, I found that when the frequency is greater than 40Hz, the ratio of measured acceleration to nominal acceleration is greater than 0.99 and less than 1. Now according to the characteristic curve of the datasheet, it was caused by the low-pass filter.

5.1.3 SAIFE Demonstrator

5.1.3.1 FOG data of demonstrator

In the beginning, the X-axis and Y-axis data of the prototype was measured, which was caused by the installation position of the fiber optic gyroscope. In the lateral test, the X-axis and Y-axis theoretically form an angle of 45° with the vertical.

Because the length of the connection cable between the power supply box and the prototype is very short, the cable is hard and difficult to produce elastic deformation. In the test, the torsion of the cable due to the rotating winding will affect the rotation of the round table. Therefore, I chose to fix the power supply box with the prototype for testing to eliminate adverse effects.

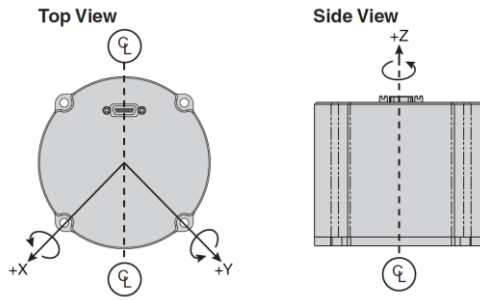


Figure 5.1.3-1 View of FOG

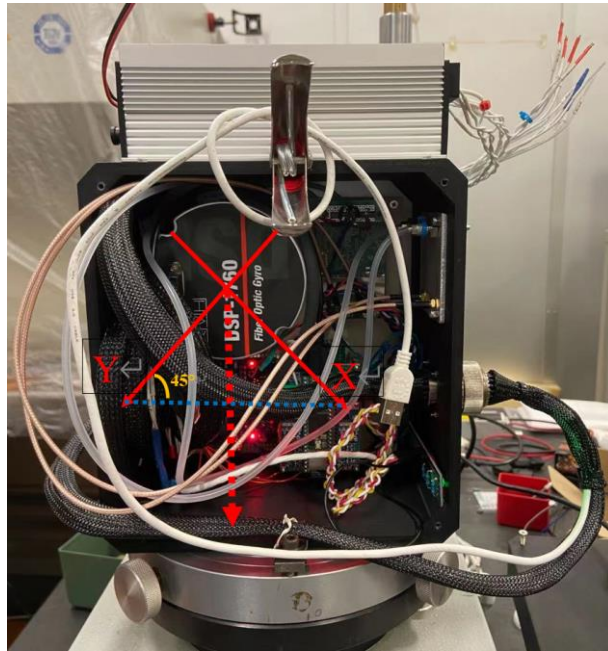


Figure 5.1.3-2 Axis component in demonstrator

Table 5.1.3-1 demonstrator gyro data on X-axis

| Demonstrator Gyro data on X-axis | | | | |
|----------------------------------|--------------------------------|-------------------------------|--------------------------|------------------------------------|
| Nominal speed($^{\circ}$ /s) | Measured speed($^{\circ}$ /s) | Ideal result ($^{\circ}$ /s) | RealAngle ($^{\circ}$) | Calibration output($^{\circ}$ /s) |
| 108.1934573 | 75.3897998 | 106.6172773 | 44.24 | 108.0601051 |
| 72.12901158 | 50.17160991 | 70.95337118 | | 71.91356728 |
| 36.06449307 | 25.11254374 | 35.51449994 | | 35.99510972 |
| 0 | -0.001942507 | -0.00274712 | | -0.002784296 |
| -36.06449307 | -25.09913385 | -35.49553549 | | -35.97588864 |
| -72.12901158 | -50.13008111 | -70.89464058 | | -71.8540419 |
| -108.1934573 | -75.38385836 | -106.6088749 | | -108.0515889 |

Table 5.1.3-2 Demonstrator gyro data on Y-axis

| Demonstrator Gyro data on Y-axis | | | | |
|----------------------------------|---------------------|--------------------|---------------|-------------------------|
| Nominal speed(°/s) | Measured speed(°/s) | Ideal result (°/s) | Real angle(°) | Calibration output(°/s) |
| 108.1934573 | 109.4023 | 109.4033581 | 45.76 | 107.9805906 |
| 72.12901158 | 72.9465 | 72.94719638 | | 71.99853354 |
| 36.06449307 | 36.4544 | 36.45477143 | | 35.98068485 |
| 0 | 0.00290261 | 0.002902638 | | 0.00286489 |
| -36.06449307 | -36.4507 | -36.4510953 | | -35.97705653 |
| -72.12901158 | -72.9379 | -72.93858304 | | -71.99003222 |
| -108.1934573 | -109.414 | -109.4146138 | | -107.9916999 |

In an ideal situation, the included angle between the X-axis and the Y-axis and the horizontal plane must be 45°. During the test, I placed it on the round table along the side of the box, as shown in the figure above. In theory, at this time I am testing the vertical components of the X and Y axes. Therefore, after obtaining the data, first, calculate the numerical trigonometric function according to 45°.

$$Ideal\ speed = \frac{measured\ speed}{\sin(45^\circ)}$$

Drawing according to the ideal value calculated under ideal conditions:

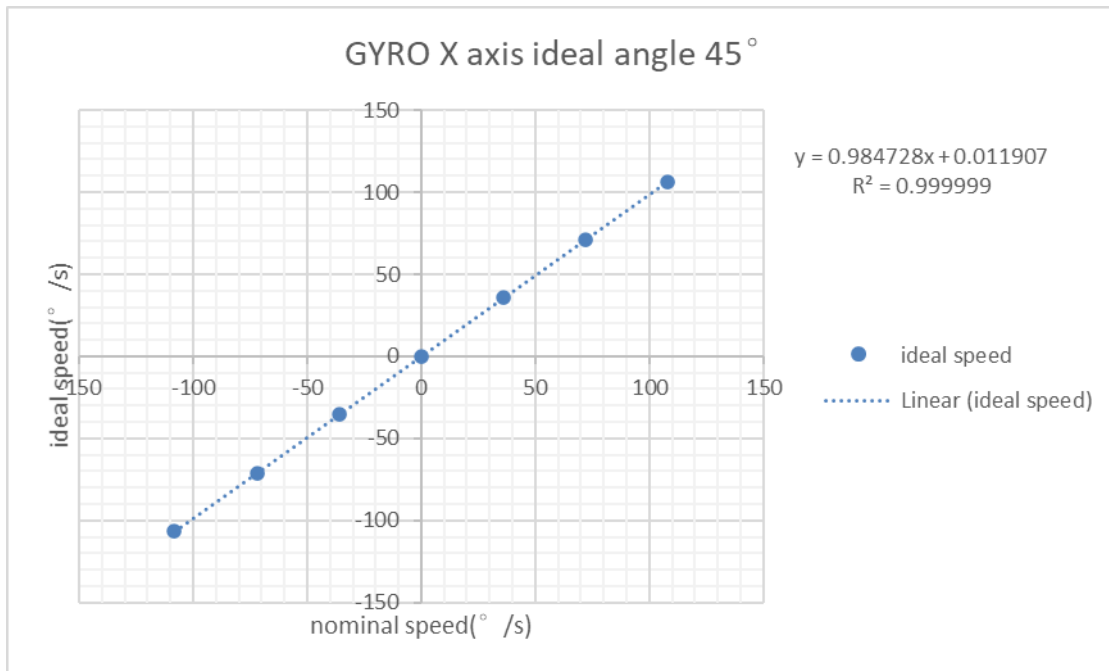


Figure 5.1.3-3 GYRO X-axis ideal angle

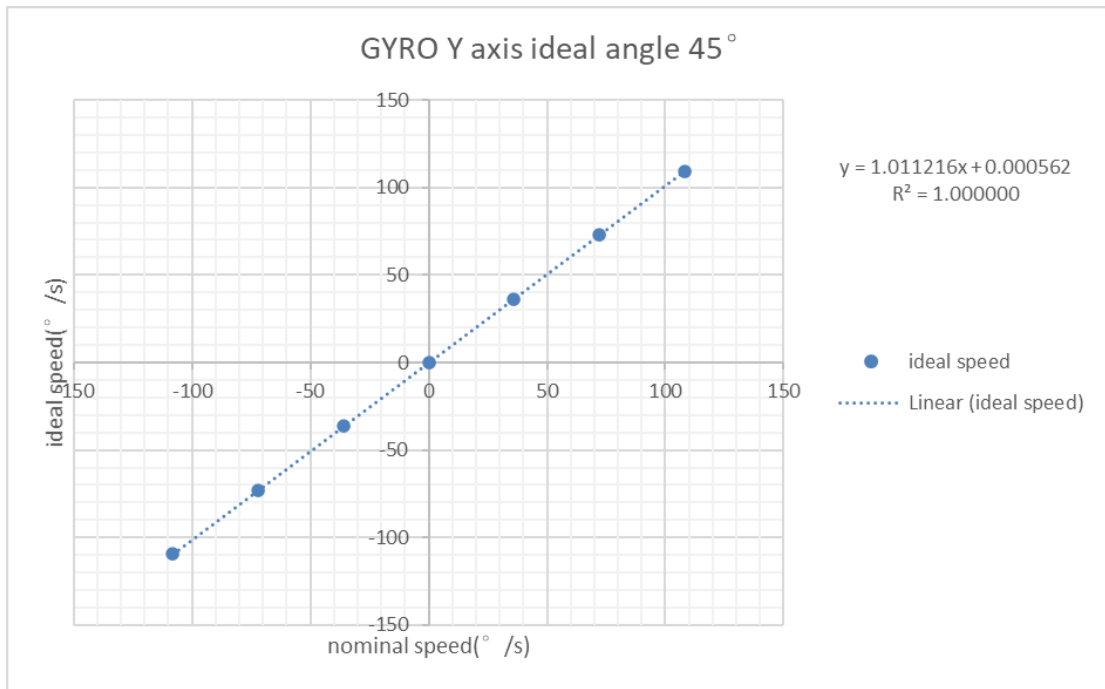


Figure 5.1.3-4 gyro Y-axis ideal angle 45°

At an ideal angle (45°), the linear regression equations of the X-axis and Y-axis of the fiber optic gyroscope are:

$$X \text{ axis: } \hat{y} = 0.984728x + 0.011907$$

$$Y \text{ axis: } \hat{y} = 1.011216x + 0.000562$$

It can be seen from the regression coefficient that on the X-axis, the regression coefficient is less than 1, and the measured value is lower than the nominal speed. On the Y-axis, the regression coefficient is greater than 1, and the measured value is higher than the nominal speed. From the previous results of separately verifying the fiber optic gyroscope, I can be sure that the angle between the X-axis and the Y-axis is absolutely 90°. So the current situation shows that the angle between the X-axis and the horizontal plane, and the angle between the Y-axis and the horizontal plane, must not be 45°. Therefore, I need to re-substitute an angle value to calculate the trigonometric function. This new angle value can be regarded as a real angle. The angle between the X-axis and the horizontal plane and the angle between the Y-axis and the horizontal plane are complementary angles to each other. After adjustment and calculation, when the real angle between the X-axis and the horizontal plane is 44.24°. The difference between the X-axis regression coefficient and the Y-axis regression coefficient is the smallest, indicating that the value of this real angle is true.

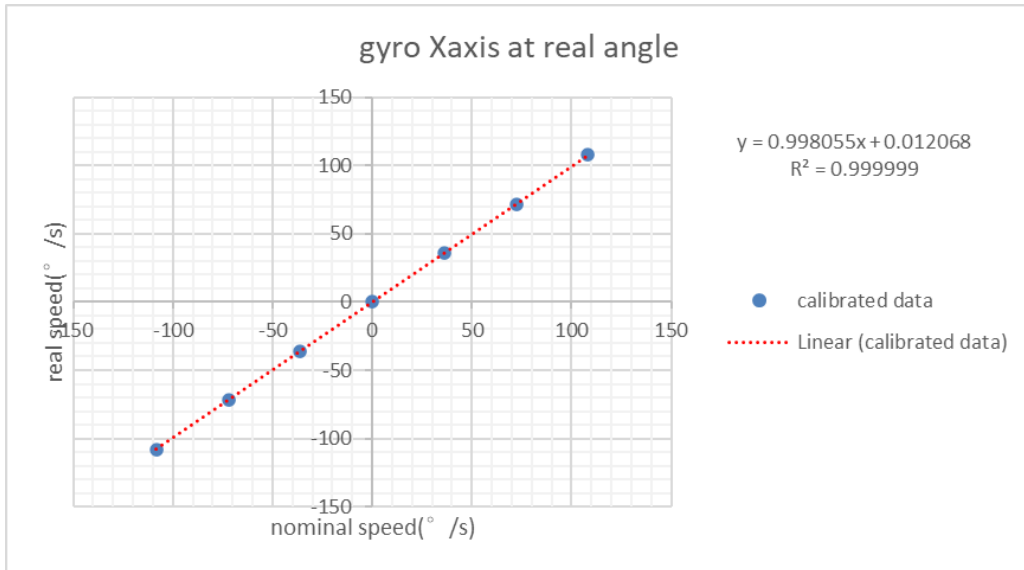


Figure 5.1.3-5 GYRO X-axis real angle

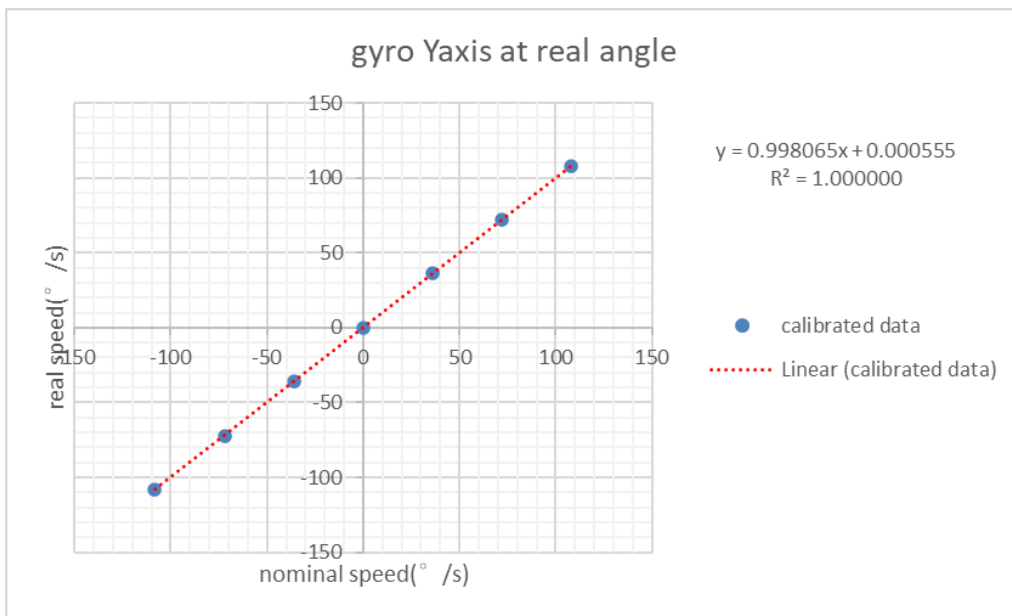


Figure 5.1.3-6 GYRO Y-axis at a real angle

At this time, the regression equations of the X-axis and Y-axis are:

$$X \text{ axis: } \hat{y} = 0.998055x + 0.012068$$

$$Y \text{ axis: } \hat{y} = 0.998065x + 0.000555$$

For the Z-axis of Gyro data:

Table 5.1.3-3 Demonstrator gyro z-axis

| demonstrator gyro data Z-axis | |
|-------------------------------|---------------------|
| nominal speed(°/s) | measured speed(°/s) |
| 108.1934573 | 108.2556958 |
| 72.12901158 | 72.1660387 |
| 36.06449307 | 36.08528317 |
| 0 | -0.002844802 |
| -36.06449307 | -36.08671844 |
| -72.12901158 | -72.1809468 |
| -108.1934573 | -108.2678073 |

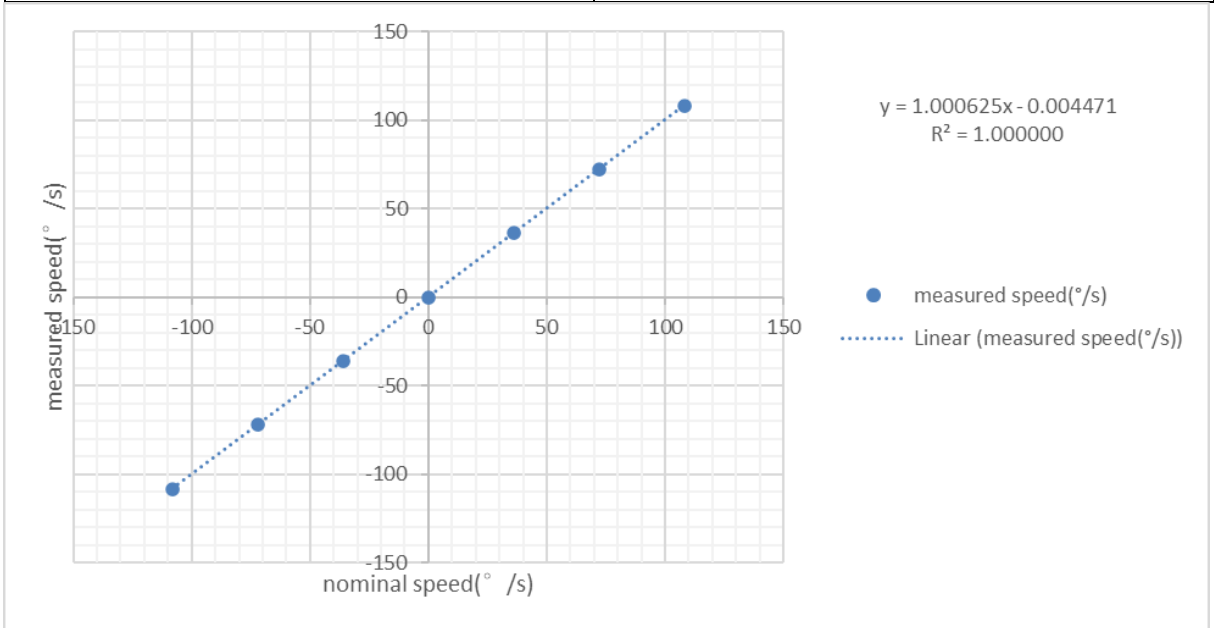


Figure 5.1.3-7 demonstrator Z-axis output

the regression equations of the Z-axis are:

$$Z \text{ axis: } \hat{y} = 1.000625x + 0.004471$$

5.1.3.2 For the inclinometer

Use a large tilt test bench for the inclinometer test, fix the BOX on the metal plate with four M2.5 screws, and use a gradient to calibrate the horizon. The inclinometer is divided into 2 directions to measure the tilt of the BOX, namely the X-axis and Y-axis. The scope of this test is a tilt test of $\pm 30^\circ$.

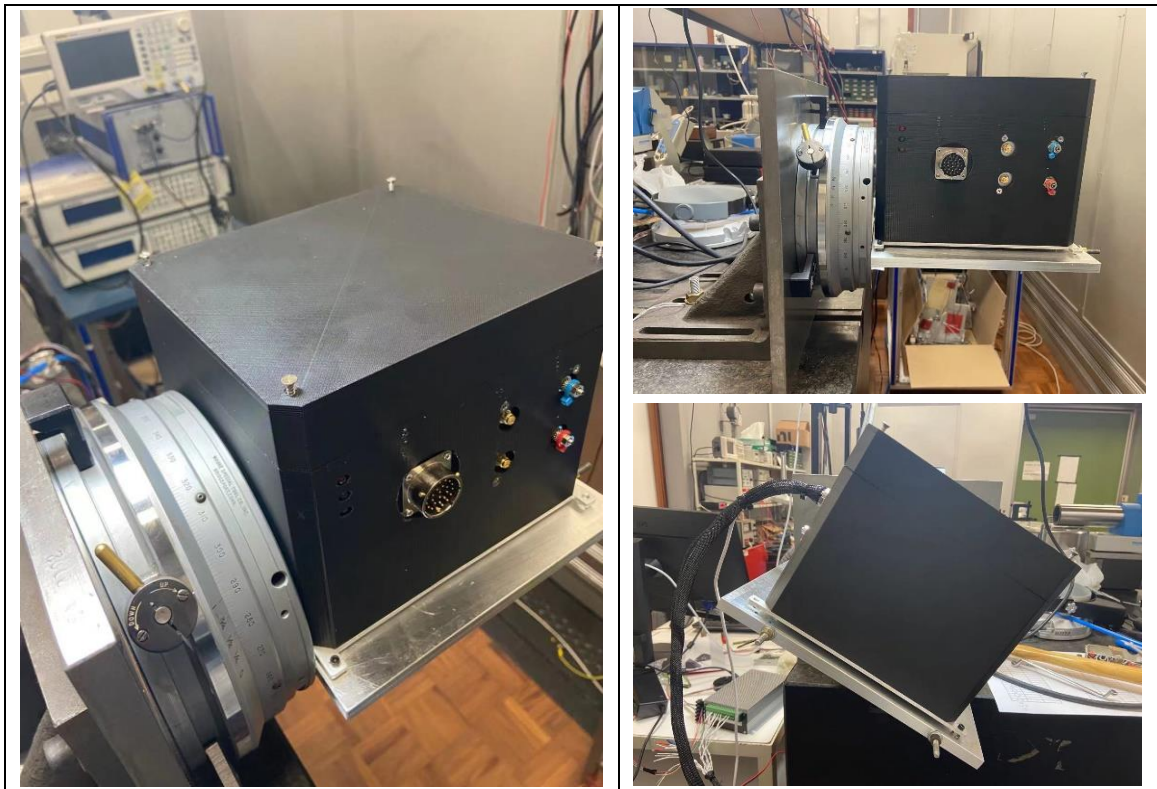


Figure 5.1.3-8 Inclinometer on platform

The platform starts from 0°, increases by 10° each time, and keeps this angle for a period of time to record data until it reaches the 30° position. Taking the X-axis from 0 to 30° as an example, the following are the test results:

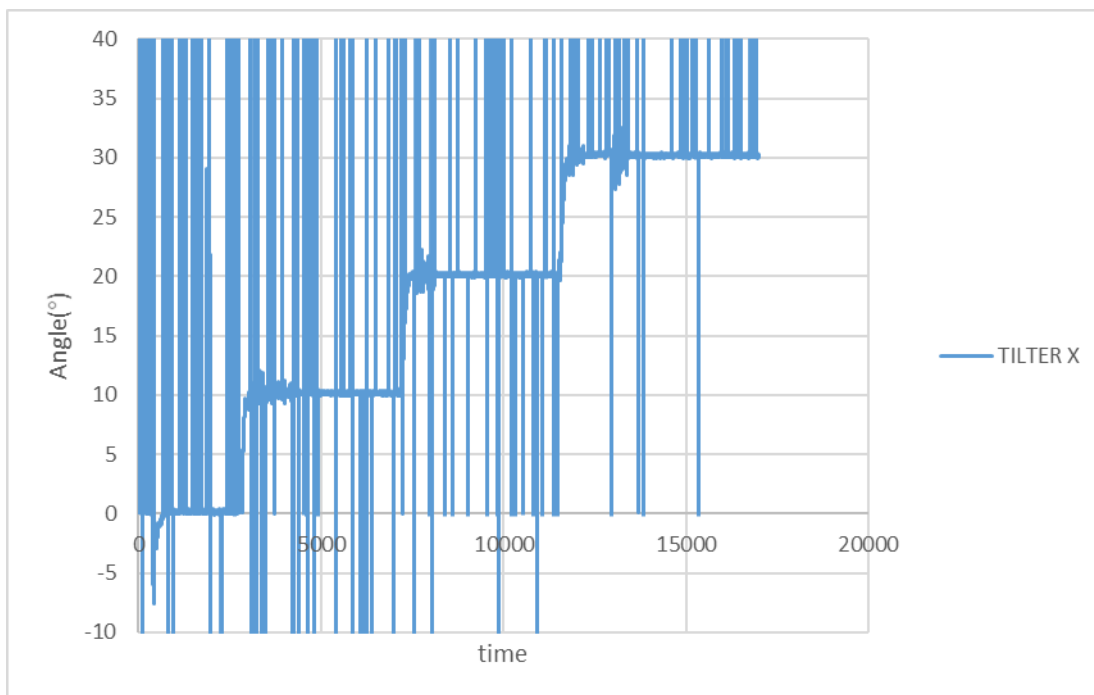


Figure 5.1.3-9 inclinometer X-axis recorded data

It can be roughly seen from the image that the inclinometer can record data, but there are a lot of abnormal values in the chart, which affects the data. This outlier is irregular, and these values are very large, the number is 999999. It is much higher than our maximum tilt angle of 30°. Therefore, a lot of vertical lines are displayed in the image.

Because these outliers are much larger than the measured value, I calculate the variance between adjacent values and judge whether it is an outlier that affects the result by the size of the variance. Some outliers are 999999, some outliers are not 999999 like the value is 90, but in our test, the maximum tilt angle is 30 degrees. A number with a value of 90 is impossible. For example: In the image, there are two adjacent values of a and b . If $a = 30, b = 30.2$. Variance: $(a - b)^2 = 0.04$. If $a = 30, b = 999999$. Then the variance: $(a - b)^2 = 999938000961$. This value is much greater than 1. If $a = 30, b = 90$. Variance: $(a - b)^2 = 360$. This value is also much greater than 1. I remove the numbers with variance greater than 1 and use the “IF” statement to edit in Excel.

$$IF((A1 - A2)^2 > 1; A2; 999999)$$

If the variance of the previous number minus the next number is less than 1, then keep the previous number. If the variance is greater than 1, then replace the value with 99999. Store the new data obtained in a new column, and then use the filtering function of Excel, or the function of deleting the duplicate number. Delete the value of 999999. The following is the image after cleaning the data.

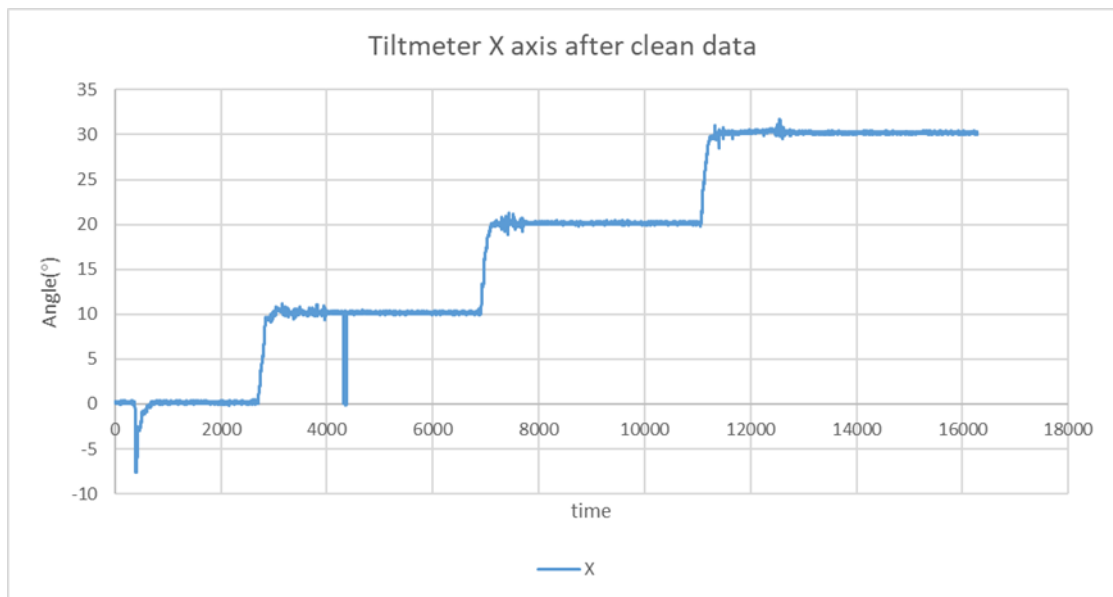


Figure 5.1.3-10 Inclinometer X-axis after clean data

Now you can use the AVERAGE function in Excel to find the back-end value of each segment. The following is the statistics of each tilt angle on the X axis of the inclinometer:

Table 5.1.3-4 Inclinometer data on X-axis

| Nominal angle (°) | measured angle(°) |
|---------------------|--------------------|
| 30 | 30.21333992 |
| 20 | 20.15217989 |
| 10 | 10.16886034 |
| 0 | 0.181814746 |
| -10 | -9.870688879 |
| -20 | -19.87720005 |
| -30 | -29.87227566 |

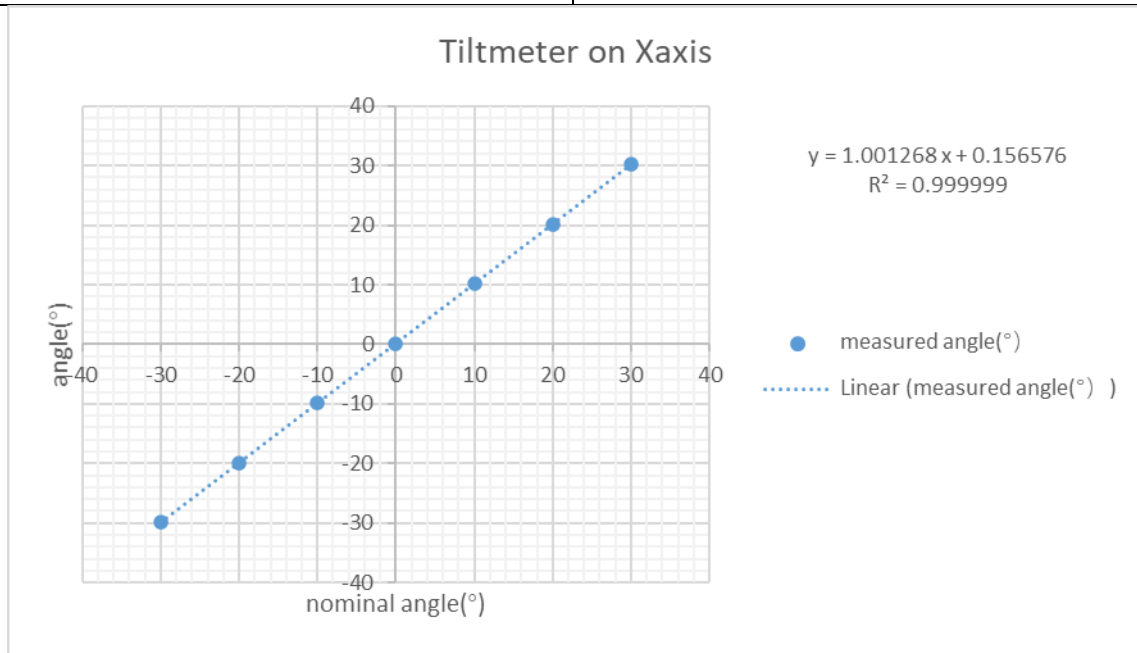


Figure 5.1.3-11 Inclinometer on X-axis

After linear regression analysis can be obtained, the linear regression equation of the inclinometer on the demonstrator is:

$$\hat{y} = 1.001268x + 0.156576$$

$R^2 = 0.999999$. It shows that the reliability of the regression equation is very high. The regression coefficient is 1.001268, that is, the test value is very close to the nominal value, which is almost a 0.1% fluctuation.

For the Y-axis of the Inclinometer:

I have selected a wider range of test angles, from -90° to $+90^\circ$. The method of data cleaning is the same as when processing the X-axis. Here is the table of the Inclinometer on the Y-axis:

| Tilt data on Yaxis | |
|--------------------|--------------|
| angle(°) | tilter Y(°) |
| 90 | 89.81147001 |
| 80 | 79.9364894 |
| 70 | 69.93133099 |
| 60 | 59.92472921 |
| 50 | 49.94245644 |
| 40 | 39.95374878 |
| 30 | 29.90769818 |
| 20 | 19.89645714 |
| 10 | 9.947869665 |
| 0 | -0.133939133 |
| -10 | -10.10529596 |
| -20 | -20.08231112 |
| -30 | -30.10744353 |
| -40 | -40.0571474 |
| -50 | -50.0854626 |
| -60 | -60.05794184 |
| -70 | -70.09135136 |
| -80 | -80.04401278 |
| -90 | -89.82449919 |

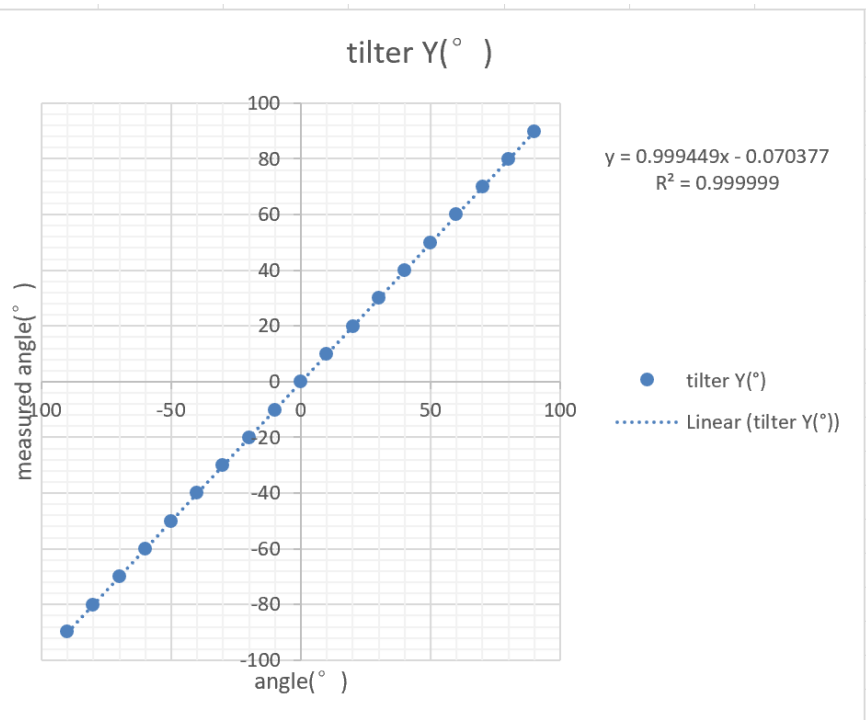


Figure 5.1.3-12 angle data on Y-axis

the linear regression equation of the inclinometer Y-axis on the demonstrator is:

$$\hat{y} = 0.999449x - 0.070377$$

5.1.3.3 For the Accelerometer of the demonstrator

In the demonstrator, theoretically, when the demonstrator is placed completely horizontal to the ground, only the direction perpendicular to the ground has the acceleration of gravity g . When I rotate along the X-axis, the acceleration of gravity will be generated in the Y-axis direction. The value of the component changes according to the rotation angle. Theoretically, the output waveform should be a sinusoid curve.

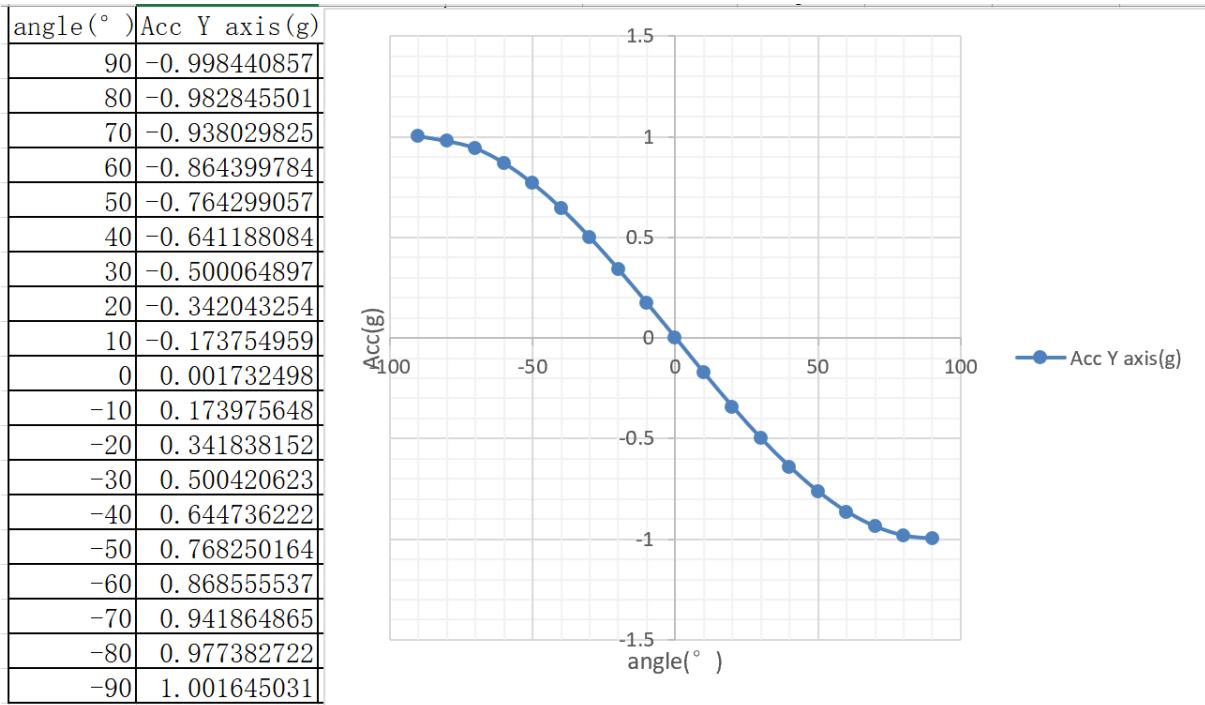


Figure 5.1.3-13 Acc data on Y-axis

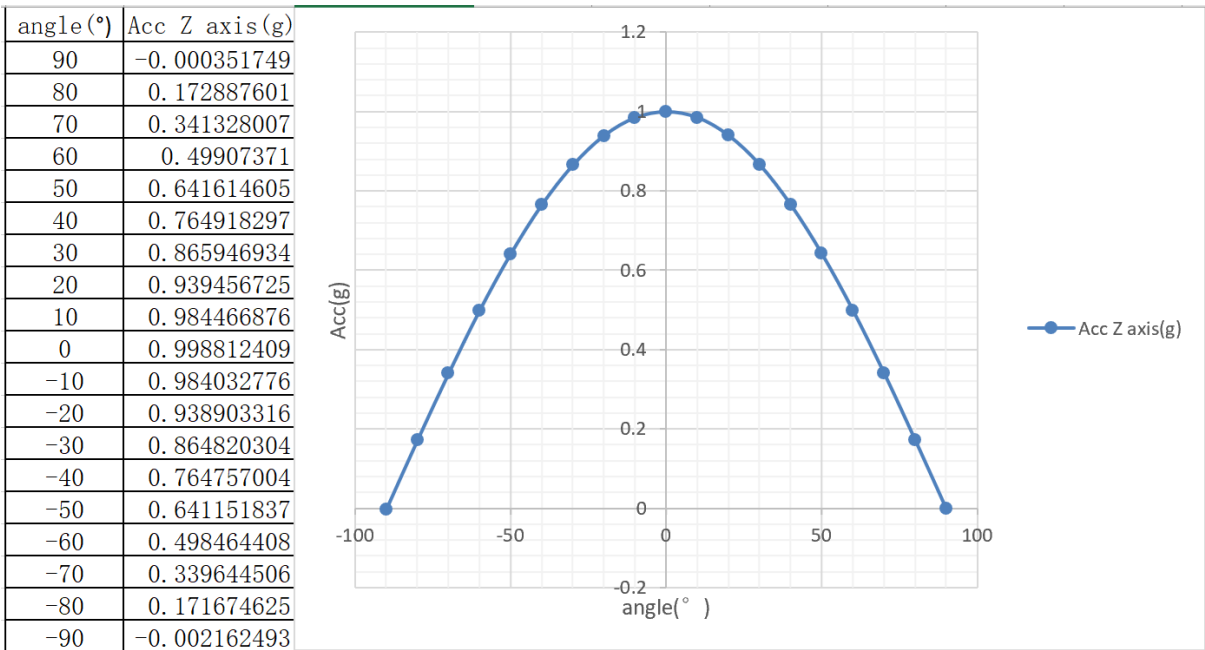


Figure 5.1.3-14 Acc data on Z-axis

From the image analysis, it can be found that when the demonstrator rotates from -90° to $+90^\circ$, the data changes conform to the trigonometric function. All the units for the acceleration of gravity in this article are g. When the demonstrator is in a horizontal state, the acceleration of gravity on the Z-axis reaches the maximum value of 1, and there is no gravity acceleration component on the Y-axis at this time, and the value is very close to 0. When the demonstrator rotates to -90° or $+90^\circ$, the gravitational acceleration is almost all on the Y-axis, and the value on the Z-axis is almost 0.

In addition, I found that in the original file of the data, the Z-axis data output format of the Inclinometer is not an angle but is displayed in the form of gravitational acceleration. I graph and analyze the data on an inclinometer. Get the following image:

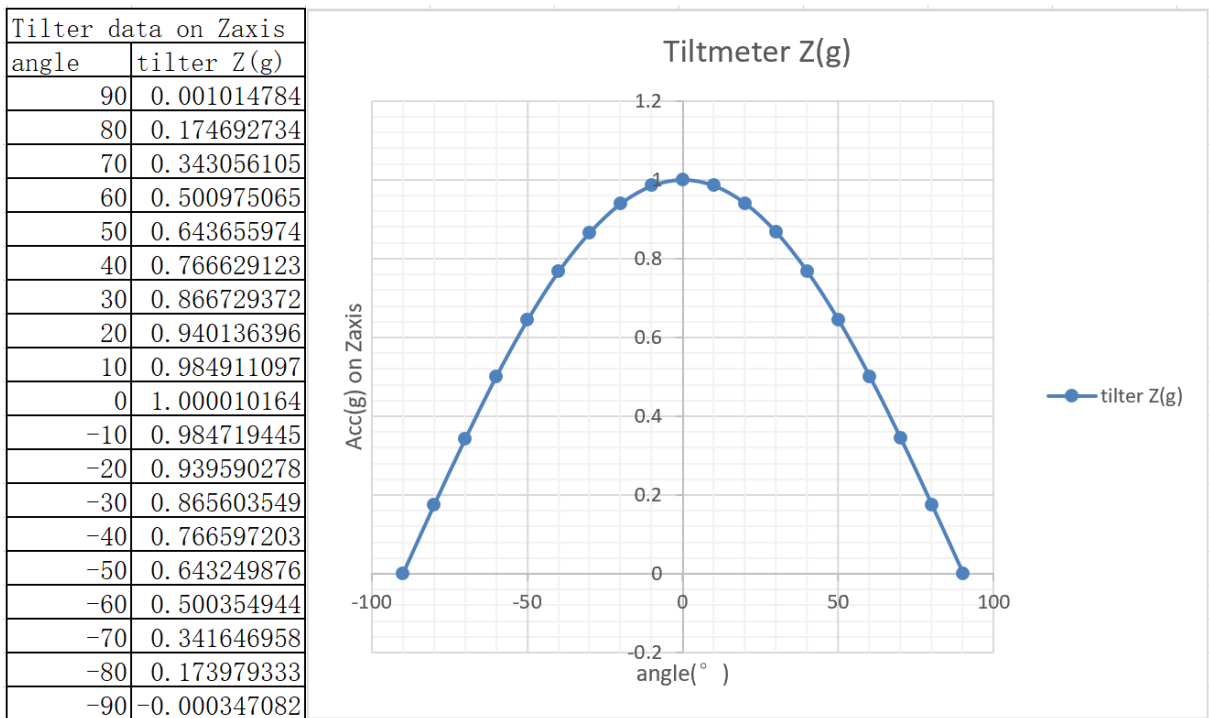


Figure 5.1.3-15 gravity Acc showed on the Tilt Z-axis

In conclusion, I integrate the gravitational acceleration value of the Z-axis on the Inclinometer and the gravitational acceleration value of the Z-axis on the Accelerometer into one chart.

Table 5.1.3-5 Integrated gravity acceleration

| Angle(°) | Acc Z axis(g) | Tilt Z axis(g) | Theoretical value(g) |
|----------|---------------|----------------|----------------------|
| 90 | -0.000351749 | 0.001014784 | 6.12574E-17 |
| 80 | 0.172887601 | 0.174692734 | 0.173648178 |
| 70 | 0.341328007 | 0.343056105 | 0.342020143 |
| 60 | 0.49907371 | 0.500975065 | 0.5 |
| 50 | 0.641614605 | 0.643655974 | 0.64278761 |
| 40 | 0.764918297 | 0.766629123 | 0.766044443 |
| 30 | 0.865946934 | 0.866729372 | 0.866025404 |
| 20 | 0.939456725 | 0.940136396 | 0.939692621 |
| 10 | 0.984466876 | 0.984911097 | 0.984807753 |
| 0 | 0.998812409 | 1.000010164 | 1 |
| -10 | 0.984032776 | 0.984719445 | 0.984807753 |
| -20 | 0.938903316 | 0.939590278 | 0.939692621 |
| -30 | 0.864820304 | 0.865603549 | 0.866025404 |
| -40 | 0.764757004 | 0.766597203 | 0.766044443 |
| -50 | 0.641151837 | 0.643249876 | 0.64278761 |
| -60 | 0.498464408 | 0.500354944 | 0.5 |
| -70 | 0.339644506 | 0.341646958 | 0.342020143 |
| -80 | 0.171674625 | 0.173979333 | 0.173648178 |
| -90 | -0.002162493 | -0.000347082 | 6.12574E-17 |

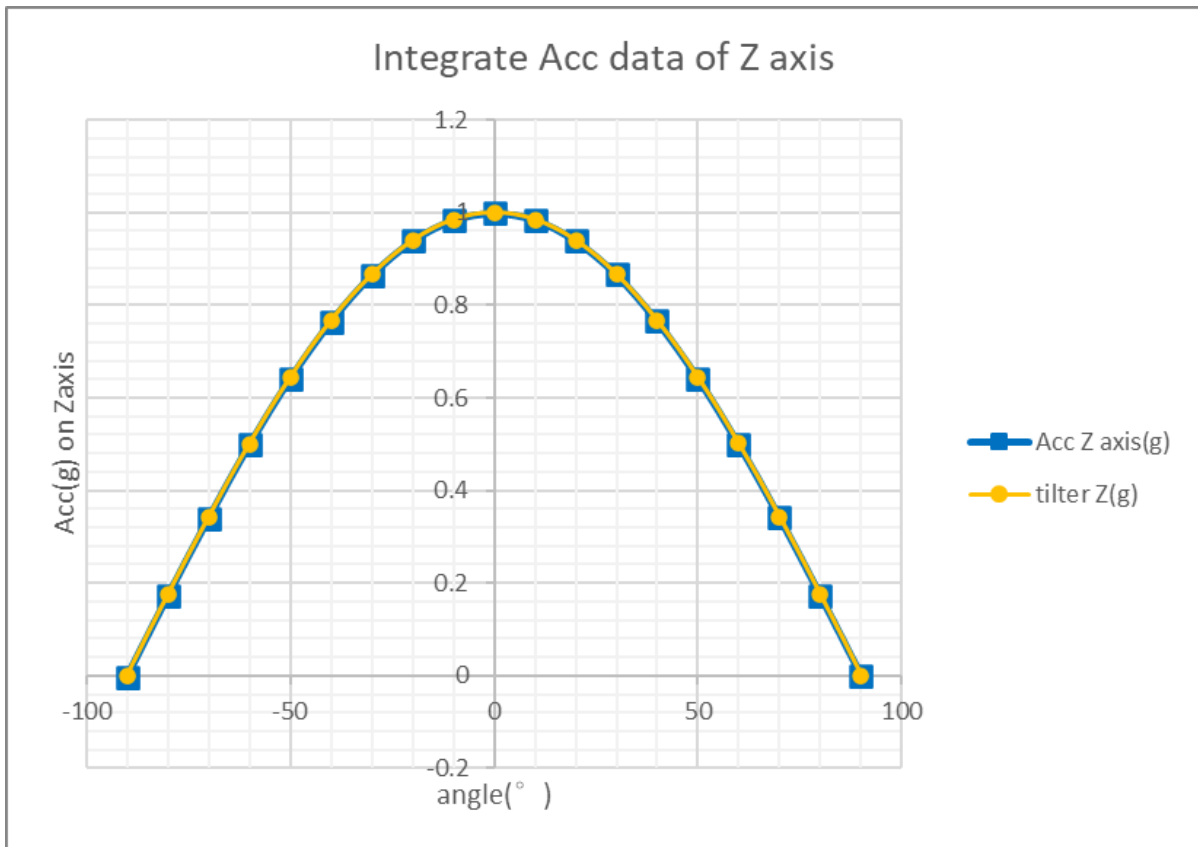


Figure 5.1.3-16 Integrate gravity acc data

From the image, it can be observed that the fitting effect of the two is very good.

6 Conclusions

Based on the performance and performance of the fiber optic gyroscope, it can be considered as an excellent fiber optic gyroscope with very high accuracy. The gap between the test data and the actual data is only three ten-thousandth. The low-pass filter inside the fiber optic gyroscope performs very well. When the data sampling time is 1 millisecond, the Gyro Filter Cut-off Frequency is 5000 Hz. Affected by the installation error of the fiber optic gyroscope and the manufacturing error of the demonstrator parts, the performance error of the X-axis and Y-axis of the fiber optic gyroscope in the demonstrator is 0.2%. The performance error range of the Z-axis of the fiber optic gyroscope in the demonstrator is 0.06%.

The angular velocity of the earth's rotation has a certain influence on the optical fiber sensor. According to the calculation of this test, the earth's rotation angular velocity is $0.00425^\circ/s$. The angular speed of Earth's rotation in inertial space is $(7.2921150 \pm 0.0000001) \times 10^{-5}$ radians per second. Multiplying by $(180^\circ/\pi \text{ radians})$, the result is $0.004178^\circ/s$. Error is 1.7%.

From the performance of the demonstrator's IMU, the gyroscope performance of IMU is not as good as fiber optic gyroscope. The scale factor of the gyroscope in the IMU ranges from 0.03% to 0.2% based on the scale factor calculated from the data. The gyroscope performance of this

IMU is similar to that of the fiber optic gyro, but the fiber optic gyro is more stable in all 3 axes. For the accelerometer static testing of the demonstrator, from -90° to $+90^{\circ}$ tilt, the IMU's linear accelerometer performed very well, with an error of 0.2% between the measured value and the nominal value. Because the maximum operating frequency of the low-pass filter is 262Hz. Based on the observation, when the acceleration input frequency is less than 40Hz, the error between the measured value and the input value of the accelerometer is 0.05%. When the frequency is greater than 40Hz, the error between the measured value and the input value is greater than 1%, and with the increase of frequency, the error value will gradually increase linearly. Presumably, due to the use of different test platforms for low-frequency and high-frequency motion, this will be the next step in the validation effort in the future.

In summary, the results of the individual sensor tests are compared to the results of the sensors integrated into the demonstrator. Based on the observation, the output of the demonstrator has some deviation from the theoretical expectation, although this deviation is larger than the deviation produced by the independent sensor test, it will not affect the performance of the demonstrator. According to the results of extensive experience, this demonstrator has been proved to be robust and reliable in the test environment.

Reference

- [1] [Online]. Available: <https://en.wikipedia.org/wiki/Avionics>.
- [2] S. P. D. a. S. J. Sanders, "Fiber Optic Gyros - A Compelling Choice for High Precision Applications," *OSA Technical Digest*, 2006.
- [3] F. S. a. A. N. Francois du Plessis, "An Alternative Methodology for Fiber Optic Gyroscope Calibration," in *AIAA Guidance, Navigation, and Control Conference*, Chicago, 2012.
- [4] V. Y. S. G. B. D. V. G. P. D. V. V. & A. A. U. I. K. Meshkovsky, "Three-axis fiber-optic gyroscope: Development and test results," *Gyroscope and Navigation*, 2011.
- [5] S.-h. P. Won and F. Golnaraghi, "A Triaxial Accelerometer Calibration Method Using a Mathematical Model," *IEEE TRANSACTIONS ON INSTRUMENTATION AND MEASUREMENT*, 2010.
- [6] P. Batista, C. Silvestre, P. Oliveira and B. Cardeira, "Accelerometer Calibration and Dynamic Bias and Gravity Estimation: Analysis, Design, and Experimental Evaluation," *IEEE TRANSACTIONS ON CONTROL SYSTEMS TECHNOLOGY*, 2011.
- [7] Bidspotter, [Online]. Available: <https://www.bidspotter.com/en-us/auction-catalogues/bscliq/catalogue-id-bscliq10008/lot-e601a749-1dfe-486f-8c63-a3e10164935f>.
- [8] A. company. [Online]. Available: <https://www.arduino.cc/en/Guide/ArduinoUno#install-the-board-drivers>.
- [9] "CLV-2534 Compact Laser Vibrometer," [Online]. Available: https://www.atecorp.com/atecorp/media/pdfs/data-sheets/polytec-clv-2534_datasheet.pdf?ext=.pdf.
- [10] modalshop, "Vibration-Shaker," [Online]. Available: [https://www.modalshop.com/filelibrary/75lbf-Vibration-Shaker-Datasheet-\(DS-0077\).pdf](https://www.modalshop.com/filelibrary/75lbf-Vibration-Shaker-Datasheet-(DS-0077).pdf).
- [11] H. C. Lefevre, *The Fiber-Optic Gyroscope*, Artech House Publishers, 2014.
- [12] KVH, "Fiber optic gyroscope," [Online]. Available: <https://www.kvh.com/admin/products/gyros-imus-inss/fiber-optic-gyros/dsp-1760/commercial-dsp-1760>.
- [13] Y. J. Morton, F. v. Diggelen, J. James J. Spilker and B. W. Parkinson, *MEMS Inertial Sensors*, Wiley-IEEE Press, 2021.
- [14] Sensoror, "STIM318," [Online]. Available: <https://www.sensoror.com/products/inertial-measurement-units/stim318/>.

- [15] "Linear regression," [Online]. Available: https://en.wikipedia.org/wiki/Linear_regression.
- [16] Sensoror. [Online]. Available: <https://www.sensoror.com/products/inertial-measurement-units/stim318/>.